THE GRADUATE UNIVERSITY FOR ADVANCED STUDIES

DOCTORAL THESIS

Studies on molecular magnetic properties using *ab initio* quantum chemical methods

Tran Nguyen Lan

DEPARTMENT OF FUNCTIONAL MOLECULAR SCIENCE

SCHOOL OF PHYSICAL SCIENCES

June 2014

Acknowledgements

I am deeply indebted to many people, for whom without their support, this thesis could not have been achieved.

First and foremost, I would like to thank my supervisor Prof. Takeshi Yanai, who gave me the opportunity to study quantum chemistry at Institute for Molecular Science (IMS). I always appreciate that he kindly helped me to get the Japanese Government (MEXT) Scholarship for studying in Japan. I am most grateful to him for his patience, encouragement, and invaluable discussion throughout my PhD study. I am greatly indebted for his kindest help when I was starting my life in Japan. Moreover, I am very grateful to him for the discussion and recommendation about my future.

I would like to thank Prof. Yuki Kurashige for his fruitful discussions. I have been using his density matrix renormalization group (DMRG) code for most of my studies.

I would like to express my gratitude to Dr. Jakub Chalupský for his everyday help and collaboration. Throughout the discussions with him, I have been learning a lot of knowledge about quantum chemistry. Also, I would like to thank him for carefully reading my thesis. I know that it required a lot of time and patience. By the way, I would like to thank his family for the hospitality and very good lunches.

I would like to thank the Japanese Government for financial support through the MEXT Scholarship.

I would like to thank Prof. Hiroki Nakamura, who introduced me to Prof. Yanai's research group. I would like to express my own appreciation to Prof. Vo Ky Lan and Prof. Tran Hoang Hai for their recommendation and constant support.

I would like to thank the other friends, colleagues, and guests of Prof. Yanai's research group not only for scientific discussion, but also for enjoyable time.

Finally, I would like to thank my family and my fiancée for their greatest love, patience, and encouragement.

List of Publications

Publications related to the thesis

1. <u>T. N. Lan</u>, T. Yanai,
   "*Correlated one-body potential from second-order Møller-Plesset perturbation theory: Alternative to orbital-optimized MP2 method*",
   J. Chem. Phys. **138**, 22418 (2013).

2. <u>T. N. Lan</u>, Y. Kurashige, T. Yanai,
   "*Toward reliable prediction of hyperfine coupling constants using ab initio density matrix renormalization group method: diatomic $^2\Sigma$ and vinyl radicals as test cases*",
   J. Chem. Theory Comput. **10**, 1953 (2014).

3. <u>T. N. Lan</u>, Y. Kurashige, T. Yanai,
   "*Scalar reltativistic calculations of hyperfine coupling constants using ab initio density matrix renormalization group in combination with third-order Douglas-Kroll-Hess transformation: case studies of 4d transition metals*",
   In preparation.

4. <u>T. N. Lan</u>, J. Chalupský, T. Yanai,
   "*Molecular g-tensors from analytical response theory and quasi-degenerate perturbation theory in framework of complete active space self-consistent field method*",
   In preparation.

5. Y. Kurashige, J. Chalupský, <u>T. N. Lan</u>, T. Yanai,
   "*Complete active space second-order perturbation theory with cumulant approximation for large entanglement space from density matrix renormalization group*"
   In preparation.

Other Publications

6. <u>T. N. Lan</u>,
   "*Resonant tunneling in closo-carborane dimers: first principle calculations,*"
   In preparation.

7. <u>T. N. Lan</u>, L. B. Ho, and T. H. Hai,
   "*Electronic and magnetic properties of hybrid boron-nitride/graphene nanoribbons having topological line defects at heterojunctions,*"
   In preparation.

8. <u>T. N. Lan</u>,
   "*Electronic transport properties of molecular junctions based on the direct binding of aromatic ring to electrodes,*"
   Chem. Phys. **428**, 53 (2014).

9. L. B. Ho, <u>T. N. Lan</u>, and T. H. Hai,
   "*Monte Carlo simulations of core/shell nanoparticles containing interfacial defects: Role of disordered ferromagnetic spins,*"
   Physica B **430**, 10 (2013).

10. <u>T. N. Lan</u> and T. H. Hai,
    "*Role of the poly-dispersity and the dipolar interaction in magnetic nanoparticle systems: Monte Carlo study,*"
    J. Non-Cryst. Solids **357**, 996 (2011).

11. T. H. Hai, L. H. Phuc, L. K. Vinh, B. D. Long, T. T. Kieu, N. N. Bich, <u>T. N. Lan</u>, N. Q. Hien, L. H. A. Khoa, and N. N. V. Tam,
    "*Immobilizing of anti-HPV18 and E. coli O157: H7 antibodies on magnetic silica-coated Fe_3O_4 for early diagnosis of cervical cancer and diarrhea,*"
    Inter. J. Nanotech. **8**, 383 (2011).

12. <u>T. N. Lan</u> and T. H. Hai,
    "*Monte Carlo simulation of magnetic nanoparticle systems,*"
    Comput. Mater. Sci. **49**, S287 (2010).

Contents

List of Abbreviations

1c	One-Component
2c	Two-Components
4c	Four-Components
4c-CI	Four-Component Configuration Interaction
4c-DFT	Four-Component Density Functional Theory
4c-DMRG	Four-Component Density Matrix Renormalization Group
ani	Anisotropic
AO	Atomic Orbital
B2PLYP	Double Hybrid Functional
B3LYP	Becke, Lee, Yang, and Parr Hybrid Functional
BO	Born-Oppenheimer
BCC	Brueckner Coupled Cluster
BP86	Becke and Perdew Functional
BP	Breit-Pauli
CABS	Complementary Auxilliary Basis Set
CAS	Complete Active Space
CASCI	Complete Active Space Configuration Interaction
CASPT2	Complete Active Space Second-Order Perturbation
CASSCF	Complete Active Space Self-Consistent Field
CC	Coupled Cluster
CCSD	Coupled Cluster Singles and Doubles
CCSD(T)	Coupled Cluster Singles and Doubles with Perturbative Triples
CI	Configuration Interaction
CIS	Configuration Interaction Singles
CIS(D)	Configuration Interaction Singles with Perturbative Triples
CISD	Configuration Interaction Singles and Doubles
CISDT	Configuration Interaction Singles, Doubles, and Triples
CP	Coupled-Perturbed

CP-CASSCF	Coupled-Perturbed Complete Active Space Self-Consistent Field
CP-CAS	CP-CASSCF with Perturbation-Induced Obital Relaxtion
CP-CI	CP-CASSCF withhout Perturbation-Induced Obital Relaxtion
CP-DMRG	Coupled-Perturbed Density Matrix Renormalization Group
CP-KS	Coupled-Perturbed Kohn-Sham
CT	Canonical Transformation
DFT	Density Functional Theory
DHF	Dirac-Hartree-Fock
DKH(n)	(n-Order) Douglas-Kroll-Hess
DMRG	Density Matrix Renormalization Group
EA	Electron Affinity
EPR	Electron Paramagnetic Resonance
ENC	Effective Charge Nucleus
FC	Fermi Contact
FCI	Full Configuration Interaction
FN	Finite Nuclear
FNSSO	Flexible Nuclear Screening Spin-Orbit
fpFW	Free-Particle Foldy-Wouthuysen
GC	Gauge Correction
GIAO	Gauge-Including Atomic Orbital
GGA	Generalized Gradient Approximation
HF	Hartree-Fock
hfc	Hyperfine Coupling
HFCC	Hyperfine Coupling Constant
HOMO	Highest Occupied Molecular Orbital
IORA	Infinite-Order Regular Approximation
IP	Ionization Potential
iso	Isotropic
LC	Long-Range Correction
LC-wPBE	LC of Perdew, Burke and Ernzerhof Functional Functional
LDA	Local Density Approximation
LFT	Ligand Field Theory
LRT	Linear Response Theory
LR-DFT	Linear Response Density Functional Theory
LR-CASSCF	Linear Response Complete Active Space Self-Consistent Field

LUMO	Lowest Unoccupied Molecular Orbital
MAX	Maximum Absolute Deviation
MAD	Mean Absolute Deviation
MCDF	Multi-Configuration Dirac-Fock
MCSCF	Multiconfigurational Self-Consistent Field
MF	Mean-Field
MO	Molecular Orbital
MPn	n-Order Møller-Plesset Perturbation
MRCI	Multireference Configuration Interaction
MRCI-SD	Multireference Configuration Interaction Singles and Doubles
MRSOCI	Multireference Spin-Orbit Configuration Interction
NESC	Normalized Elimination of Small Component
NR	Non-Relativistic
OB-MP2	One-Body Second-Order Møller-Plesset Perturbation
OCC	Orbital-Optimized Coupled Cluster
OEP	Optimized Effective Potential
OO-MP2	Orbital-Optimized Second-Order Møller-Plesset Perturbation
OO-RI-MP2	Resolution-of-Identity Approximation OO-MP2
OZ	Orbital-Zeeman
PBE	Perdew, Burke and Ernzerhof Functional
PCE	Picture Change Error
QCI	Quadratic Configuration Interaction
QCISD	Quadratic Configuration Interaction Singles and Doubles
QCISD(T)	QCI Singles and Doubles with Perturbative Triples
QDPT	Quasi-Degenerate Perturbation Theory
qrel	quasi-relativistic
RASSCF	Restricted Active Space Self-Consistent Field
RASSI	Restricted Active Space State Interaction
RDFT-LR	Restricted Open-Shell DFT Linear Response
RMS	Root Mean Square
RI	Resolution-of-Identity
ROHF	Restricted Open-Shell Hartree-Fock
SAC-CI	Symmetry Adapted Configuration Interaction
SCF	Self-Consistent Field
SD	Spin-Dipole

SNO	Spin Natural Orbital
SO	Spin-Orbit
SO-CASSCF	Spin-Orbit Complete Active Space Self-Consistent Field
SO-RASSI	Spin-Orbit Restricted Active Space State Interaction
SOC	Spin-Orbit Coupling
SOMO	Singly Occupied Molecular Orbital
SON	Spin Occupation Number
SOS	Sum-Over-States
SOS-CASPT2	CASPT2 based Sum-Over-States
SOS-DFPT	Sum-Over-State Density Functional Perturbation Theory
SOS-MRCI	MRCI based Sum-Over-States
SOSNO	Singly Occupied Spin Natural Orbital
SNSO	Screening Nuclear Spin-Orbit
SR	Scalar Relativistic
SZ	Spin-Zeeman
TPSS	Tao, Perdew, Staroverov, and Scuseria Functional
TPSSh	Hybrid Version TPSS Functional
UHF	Unrestricted Hartree-Fock
ZORA	Zeroth-Order Regular Approximation

List of Figures

List of Tables

Chapter 1

General Introduction

Electron paramagnetic resonance (EPR) spectroscopy is one of the most powerful tools for investigating electronic and structural features of systems containing unpaired electrons, for example, radicals or coordination compounds. There are two major parameters derived from EPR spectra: hyperfine coupling constants (HFCCs) and $g-$tensors. While the HFCCs describe the interaction between the electron spin and magnetic field created by a nuclear spin, the $g-$tensors parameterize the interaction between the electron spin and homogeneous external magnetic field. Thus, the HFCCs provide the information about the electron spin density in vicinity of the given nuclei. On the other hand, the $g-$tensors are the property of an entire molecule. Beside experimental measurements, theoretical interpretations are also quite important not only for explaining what governs the observed spectra, but also for predicting parameters that are not easy to measure in experiment. Before introducing the main points of the present thesis, we will briefly recapitulate the previous calculations of EPR parameters using modern electronic structure methods.

1.1 Brief overview of EPR parameter calculations

1.1.1 Hyperfine coupling constants

Let us begin with discussing HFCCs. There are both isotropic and anisotropic contributions to HFCCs. The isotropic HFCC is typically associated with the spin density in the vicinity of the nuclei. This leads to the difficulties for numerically accurate prediction of HFCCs; therefore, the methods including both high-order correlation and relativity are often required in order to accurately predict HFCCs.

In non-relativistic limit, Bartlett and co-workers developed several approaches based on the coupled cluster (CC) method to evaluate the HFCCs, including finite-field CC [1] or analytical derivative CC [2]. Momose *et al.* [3, 4] employed the symmetry adapted cluster−configuration interaction (SAC−CI) method to evaluate the HFCCs of several organic radicals. Chipman systematically assessed the influence of excitation levels of the configuration interaction (CI) method for treatment of HFCCs for the CH radical [5], which revealed a non-monotonic variation of the isotropic HFCC value for the C center with increasing CI excitation levels. Engels [6, 7] developed a new selection procedure for multireference CI (MRCI) method in order to accurately characterize HFCCs of small molecules. The density functional theory has been also extensively used to calculate the HFCCs. Among the functionals tested, the hybrid functionals such as B3LYP [8, 9] and PBE0 [10, 11] are known to perform best in many cases. In a recent assessment of DFT performance, Kossmann *et al.* [12] has shown that the meta-GGA functional TPSS [13] (and its hybrid version TPSSh [13]) and the double hybrid functional B2PLYP [14] provide the HFCCs in acceptable agreement with experimental results.

Regarding the relativity, because the isotropic HFCC depends on the spin distribution in the closest vicinity of the nuclei, the scalar relativistic (SR) effects are quite important. The spin-orbit coupling (SOC) effect on HFCCs is often small and can be neglected. However, there are situations where it can be non-negligible. In framework of four component approach (4c), Quiney and Belanzoni [15] have employed the Dirac-Hartree-Fock (DHF) approximation to calculate HFCCs of diatomic molecules. Later, multi-configuration Dirac-Fock (MCDF) calculations were carried out by Song *et al.* [16] for coinage atoms. Malkin and coworkers [17] have recently implemented the 4c-DFT including the finite size nuclei for calculation of HFCCs. It is not doubtful that the 4c level of relativistic treatment can provide the accurate HFCCs; it is, however, too expensive when combined with high level of correlation treatment. Thus, the quasi-relativistic approaches have become the useful tools for HFCC calculations. Since the first work conducted by van Lenthe and colleagues [18], the zeroth-order regular approximation (ZORA) based DFT method has been widely used [19–22]. The implementation of second-order Douglas-Kroll-Hess (DKH2) transformation for HFCCs was first presented by Malkin and coworkers [23, 24]. Very recently, Sandhoefer and colleagues [25] have successfully applied the DKH2 transformation in combination with orbital-optimized second-order Møller-Plesset perturbation (OO-MP2) to calculation of HFCCs for transition metal complexes, which are difficult for DFT method. Filatov, Cremer and their coworker [26–28] have reported the calculations of HFCCs using infinite-order regular approximation (IORA) and normalized elimination of the small component (NESC) formalism in connection with high-level correlation methods, such as quadratic configuration interaction singles and doubles (QCISD) and CCSD.

1.1.2 Molecular $g-$tensors

We now turn to the $g-$tensors. There are two different ways of $g-$tensor calculations: the first-order and second-oder perturbation treatments. In the first one, the SOC is first included in the wavefunction and the Zeeman interaction is accounted for through the first-order degenerate perturbation theory within the ground state Kramers doublet. In the second one, the SOC and Zeeman interaction are included using the second-order perturbation theory, which is formulated with the linear response theory (LRT) or sum-over-states (SOS) expansion. It is worth emphasizing that the first-order perturbation approach includes the *full* SOC effects, while the second-order perturbation approach only includes the first-order (linear) SOC effects. In principle, the second-order approach can be applied to any multiplicity, while the first-order approach, which is based on the Kramers theorem, is limited to systems consisting of an odd number of electrons. Several recent works have been devoted to an extension of the first-order approach to any multiplicity.

DFT is the most popular quantum chemical method for $g-$tensor calculations. In the first-order approach, the DFT method is usually used in combination with the two-component (2c) relativistic Hamiltonian. For instance, van Lenthe *et al.* [29] used the ZORA Hamiltonian to treat SOC and SR effects. Neyman *et al.* [30] and Malkin *et al.* [31] reported their quasi-relativistic DKH implementations. The 4c-DFT method was also employed for $g-$tensor calculations, such as Komorovský *et al.* [32] and Repiský *et al.* [33]. Regarding the second-order approach, Ziegler and coworkers [34, 35] first implemented the linear response DFT (LR-DFT) for $g-$tensor calculations using the gauge-including atomic orbital (GIAO). Malkina, Kaupp and their coworkers [36, 37] reported the $g-$tensor calculations based on the SOS density functional perturbation theory (SOS-DFPT). Neese [38, 39] has proposed the coupled-perturbed Kohn-Sham (CP-KS) equation for EPR parameter predictions. Thereafter, Rinkevicius *et al.* [40] developed the spin-restricted open-shell DFT linear response theory (RDFT-LR). Recently, there have been several interesting studies making comparison between the performance of first- and second-order perturbation approaches based on DFT method, such as Hrobarik and colleagues [41], Autschbach and Pritchard [42], as well as Verma and Autschbach [43].

Since the earliest work carried out by Lushington and coworkers [44–47], *ab initio* methods have been widely used for $g-$tensor calculations. In the framework of the second-order perturbation approach, Vahtras *et al.* [48] initially implemented the LRT for the restricted open shell Hartree-Fock (ROHF) and the multiconfigurational self-consistent field (MCSCF). Later, Brownridge and colleagues [49] extended the SOS multireference configurattion interaction (SOS-MRCI) calculations, which was first used for small

molecules by Lushington and coworker [44–47], to medium-sized systems by more efficient implementation. Meanwhile, Neese [50] implemented and assessed a series of SOS-based *ab initio* methods. Thereafter, Neese [51] proposed the analytical derivative MRCI method that is equivalent to the untruncated SOS-MRCI. The complete active space second order perturbation based SOS (SOS-CASPT2) method was implemented by Vancoillie and colleagues [52]. Gauss and coworkers [53] recently reported a scheme for the calculation of $g-$tensors at the CC level. Regarding the first-order perturbation treatment, Bolvin [54] employed the spin-orbit restricted active space state interaction (SO-RASSI) procedure for CASPT2 as well as CC singles and doubles with perturbative triples [CCSD(T)] to evaluate $g-$tensors for a wide range of molecules. Tatchen and corworkers [55] developed the new route toward $g-$tensors based on the multireference spin-orbit configuration interaction (MRSOCI) method. The extension of the first-order perturbation approach based on the CASPT2 method to any multiplicity was also reported by Chibotaru and Ungur [56]. Most recently, Ganyushin and Neese [57] proposed an interesting approach, in which the SOC was variationally included in the complete active space self-consistent field theory (CASSCF) wavefution. This approach has been successfully applied to transition metal complexes. Meantime, Vad and colleagues [58] implemented the single-reference 4c-CI method to calculate the $g-$tensors for doublet radicals.

1.2 Scope of this thesis

Despite the recent progress, it is still important and challenging to provide highly reliable values of EPR paramters, even for small molecules, from quantum chemical calculations that are numerically convergent with respect to the level of the theoretical treatment. Therefore, the major purpose of this study is not to practically calculate EPR parameters using available methods, but to develop and/or assess the new methods for prediction of EPR parameters. The thesis begins with this general introduction followed by the next four chapters, which are central in the doctoral research, focusing on the prediction of molecular HFCCs and $g-$tensors using ab initio quantum chemistry methods based on the density matrix renormalization group (DMRG).

The DMRG method was introduced in condensed-matter physics by White [59, 60], and later applied to *ab initio* quantum chemical calculations [61–70]. The DMRG method has been shown to be an exceedingly efficient approach to a near "exact" [or full CI (FCI)] solution. In this algorithm, the molecular orbitals (MOs) are assigned to 1D quantum lattice sites. The tractable correlation length in the 1D lattice is controlled

by the number of renormalized basis states M, which affects the computational cost as $O(M^3k^3 + M^2k^4)$, where k refers to the number of MOs.

Although the DMRG method can be used in a brute-force way as a highly-scalable substitute for the FCI, recent studies have shown that it can be more practically used in combination with the complete active space (CAS) model to describe the multireference (or active-space) correlation. This active-space DMRG approach has been combined with the orbital optimization procedure [68, 71, 72] and is able to go far beyond the limitation of the traditional CASSCF method. In practical applications, the DMRG method has been shown to be successful for the prediction of molecular properties in large-scale multireference states [69, 73–82]. Most recently, Boguslawski *et al.* demonstrated that a reliable spin density can be calculated using the DMRG algorithm [83] and concluded that reliable reference spin densities can be obtained even if the total energies are not converged with respect to M.

In the Chapter 2, we have assessed the performance of ab initio DMRG in combination with complete active space (CAS) procedure, the CAS configuration interaction (CASCI), and the CASSCF for prediction of HFCCs of light radicals: BO, CO^+, CN, AlO, and C_2H_3. We found that the DMRG-CASSCF calculation with sufficiently large active space could provide the HFCCs in good agreement with experimental values, especially in the case of AlO radical that seems to be formidable for conventional methods. In order to get insight into the accuracy of DMRG calculations, the orbital contributions to the total spin were analyzed at a given nucleus. We also assessed the performance of DMRG method by calculating HFCCs at various numbers of renormalized states M. We found that the DMRG calculations with $M = 512$ were capable of giving the reliable HFCCs for our test cases.

In the Chapter 3, as a continuation of the Chapter 2, we have evaluated the HFCCs of radicals containing a single heavy element using the DMRG method that takes into account SR effects. The quasi-relativistic Douglas-Kroll-Hess (DKH) transformation has been applied to both Hamiltonian and hyperfine coupling operator. To our best knowledge, this study is the first to present the HFCCs at the DKH3 level of scalar relativistic treatment, which was found crucial to obtain converged results. As test cases, we applied the DMRG-CASSCF/DKH3 implementation to evaluate HFCCs of 4d transition metals: Ag atom, Pd in PdH radical, and Rh in RhH_2 radical. Our calculated values were in good agreement with experimental values.

In the Chapter 4, the molecular $g-$tensors were evaluated using CASSCF method. As the first step before employing the DMRG-CASSCF method for $g-$tensor calculation provided in the next chapter, the conventional FCI method was used to describe the correlation in active space. We have employed two technical approaches. The first is the

quasi-degenerate perturbation theory (QDPT). The second is the analytical response theory based on coupled-perturbed (CP) equation. We have made the comparison between the performance of CP- and QDPT-CASSCF approaches for some heavy doublet radicals. Although the CP-CASSCF approach can include all excited states expanded in active space, it is limitated to weak SOC cases. The QDPT-CASSCF approach with truncated state expansion, however, can be applied for systems with strong SOC. Apart from the perturbation treatment, the SOC treatment is also important for the accuracy of $g-$tensor calculations. In this work, we employed the flexible nuclear screening spin-orbit (FNSSO) approximation, which has been very recently developed by Chalupský and Yanai [84]. The $g-$tensor calculations of a test set including 20 small light radicals were first performed. Next, we evaluated the $g-$tensor of 5 radicals including heavy atoms.

In the Chapter 5, a new approach for molecular g-tensors based on the analytical response theory for DMRG, referred to as CP-DMRG, was implemented. The CP-DMRG method has been recently proposed by Dorando, Hachmann, and Chan [85] for electric field related properties. In this Chapter, we will provide our formulation for the case of molecular $g-$tensors. The algorithm for implementation will be also provided.

In the Chapter 6, a mean-field (or one-particle) theory to represent electron correlation at the level of the MP2 theory has been formulated and implemented. Orbitals and associated energy levels are given as eigenfunctions and eigenvalues of the resulting one-body (or Fock-like) MP2 Hamiltonian, respectively. They are optimized in the presence of MP2-level correlation with the self-consistent field procedure and used to update the first-order Møller-Plesset perturbation (MP1) amplitudes including their denominators. Numerical performance was illustrated in molecular applications for computing reaction energies, applying Koopmans' theorem, and examining the effects of dynamic correlation on energy levels of metal complexes.

Finally, the general conclusion will be provided in Chapter 7.

Chapter 2

Non−relativistic DMRG calculations of HFCCs for light molecules: diatomic $^2\Sigma$ and vinyl radicals as test cases

T. N. Lan, Y. Kurashige, T. Yanai,

2.1   Introduction

In this chapter, we attempt to use the DMRG method with large active space to include near convergent electron correlation in the HFCC calculations. For light element molecules, the SOC effects are small and can be neglected, so that the HFCCs are dominated by the Fermi contact (FC) term [86] and the spin-dipole (SD) interaction term [87]. This work serves as the initial application of the DMRG algorithm in combination with CASCI and CASSCF methods for computing the HFCCs, the FC and SD terms. The electron correlation effects on the computed HFCC values are systematically investigated using various levels of active space, which are increasingly extended from the single valence space to the large model space entailing double valence and at least single polarization shells. In addition, the core correlation is treated by including the core orbitals in active space. High-accuracy wavefunctions are obtained using the

DMRG-CASCI and DMRG-CASSCF calculations with large-size active space. The exact diagonalization with such active space can be achieved only by the DMRG method. The dependence of the formulas for the FC and SD terms on the DMRG wavefunction arises through the spin density. The DMRG with enlargement of the active space delivers convergence of the spin density to a FCI-quality description. To achieve further insights into the accuracy of HFCC calculations, the orbital contributions to the total spin density are analyzed at a given nucleus, which is directly related to the FC term and is numerically sensitive to the level of correlation treatment and basis set.

In this study, assessment of the DMRG method for HFCC calculations is first performed on small $^2\Sigma$ radicals: BO, CO^+, CN, and AlO. Although these test molecules are small in size, determination of their HFCCs is considered to be important from both experimental and computational perspectives. Moreover, it is of significant value to provide theoretical results with near exact accuracy that can serve as benchmark data. The HFCCs of BO and CO^+ have been well characterized by the conventional methods, namely DFT and CC, to an acceptable accuracy with respect to the experimental values. However, the determination of HFCCs for the CN and AlO molecules is a challenge for the computational approaches. The difficulties are that the unrestricted treatment for CN suffers from a large degree of spin contamination [88], and the delicate balance between the ionic states of AlO must be handled carefully in the electronic structure calculations [89–93]. Finally, to explore the performance of present approach for HFCC prediction of multi-atomic organic radicals, we evaluate the HFCCs of vinyl (C_2H_3) radical. We concomitantly address the following questions of technical interest: (i) Can HFCCs be accurately described by the active-space wavefunction? (ii) What type of orbitals should be included in active space for HFCC calculations? We attempt to address these issues using the active-space DMRG method.

The chapter is organized as follows. In Sec. 2.2, we briefly discuss the background of quantum chemical calculations for the hyperfine coupling tensors. The computational details are shown in Sec. 2.3. The results are presented and discussed in Sec. 2.4. Finally, a summary and concluding remarks are given in Sec. 2.5.

2.2 Theoretical background

2.2.1 Hyperfine coupling tensor

The hyperfine coupling tensor $\mathbf{A}$ is parameterized by a phenomenological spin Hamiltonian that describes the interaction between electron spin $\mathbf{s}$ and nuclear spin $\mathbf{I}$:

$$\hat{H}_{SI} = \mathbf{s} \cdot \mathbf{A} \cdot \mathbf{I}. \tag{2.1}$$

In the absence of SOC, this Hamiltonian contains two terms; the FC Hamiltonian [86]

$$\hat{H}_{FC} = \frac{8\pi}{3} g_e \beta \sum_K g_K \beta_K \sum_i \left[\delta\left(r_{iK}\right) \mathbf{s}_i \mathbf{I}^{(K)} \right], \tag{2.2}$$

and the SD Hamiltonian [87]

$$\hat{H}_{SD} = g_e \beta \sum_K g_K \beta_K \sum_i \left[\frac{\mathbf{s}_i \mathbf{I}^{(K)}}{r_{iK}^3} - 3 \frac{\left(\mathbf{s}_i \mathbf{r}_{iK}\right)\left(\mathbf{I}^{(K)} \mathbf{r}_{iK}\right)}{\mathbf{r}_{iK}^5} \right], \tag{2.3}$$

where K and i run over the number of nuclei and electrons, respectively. The constant g_e is the g-value of a free electron ($g_e = 2.002319$), β is the Bohr magneton, g_K and β_K are the nuclear g-value and nuclear magneton of a given nucleus K, respectively. $\mathbf{r}_{iK}(= (r_{iK,x}, r_{iK,y}, r_{iK,z}))$ is the relative position vector between the i-th electron and K-th nucleus. The symbol $\delta(...)$ refers to the Dirac delta function. The $\mathbf{A}$ tensor of nucleus K is obtained by taking the second derivative of the spin Hamiltonian with respect to electron and nuclear spins:

$$\mathbf{A}^{(K)} = \frac{\partial^2 \hat{H}_{SI}}{\partial \mathbf{s}\, \partial \mathbf{I}}. \tag{2.4}$$

This can be expressed as the decomposed form:

$$\mathbf{A}^{(K)} = \mathbf{A}^{(K;c)} + \mathbf{A}^{(K;d)}, \tag{2.5}$$

with the FC tensor $\mathbf{A}^{(K;c)}$,

$$A_{kl}^{(K;c)} = \delta_{kl} \frac{8\pi}{3} \frac{P_K}{2S} \sum_{\mu\nu} P_{\mu\nu}^{(\alpha-\beta)} \langle \chi_\mu | \delta(r_{iK}) | \chi_\nu \rangle, \tag{2.6}$$

and the SD tensor $\mathbf{A}^{(K;d)}$,

$$A_{kl}^{(K;d)} = \frac{P_K}{2S} \sum_{\mu\nu} P_{\mu\nu}^{(\alpha-\beta)} \langle \chi_\mu | r_{iK}^{-5} (r_{iK}^2 \delta_{kl} - 3 r_{iK,k} r_{iK,l}) | \chi_\nu \rangle, \tag{2.7}$$

where $k, l = x, y, z$; $P_K(= g_e \beta g_K \beta_K)$ is the nucleus-type constant, and S is the total spin. The one-particle integrals $\langle \chi_\mu | \cdots | \chi_\nu \rangle$ in Eqs. (2.6) and (2.7) are represented in atomic orbital (AO) basis χ_μ and χ_ν. The FC integral is regarded as the overlap distribution at the nuclear point K. The implementation of the SD integral is more complicated than that of the FC integral. The SD integral was implemented using the Rys-quadrature algorithm [94]. The matrix $P_{\mu\nu}^{(\alpha-\beta)}$ is the difference between the α and β electron density matrices in the AO basis representation, which is referred to as the AO spin density matrix.

2.2.2 Spin density analysis

The spatially resolved spin density can be given by

$$
\rho^{(\alpha-\beta)}(\mathbf{r}) = \sum_{\mu\nu} P_{\mu\nu}^{(\alpha-\beta)} \chi_\mu(\mathbf{r}) \chi_\nu(\mathbf{r})
$$

$$
= \sum_{\mu\nu} \sum_{pq}^{\mathrm{MO}} D_{pq}^{(\alpha-\beta)} c_{p\mu} c_{q\nu} \chi_\mu(\mathbf{r}) \chi_\nu(\mathbf{r}) , \tag{2.8}
$$

where the matrix $D_{pq}^{(\alpha-\beta)}$ is the spin density matrix represented in the given MO basis, thus referred to as the MO spin density matrix, and $c_{p\mu}$ are the MO coefficients. Diagonalization of the MO spin density matrix leads to the so-called spin natural orbitals (SNOs). Let $n_i^{(\alpha-\beta)}$ and U_{ip} be its eigenvalues and eigenvectors, respectively, so that we have $\sum_{pq} U_{ip} U_{jq} D_{pq}^{(\alpha-\beta)} = \delta_{ij} n_i^{(\alpha-\beta)}$. The MO coefficients of the SNOs, $\{\bar{c}_{i\mu}\}$, can be obtained from the unitary transformation of $\{c_{p\mu}\}$ as

$$
\bar{c}_{i\mu} = \sum_p^{\mathrm{MO}} U_{ip} c_{p\mu} . \tag{2.9}
$$

This definition is analogous to that for the natural orbitals (NOs) obtained by diagonalization of the density matrix. The eigenvalue $n_i^{(\alpha-\beta)}$ is called the spin occupation number of the i-th SNO. The spatially resolved spin density $\rho^{(\alpha-\beta)}(\mathbf{r})$ [Eq. (2.8)] can be rewritten using the SNO basis as follows:

$$
\rho^{(\alpha-\beta)}(\mathbf{r}) = \sum_i^{\mathrm{SNO}} \sum_{\mu\nu} n_i^{(\alpha-\beta)} \bar{c}_{i\mu} \bar{c}_{i\nu} \chi_\mu(\mathbf{r}) \chi_\nu(\mathbf{r}) . \tag{2.10}
$$

Finally, it can be written as the summation of individual SNO contributions:

$$
\rho^{(\alpha-\beta)}(\mathbf{r}) = \sum_i^{\mathrm{SNO}} \rho_i^{(\alpha-\beta)}(\mathbf{r}) , \tag{2.11}
$$

where $\rho_i^{(\alpha-\beta)}(\mathbf{r})$ is the spatial distribution of the spin density associated with the i-th SNO, given by

$$\rho_i^{(\alpha-\beta)}(\mathbf{r}) = n_i^{(\alpha-\beta)} \sum_{\mu\nu} \bar{c}_{i\mu}\, \bar{c}_{i\nu} \chi_\mu(\mathbf{r})\, \chi_\nu(\mathbf{r}) \,. \qquad (2.12)$$

The SNO analysis is useful to identify those MOs that primarily contribute to the spin density at the nucleus.

2.3   Computational details

The FC and SD terms were calculated using Eqs. (2.6) and (2.7), respectively. These formulas clearly show that the accuracy of HFCCs is essentially determined by that of the calculated spin density $\rho^{(\alpha-\beta)}(\mathbf{r})$ [Eq. (2.8)]. In the present work, the spin density was evaluated from the CAS-type wavefunctions. The active spaces used in this work are presented in Table 2.1. The DMRG code implemented by our group [70] was employed to obtain the active-space wavefunction for active space involving more than 16 orbitals; otherwise, the FCI procedure was used. The number of spin adapted renormalized states M was set to 512 in all DMRG calculations. We have implemented the spin adaptation of Zgid and Nooijen [67] in our DMRG code; therefore, the number of actual bases that are not spin adapted is much larger than M (approximately twice). The numerical convergence of HFCCs with respect to M will be discussed later (Sec. 2.4.5).

TABLE 2.1: Active orbitals.

Molecule	Active space	Active orbitals	
BO, CO$^+$, and CN	CAS(9e,8o)	B, C, O, N: $2s2p$	
	CAS(9e,16o)	B, C, O, N: $2s2p3s3p$	
	CAS(9e,28o)	B, C, O, N: $2s2p3s3p4s3d$	
	CAS(13e,30o)	B, C, O, N: $1s2s2p3s3p4s3d$	
AlO	CAS(9e,8o)	Al: $3s3p$	O: $2s2p$
	CAS(9e,16o)	Al: $3s3p3d$	O: $2s2p3p$
	CAS(9e,21o)	Al: $3s3p3d$	O: $2s2p3p, 3d$
	CAS(15e,28o)	Al: $2p3s3p3d4p$	O: $2s2p3s3p3d$
	CAS(21e,31o)	Al: $1s2p3s3p3d4p$	O: $1s2s2p3s3p3d$
	CAS(15e,33o)	Al: $2p3s3p3d4p4d$	O: $2s2p3s3p3d$
	CAS(21e,36o)	Al: $1s2s2p3s3p3d4p4d$	O: $1s2s2p3s3p3d$
C$_2$H$_3$	CAS(15e,33o)	C: $1s2s2p3s3p4s3d$	H: $1s$

For the diatomic radicals, the canonical HF MOs were used as the initial orbitals. For vinyl radical, however, the initial orbitals were obtained from the restricted active space SCF (RASSCF) calculation including single and double excitations from RAS1 to RAS3 (singly occupied orbital was included in RAS2 space). The basis sets for this calculation are ANO-L [95, 96] with $4s2p1d$ and $1s$ contractions for C and H atoms, respectively. The program package MOLCAS [97] was used for this purpose.

TABLE 2.2: Bond lengths of $^2\Sigma$ diatomic radicals used to calculate the HFCCs.

Molecule	Bond length (Å)	
	Present work[a]	Neese *et al.*[b]
BO	1.2049	1.2049
CO^+	1.1500	1.1105
CN	1.1718	1.1555
AlO	1.6176	1.6176

[a] Ref. [98].
[b] Ref. [38].

For comparison, the HFCCs were also calculated using the DFT and CCSD methods. The ORCA code[99] was used for DFT calculations with three functionals; the hybrid-GGA functional B3LYP, meta-GGA functional TPSS, and pure-GGA functional BP86.[100, 101] The CCSD calculations were performed using the GAUSSIAN 09 program package[102] without the frozen core approximation.

Table 2.2 shows the geometries of diatomic molecules used in these calculations, which were adopted from experimental measurements [98]. As a reference, these include the geometries employed in the previous work of Neese and colleagues [12, 38, 103]. The molecular structure of vinyl radical is shown Figure 2.1. Because not even an approximate experimental structure has been reported for this radical, we use the geometry theoretically recomended by Peterson and Dunning [104] as follows: $r(\text{C1C2}) = 1.3102$ Å, $r(\text{C1H1}) = 1.0773$ Å, $r(\text{C2H2}) = 1.0830$ Å, $r(\text{C2H3}) = 1.0881$ Å, $a(\text{C2C1H1}) = 137.0°$, $a(\text{H2C2C1}) = 122.0°$, $a(\text{H3C2C1}) = 121.3°$.

The point-group symmetry of molecules are C_{2v} and C_s for diatomic and vinly radicals, respectively.
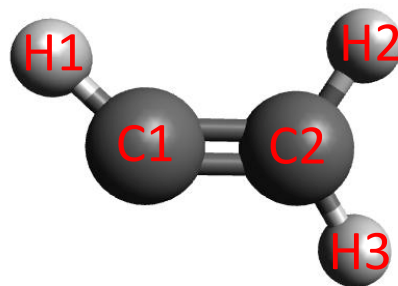
FIGURE 2.1: Molecular structure of vinyl (C_2H_3) radical.

2.4 Results and discussion

2.4.1 BO and CO^+ radicals

HFCC calculations were first performed for the BO and CO^+ radicals, which have been well characterized by the DFT and CC methods. The EPR-type basis sets reported by Barone and coworkers[105] in combination with appropriate functionals are known to generally provide reasonable HFCCs for organic radicals. On the other hand, the ANO-type basis sets by Roos and colleagues have been widely used for the construction of correlated molecular wavefunctions; however, the performance for HFCCs calculations has not yet been tested. Thus, the HFCCs of the BO and CO^+ radicals were evaluated here using both EPR-III and ANO-L-TZP basis sets. For the BO radical, the total number of AOs for the EPR-III and ANO-L-TZP basis sets is 69 and 60, respectively, while that for CO^+ is 80 and 60, respectively. The calculated values of the HFCCs are summarized in Tables 2.3 and 2.4. The experimental gas-phase and Ne-matrix HFCCs available for BO[106–109] and CO^+[110–112] are presented. The gas-phase and Ne-matrix values for the B center are not so different, while those for the C center differ significantly. The DFT/EPR-III and CCSD/EPR-III results for the BO radical are basically consistent with the previous results reported by Neese and coworkers,[12, 103] while those for CO^+ are not. This inconsistency for CO^+ can be attributed to the difference in geometry used between the present and previous calculations, as shown in Table 2.2.

Fermi contact term. Herein, let this analysis focus on the HFCCs of less electronegative atom centers, i.e. the B and C centers. The CCSD results with the EPR-III basis set for these centers are comparable with the experimental values and the errors with respect to the gas-phase values for the B and C centers are 1.37 and 3.44%, respectively. Among the DFT functionals, the B3LYP functional generally provides the best

results. The BP86 and TPSS functionals yield FC terms for the B center that are in good agreement with the experimental results, while those for the C center are largely underestimated.

We now move to the results of the CASCI and CASSCF calculations. For the CASCI calculations, the effect of core correlation seems to be negligible, and the FC term is significantly decreased for both the B and C centers with enlargement of the active space, which results in underestimation with the DMRG-CASCI calculations. The CASSCF results clearly show that the active space with full valence shells alone is insufficient for reliable prediction of the HFCCs. In the presence of the polarization shell but without core correlation, the orbital optimization in the CASSCF calculations provides only a marginal improvement upon the CASCI results. In contrast, the FC term is significantly increased when the core correlation is taken into account. The FC term obtained by DMRG-CASSCF(13e,30o)/EPR-III is in excellent agreement with the experimental gas-phase values and the errors for the B and C centers are 0.87 and 0.99%, respectively.

Concerning the basis set, the values for the FC terms obtained with ANO-L-TZP are far from experimental values. This inadequacy of ANO-L-TZP for HFCC prediction is associated with contraction of the ANO-type basis sets, which are too contracted in the s-shells. Thus, the ANO-type basis set is not sufficiently flexible to properly describe the spin-polarization of the core region. To confirm that the EPR-III basis set provides convergent basis set descriptions, HFCC calculations were performed with the uncontracted ANO-L-TZP basis set (Table 2.5). The total number of AOs for this uncontracted basis set is 164 for both BO and CO^+ radicals, which indicates that it is much larger and more flexible than the EPR-III basis set. Table 2.5 shows that the HFCC values obtained with the EPR-III and uncontracted ANO-L-TZP basis sets are comparable; therefore, it can be concluded that the basis set error in EPR-III is negligible for these $^2\Sigma$ radicals.

The spin density at the nuclear centers was analyzed using SNOs to determine the dependence of the FC term on the active space and the orbital optimization in more detail. Table 2.6 shows the contributions to the total spin density from the SNO with the largest spin occupation number (SON) and from the other SNOs at each of the B and C centers obtained with the EPR-III basis set. The eigenvector elements U_{ip} for construction of the SNO with the largest SON reveal that it is dominantly composed of a singly occupied MO (SOMO) and is thus regarded as a singly occupied SNO (SOSNO). The total spin density at the nuclei centers is dominated by the SOSNO because the remaining SNOs have negligible spin occupancies. For the CASCI calculation, enlargement of the active space depresses the net spin density associated with the SOSNO. The contribution from the SNOs other than the SOSNO to the spin density is relatively small. The total spin

TABLE 2.3: HFCCs (in MHz) for the ^{2}BO molecule obtained with the EPR-III and ANO-L-TZP basis sets, where the total numbers of AOs are 69 and 60, respectively.

Method	^{11}B		^{17}O	
	$A^{(K;c)}$	$A_{11}^{(K;d)}$	$A^{(K;c)}$	$A_{11}^{(K;d)}$
EPR-III				
CASCI(9e,8o)	966.29	−28.11	−23.72	12.28
CASCI(9e,16o)	920.81	−25.29	−12.08	16.95
DMRG-CASCI(9e,28o)	903.81	−24.98	−2.43	18.84
DMRG-CASCI(13e,30o)	904.59	−25.02	−2.94	18.83
CASSCF(9e,8o)	916.85	−26.72	−19.02	19.80
DMRG-CASSCF(9e,28o)	912.09	−24.22	−5.67	21.07
DMRG-CASSCF(13e,30o)	1018.33	−24.44	−11.95	20.84
B3LYP	1074.79	−27.80	−11.66	21.42
TPSS	990.76	−27.04	−5.70	25.20
BP86	989.79	−26.84	−7.73	23.32
CCSD	1041.15	−24.87	−11.96	21.68
ANO-L-TZP				
CASCI(9e,8o)	969.42	−28.44	−39.44	8.93
CASCI(9e,16o)	911.81	−24.76	−26.30	17.60
DMRG-CASCI(9e,28o)	885.48	−23.13	−32.44	19.43
DMRG-CASCI(13e,30o)	901.80	−23.19	−30.06	19.44
FCI-CASSCF(9e,8o)	895.24	−25.86	−31.70	19.95
DMRG-CASSCF(9e,28o)	901.54	−23.33	−24.07	20.89
DMRG-CASSCF(13e,30o)	930.68	−23.55	−24.58	20.92
B3LYP	1015.79	−25.90	−32.21	21.82
TPSS	928.40	−25.30	−22.84	25.47
BP86	929.68	−24.95	−25.27	23.73
CCSD	958.07	−23.52	−30.58	21.88
Exp − gas-phase [a]	1027	−27	n/a	
Exp − Ne-matrix [b]	1033	−25	−19	12

[a] Ref. [106];
[b] Ref. [107–109]

TABLE 2.4: HFCCs (in MHz) for the $^2CO^+$ molecule obtained with the EPR-III and ANO-L-TZP basis sets, where the total numbers of AOs are 80 and 60, respectively.

Method	^{13}C		^{17}O	
	$A^{(K;c)}$	$A_{11}^{(K;d)}$	$A^{(K;c)}$	$A_{11}^{(K;d)}$
EPR-III				
CASCI(9e,8o)	1469.96	−48.44	−7.87	29.14
CASCI(9e,16o)	1450.21	−47.84	1.84	30.24
DMRG-CASCI(9e,28o)	1410.98	−47.68	19.88	33.77
DMRG-CASCI(13e,30o)	1409.23	−47.72	20.01	33.78
CASSCF(9e,8o)	1431.59	−46.13	25.37	38.00
DMRG-CASSCF(9e,28o)	1396.59	−44.14	26.56	38.73
DMRG-CASSCF(13e,30o)	1492.96	−44.82	32.60	38.55
B3LYP	1548.21	−50.08	39.73	44.02
TPSS	1444.78	−49.26	39.73	47.10
BP86	1439.34	−50.22	37.39	44.44
CCSD	1557.75	−43.63	32.87	42.78
ANO-L-TZP				
CASCI(9e,8o)	1396.95	−47.39	−10.88	29.19
CASCI(9e,16o)	1365.90	−46.27	4.55	31.85
DMRG-CASCI(9e,28o)	1314.59	−45.99	32.98	35.64
DMRG-CASCI(13e,30o)	1296.20	−46.11	32.12	35.61
CASSCF(9e,8o)	1360.59	−45.29	19.66	37.76
DMRG-CASSCF(9e,28o)	1318.98	−43.48	14.57	38.44
DMRG-CASSCF(13e,30o)	1348.58	−43.72	20.24	38.31
B3LYP	1435.01	−47.80	29.27	43.71
TPSS	1331.67	−47.07	31.79	46.71
BP86	1338.13	−47.88	29.49	44.06
CCSD	1425.84	−42.03	18.53	42.30
Exp − gas-phase [a]	1506	−46	n/a	
Exp − Ne-matrix [b]	1573	−49	19	33

[a] Ref. [110];
[b] Ref. [111, 112]

density thus decreases with enlargement of the active space, which leads to a decrease in the values of the FC terms for the B and C centers. From a comparison of the results from the DMRG-CASCI(9e,28o) and DMRG-CASCI(13e,30o) calculations, i.e. with and without two $1s$ orbitals in CAS, it was concluded that the core correlation does not induce any significant change in the total spin density with the CASCI calculation.

TABLE 2.5: HFCCs (in MHz) for the B center in ^{2}BO and the C center in ^{2}CO$^+$ radicals with the uncontracted ANO-L basis set, where the total number of AOs is 164 for both radicals.

Center	Method	$A^{(K;c)}$	$A_{11}^{(K;d)}$
	B3LYP	1072.80	−28.16
	TPSS	982.71	−27.53
B in BO	BP86	986.66	−27.47
	CCSD	1041.70	−25.28
	DMRG-CASSCF(13e,30o)	1028.41	−24.34
	B3LYP	1542.81	−50.38
	TPSS	1430.26	−49.61
C in CO$^+$	BP86	1432.74	−50.77
	CCSD	1554.42	−43.85
	DMRG-CASSCF(13e,30o)	1493.89	−44.22

Let us discuss the orbital optimization effects on the spin density that arise from the CASSCF procedure. A comparison is made between two large CAS calculations; DMRG-CASSCF(9e,28o) and DMRG-CASSCF(13e,30o). The spin density associated with the SOSNO from the two DMRG-CASSCF calculations is similar, whereas that with the other SNOs significantly increases with inclusion of the two $1s$ orbitals in the CAS method. This indicates that the core correlation leads to strong enhancement of the total spin densities at nuclei centers. The poor agreement of DMRG-CASSCF(9e,28o) with the experiment data was significantly improved with DMRG-CASSCF(13e,30o).

Finally, we briefly discuss the FC term for the O center. The HFCCs of an electronegative atom is difficult to experimentally measure in the gas-phase; therefore, the calculation results are compared with Ne-matrix measurements. The errors of the DMRG-CASSCF(13e,30o)/EPR-III results relative to the experimental values are 7.04 and 13.60% for the O center in the BO and CO$^+$ radicals, respectively. The results obtained with CCSD are very close to those with DMRG-CASSCF(13e,30o), especially for the EPR-III basis set.

Spin-dipole term. The elements of SD tensors are shown in Tables 2.3 and 2.4 for the B and C centers, respectively. The general conclusion is that the SD term is less

TABLE 2.6: SNO contributions to spin density (in a.u.) at the B (BO) and C (CO$^+$) centers. The values in parentheses indicate the SON of SOSNO. For the CASSCF calculations, only the two largest active spaces are compared. Only the results of the EPR-III basis set are presented.

Center	Method	Contribution of SOSNO	Sum of the other SNO contributions	Total
B	CASCI(9e,8o)	0.6722 (*0.9870*)	0.0012	0.6734
	CASCI(9e,16o)	0.6325 (*0.9716*)	0.0089	0.6414
	DMRG-CASCI(9e,28o)	0.6209 (*0.9693*)	0.0086	0.6295
	DMRG-CASCI(13e,30o)	0.6291 (*0.9694*)	0.0011	0.6302
	DMRG-CASSCF(9e,28o)	0.6238 (*0.9700*)	0.0120	0.6358
	DMRG-CASSCF(13e,30o)	0.6213 (*0.9725*)	0.0880	0.7097
C	CASCI(9e,8o)	1.2892 (*0.9577*)	0.0120	1.3076
	CASCI(9e,16o)	1.2664 (*0.9553*)	0.0236	1.2900
	DMRG-CASCI(9e,28o)	1.2394 (*0.9529*)	0.0157	1.2551
	DMRG-CASCI(13e,30o)	1.2398 (*0.9530*)	0.0139	1.2537
	DMRG-CASSCF(9e,28o)	1.2127 (*0.9509*)	0.0297	1.2424
	DMRG-CASSCF(13e,30o)	1.2385 (*0.9525*)	0.0942	1.3334

dependent on the basis set and the active space than the FC term. The SD term converges smoothly with enlargement of the active space. The core correlation does not affect the SD term. With enlargement of the active space, the values of the SD term for the B and C centers decrease, while those for the O center increase for both radicals. The CCSD results are generally close to those obtained with DMRG-CASSCF(13e,30o). For the B center, the error of the SD term calculated by DMRG-CASSCF(13e,30o)/EPR-III with respect to that from Ne-matrix measurements (2.24%) is smaller than that from gas-phase measurements (9.48%). In contrast, the DMRG-CASSCF(13e,30o)/EPR-III results for the C center are in better agreement with the gas-phase value (2.56% error) than with the Ne-matrix value (8.53% error). Unfortunately, all the values presented herein are largely overestimated with respect to the Ne-matrix values for the O centers in both radicals.

To summarize, the performance of the DMRG method for the prediction of HFCCs for BO and CO$^+$ radicals, which can be accurately described by DFT and CC methods, was assessed. While the DMRG-CASCI calculations gave results that were in poor agreement with the experimental values, the DMRG-CASSCF calculations with orbital optimization and inclusion of the core correlation were in excellent agreement with the gas-phase measurements for the FC terms of the less electronegative centers.

2.4.2   CN radical

Momose *et al.* [4] first used the SAC-CI method to calculate the HFCCs of the CN radical and the results compared favorably with the experimental results. However, as shown later by Fernandez *et al.* [113], this agreement was fortuitous and resulted from cancellation of the basis set and correlation errors. These authors employed the multiconfiguration self-consistent-field (MCSCF) restricted-unrestricted (RU) response function method [114] to evaluate HFCCs for the CN radical. In this approach, although the spin polarization of the core orbitals cannot be described by the MCSCF wavefunction itself, it was perturbatively addressed by the response term. Accurate HFCCs for the CN radical were generally obtained with an appropriate conjunction between the active space and basis set. Gauld *et al.* [88] found that the QCISD approach with perturbative triples [QCISD(T)] underestimated the FC term of this radical. Nevertheless, good agreement with the experimental value was obtained when the CCSD(T) method was employed in place of QCISD(T). Neese and colleagues [12] recently reported that the double hybrid functional B2PLYP does not accurately characterize the HFCCs of the CN radical. In their later work [103], the OO-MP2 method provided the HFCCs in acceptable agreement with the experimental values for many molecules, while it failed for the CN radical. From the previous subsection, the ANO-L-TZP basis set was deemed inadequate for HFCC prediction, so that only the results obtained with the EPR-III basis set were presented. The total number of AOs is 80. All results are summarized in Table 2.7. Experimental gas-phase values for the CN radical are not available; therefore, Ne-matrix values [115] were used as references. The CCSD results of the present work are consistent with those reported by Kossmann and Neese [103], where the same basis set (EPR-III), but different geometry, was used (see Table 2.2). Based on this consistency, we also adopted their CCSD(T) results [103] for further consideration.

Fermi contact term. Here, we mainly focus on the less electronegative center, i.e., the C center. For the DFT calculations, the TPSS and BP86 functionals largely underestimate the FC term for the C center with errors of 14.29 and 15.99%, respectively. For the CC methods, CCSD overestimates the FC term for the C center with errors of up to 11.39%. However, with inclusion of the perturbative triples, the error is decreased to 5.43%.

Regarding the CASCI calculations, the FC term for the C center is rapidly decreasing with enlargement of the active space. As the active space is extended from CAS(9e,28o) to CAS(13e,30o), the error is decreased from 19.20 to 16.60%. For the DMRG-CASSCF calculations, the FC term also converges smoothly with respect to the active space. By relaxing the orbitals with 1s orbitals in the active space, the error with respect to the experimental value is reduced to 4.43%. It is worth noting that the CCSD(T) and

TABLE 2.7: HFCCs (in MHz) for the ^{2}CN molecule obtained with EPR-III basis set, where the total number of AOs is 80. For comparison, the CCSD and CCSD(T) results from Kossmann and Neese's work were also adopted, where the same basis set was used, but with a slightly different geometry (see Table 2.2).

Method	^{13}C		^{14}N	
	$A^{(K;c)}$	$A_{11}^{(K;d)}$	$A^{(K;c)}$	$A_{11}^{(K;d)}$
CASCI(9e,8o)	936.03	−62.25	8.78	−8.78
CASCI(9e,16o)	767.11	−53.93	3.70	−13.63
DMRG-CASCI(9e,28o)	700.91	−54.34	9.04	−15.51
DMRG-CASCI(13e,30o)	685.66	−54.37	8.18	−15.52
CASSCF(9e,8o)	629.40	−51.06	−19.72	−17.90
DMRG-CASSCF(9e,28o)	596.48	−52.33	−3.42	−19.22
DMRG-CASSCF(13e,30o)	561.95	−52.92	−20.14	−19.28
B3LYP	572.62	−59.93	−18.90	−21.66
TPSS	504.83	−59.34	−16.35	−22.12
BP86	494.08	−59.47	−13.65	−21.58
CCSD [a]	655.27	−52.97	−20.03	−19.84
CCSD [b]	655.40	−53.00	−20.00	−19.80
CCSD(T) [b]	556.10	−56.70	−18.30	−19.10
Exp − Ar-matrix [c]	588	−45	−13	−15

[a] Present work
[b] Kossmann and Neese, Ref. [103]
[c] Ref. [115]

DMRG-CASSCF(13e,30o) results are very close together. This means that the DMRG-CASSCF(13e,30o) has captured the high-order correlation, which is required for the accuracy of the FC term for the C center in the CN radical.

The SNO contributions to the total spin density are analyzed next. Table 2.8 shows the SOSNO contribution and the summation of the other SNO contributions to the total spin density at the C center. The SOSNO spin density rapidly decreases with enlargement of the active space in the CASCI calculations, while the increase in the summation of the other SNO spin densities is relatively slow. Consequently, the total spin density at the C center decreases. For the CASSCF calculations, the orbital relaxation lowers the SOSNO spin density relative to that of the CASCI calculations. While the SOSNO spin densities from the DMRG-CASSCF(9e,28o) and DMRG-CASSCF(13e,30o) calculations are comparable, the summation of the other SNO spin densities from the latter is much smaller than from the former. Therefore, in contrast to the BO and CO$^+$ radicals, the core correlation in the CN radical reduces the summation of the other SNO spin densities.

TABLE 2.8: SNO contributions to spin density (in a.u.) at the C center in the CN radical. The values in parentheses indicate the SON of SOSNO. For the CASSCF calculations, only the two largest active spaces are compared.

Method	Contribution of SOSNO	Sum of the other SNO contributions	Total
CASCI(9e,8o)	0.8223 (*0.9948*)	0.0103	0.8326
CASCI(9e,16o)	0.6373 (*0.9501*)	0.0480	0.6823
DMRG-CASCI(9e,28o)	0.5312 (*0.9439*)	0.0922	0.6235
DMRG-CASCI(13e,30o)	0.5278 (*0.9440*)	0.0822	0.6099
DMRG-CASSCF(9e,28o)	0.4706 (*0.9364*)	0.0604	0.5310
DMRG-CASSCF(13e,30o)	0.4800 (*0.9372*)	0.0194	0.4996

We also provide a brief comment here with regard to the FC term for the N center. For the CASCI calculations, the FC term of the N center is completely wrong, even the sign, and this remains unchanged with changes in the active space. Although the DMRG-CASSCF(9e,28o) calculation can give the correct sign of the FC term, the error of the result with respect to the experimental value is as large as 76.92%. The DMRG-CASSCF(13e,30o) calculation improves the FC term to some degree, but the value is still far from the experimental result with an error of up to 54.92%. In addition, the CC results are very close to that obtained with the DMRG-CASSCF(13e,30o) calculation.

Spin-dipole term. The calculated SD terms are also presented in Table 2.7. For the DFT calculations, all three functionals largely overestimate the SD terms for both the C and N centers, with errors of approximately 33.00 and 47.00%, respectively. For the CC calculations, the SD term for the C center calculated by CCSD appears better than that calculated by CCSD(T), where the errors are 17.78 and 26.00%, respectively. The SD term for the N center calculated by CCSD and CCSD(T) were comparable and the error with respect to the experimental data is approximately 32.00%. For the CASCI calculations, the SD terms for the C and N centers converge smoothly with respect to the active space and the core correlation does not affect the SD terms; the SD term for the C center increases with enlargement of the active space, while that for the N center decreases. Finally, the errors of the SD terms calculated by DMRG-CASSCF(13e,30o) relative to the experimental values were similar to those obtained by the CCSD calculations.

2.4.3 AlO radical

The AlO radical is best characterized as somewhere between $Al^{++}O^{--}$ with the unpaired electron in the Al s orbital, and $Al^{+}O^{-}$ with the unpaired electron in the O sp

hybrid orbital polarized away from the metal. Therefore, the spin density will be extremely sensitive to the balance in the treatment of these two configurations. This leads to the difficulties in the characterization of the HFCCs for AlO, both experimentally and theoretically. Electronic polarization in the AlO radical can easily arise in the matrix environment during experimental measurement. Knight and Weltner [116] reported the experimental FC terms for the Al center as 766, 899, and 920 MHz in Ne, Ar, and Kr matrices, respectively. Yamada *et al.* [117] later reported the experimental gas-phase value to be 738 MHz. The value for the Ne-matrix is thus closest to the gas-phase value. The experimental dielectric constants of Ne, Ar, and Kr matrices are 1.10, 1.75, and 1.85, respectively; therefore, the FC term for the Al center increases with the dielectric constant of the matrix. According to Grein's theoretical explanation [91, 92], the large values for the FC term in Ar and Kr matrices result from the dominance of the $Al^{++}O^{--}$ configuration, which enhances the spin density at the Al center. Knight *el al.* [108] first used the CI method with the Dunning's double zeta with polarizations (DZP) basis set to evaluate the FC term for Al in AlO, and the result was in reasonable agreement with the experimental values. However, in a later work, CI calculations using much larger uncontracted and contracted basis sets gave completely incorrect values [90]. These authors also determined that the MRCI-SD was not very effective to accurately characterize the HFCCs for the AlO radical. Although DFT calculations can give a qualitatively correct FC term for Al, the agreement with experiment was still far from perfect [12, 90]. Recently, the OO-MP2 and CC methods were also employed by Kossmann and Neese [103]. However, none of these methods provided results that are comparable to the experimental values, even for CCSD(T). The OO-MP2 results were too high, while the CC counterparts were too low. It is generally desirable to have the wavefunction, which provides appropriate mixing of the $Al^{+}O^{-}$ and $Al^{++}O^{--}$ configurations; therefore, the AlO radical is a multireference case [93]. It is thus interesting to assess the performance of the DMRG method for the evaluation of the **A** tensor for the AlO radical. We have used the IGLO-III [118] and EPR-III basis sets for Al and O, respectively. The total number of AOs is 84 and the results are summarized in Table 2.9. For comparison, this table also includes the experimental data of recent gas-phase [117] and Ne-matrix [116] measurements as well as the CCSD and CCSD(T) results from Kossmann and Neese [103], where the same basis sets and geometry were used.

Fermi contact term. For DFT calculations, the B3LYP functional enormously underestimates the FC term for the Al center. Although the other functionals reduce this underestimation, the error from the gas-phase value is still large at approximately 11.00%. The failure of CCSD has been confirmed with an error as large as 35.69%. The perturbative triples correction improved upon the CCSD result to some extent, but the

TABLE 2.9: HFCCs (in MHz) for the ^{2}AlO molecule. The IGLO-III and EPR-III basis sets were used for Al and O, respectively. The total number of AOs is 84. For comparison, the CCSD and CCSD(T) results from Kossmann and Neese's work were also adopted, where the same basis sets and geometry were used (see Table 2.2).

Method	^{27}Al		^{17}O	
	$A^{(K;c)}$	$A_{11}^{(K;d)}$	$A^{(K;c)}$	$A_{11}^{(K;d)}$
CASCI(9e,8o)	830.31	−47.94	9.56	36.41
CASCI(9e,16o)	765.57	−48.32	3.81	38.77
DMRG-CASCI(9e,21o)	727.98	−47.31	−0.71	42.56
DMRG-CASCI(15e,28o)	670.79	−46.37	−2.07	45.64
DMRG-CASCI(21e,31o)	682.79	−46.39	1.57	45.48
DMRG-CASCI(15e,33o)	702.80	−46.41	−3.16	45.26
DMRG-CASCI(21e,36o)	708.32	−46.49	1.61	45.13
CASSCF(9e,8o)	830.07	−47.63	−1.27	37.30
DMRG-CASSCF(15e,28o)	629.25	−53.07	−42.28	49.16
DMRG-CASSCF(21e,31o)	887.02	−54.58	−28.35	46.48
DMRG-CASSCF(15e,33o)	573.08	−54.74	−57.34	55.55
DMRG-CASSCF(21e,36o)	712.65	−54.04	−35.04	52.21
B3LYP	512.21	−59.97	8.17	66.22
TPSS	656.79	−56.10	9.52	59.91
BP86	653.71	−56.86	14.21	59.60
CCSD [a]	482.02	−57.13	18.14	63.86
CCSD [b]	482.40	−57.20	18.10	63.80
CCSD(T) [b]	565.30	−56.20	19.30	58.90
Exp − gas-phase [c]	738	−56	n/a	
Exp − Ne-matrix [d]	766	−52	2	50

[a] Present work
[b] Kossmann and Neese, Ref. [103]
[c] Ref. [117]
[d] Ref. [116]

result (error 23.40%) was still far from experimental values. The failure of CCSD(T) can be attributed to the multireference character of the AlO radical discussed earlier.

For the DMRG calculations, inclusion of the 3d polarization shells is insufficient to achieve accuracy; therefore, the Al 4d polarization in active space was also included (see Table 2.1 for details). With the CASCI calculation, the FC term for the Al center was non-monotonically dependent on the active spaces; as the size of the active space was increased, the FC term first decreased and then slowly increased. The result of the DMRG-CASCI(13e,36o) calculation (error 4.02%) is in reasonable agreement with the gas-phase value. For the CASSCF calculation, there is no improvement of the FC term

calculated by CASCI if the CAS only consists of full valence shells. The FC term for the Al center is quite sensitive with further enlargement of the active space. The FC terms are too low without core correlation; however, the FC terms are too high with core correlation but without Al $4d$ polarization. Good agreement with the gas-phase value with an error of 3.43% was obtained when all these orbitals were included in the active space.

Table 2.10 presents the SNO contributions to the total spin density at the Al center. We only compare the spin densities calculated with the four largest active spaces. The CASCI results are considered first. The SOSNO spin density slowly increases with enlargement of the CAS, while the summation of the other SNO contribution seems to remain unchanged. The increase of total spin density then follows the increase of the SOSNO spin density. Although the SOSNO spin densities from the DMRG-CASCI calculations are generally comparable to the total spin density from the gas-phase measurement (0.634 a.u. [117]), the calculated total spin densities are lowered by the negative contributions from the other SNOs, which leads to the underestimation of the DMRG-CASCI calculations. We now discuss the DMRG-CASSCF spin density. Without the core orbitals in the active space, i.e. CAS(15e,28o) and CAS(15e,33o), the total spin densities are too low relative to the gas-phase value, due to the largely negative contributions of the other SNOs. In contrast, the total spin density from the DMRG-CASSCF(21e,31o) calculation is too high relative to the gas-phase value, as a result of the high SOSNO spin density. When the core orbitals and Al $4d$ polarization shell are taken into account, i.e. CAS(21e,36o), the SOSNO spin density is close to the gas-phase value and the summation of other SNO contributions is relatively small. Consequently, the total spin density in this case is comparable to that of the gas-phase measurement.

Figure 2.2 presents the spatial distribution of the SOSNO spin density for the AlO radical. The largest CAS, i.e. CAS(21e,36o), provides an FC term for the Al center that is in excellent agreement with the gas-phase value, and the spatial distribution has peaks with medium height. In the presence of $4d$ polarization but without core correlation, i.e. CAS(15e,33o), the distribution plot has the highest peaks around the O center, while the peak at the Al center is the lowest. The features are opposite for the case of CAS(21e,31o). This figure indicates that the difference in the SOSNO spin density between CAS(15e,33o) and CAS(21e,36o) is smaller than that between CAS(21e,31o) and CAS(21e,36o), which implies that the SOSNO spin density is more significantly affected by the polarization shell than by the core correlation.
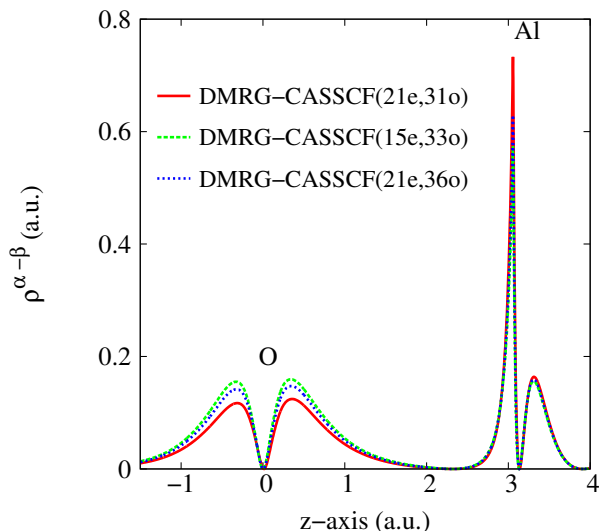
FIGURE 2.2: Spin density distribution of SOSNO for the AlO radical. The geometry of the AlO radical (in a.u.) is: O(0.000, 0.000, 0.000) and Al(0.000, 0.000, 3.057). The results were calculated using the DMRG-CASSCF(15e,33o), DMRG-CASSCF(21e,31o), and DMRG-CASSCF(21e,36o) procedures.

TABLE 2.10: SNO contributions to spin density (in a.u.) at the Al center in the AlO radical. The values in parentheses indicate the SON of SOSNO. Only the four largest active spaces are compared.

Method	Contribution of SOSNO	Sum of the other SNO contributions	Total
DMRG-CASCI(15e,28o)	0.6191 (*0.9262*)	−0.0436	0.5754
DMRG-CASCI(21e,31o)	0.6236 (*0.9264*)	−0.0385	0.5850
DMRG-CASCI(15e,33o)	0.6459 (*0.9292*)	−0.0430	0.6029
DMRG-CASCI(21e,36o)	0.6513 (*0.9306*)	−0.0436	0.6076
DMRG-CASSCF(15e,28o)	0.6491 (*0.9331*)	−0.1095	0.5396
DMRG-CASSCF(21e,31o)	0.7296 (*0.9625*)	0.0312	0.7609
DMRG-CASSCF(15e,33o)	0.5710 (*0.9376*)	−0.0794	0.4915
DMRG-CASSCF(21e,36o)	0.6259 (*0.9482*)	−0.0146	0.6113

Concerning the FC term for the O center, none of present methods except the DMRG-CASCI calculations can correctly reproduce the Ne-matrix value. However, the agreement of the DMRG-CASCI results with the Ne-matrix value can be attributed to fortuitous error cancellation. In addition, the results obtained by CC calculations are comparable to those obtained with the DMRG-CASSCF(21e,36o) calculation.

Spin-dipole term. We first discuss the SD term for the Al center. For the DFT calculations, the SD terms are very close to the gas-phase value when using the BP86 and TPSS functionals, while that with the B3LYP functional gave an overestimation with an error of 7.09%. Similarly, the SD term calculated by the CCSD method is comparable

with the gas-phase value and has an error of 2.02%. For the DMRG calculation, the SD term for the Al center is less sensitive to the active space. All DMRG-CASCI calculations largely underestimate the SD term, where the errors relative to the gas-phase and Ne-matrix values are approximately 16.00% and 10.00%, respectively. Interestingly, all DMRG-CASSCF results fall between the gas-phase and Ne-matrix values. In the case of the O center, both DFT and CC approaches largely overestimate the Ne-matrix value with the largest error up to 32.44% (for the B3LYP functional). Similarly to the Al center, the SD term for the O center is underestimated by the DMRG-CASCI calculation. Finally, the result with DMRG-CASSCF(21e,36o) is very close to the Ne-matrix value with an error of 1.46%.

2.4.4 Vinyl radical

In this subsection, we will consider the performance of DMRG method for Fermi contact prediction of vinyl radical. For the $^2A'$ ground state, the unpaired electron is located in the $8a'$ orbital which is an in-plane sp hybrid. The vinyl radical, therefore, is designated as σ radical. Briefly, the FC values of vinyl radical have been previously evaluated using several conventional methods, such as DFT [119], MR-SCI [120] , and CC [121, 122]. In the present calculations, we have used the EPR-III basis set for both C and H atoms. The total number of AOs is 113. We herein focus on the FC term of C atoms; therefore, we included a large number of orbitals of C atoms in active space, while only $1s$ orbitals of H atoms were taken into account (see Table 2.1). It is difficult to properly chose active orbitals from HF orbitals for this molecule; therefore, we employed the orbitals obtained from RASSCF/ANO-L calculation (see Sec. 2.3 for details) as the initial orbitals for DMRG calculations. Because we used different basis sets for preparing initial orbitals and DMRG calculation, we have not presented the DMRG-CASCI results. We also provided the DFT (B3LYP, TPSS, and BP86 functionals), UHF, as well as CCSD results for comparison. All results are summarized in Table 2.11.

We first discuss the FC terms of both C centers. It is obvious that the UHF method largely overestimates these FC terms. For three DFT calculations, while their results for C1 center are in reasonable agreement with experimental value, they significantly underestimate the FC term of C2 center with smallest and largest error of up to 27.01% (for TPSS functional) and 61.08% (for BP86 functional), respectively. The similar situation was observed for the CCSD calculation. The errors of CCSD results from experimental values are 4.84% and 29.88% for C1 and C2 centers, respectively. The DMRG-CASSCF(15e,33o) calculation provided the FC terms of both C centers in good agreement with experimental values. The errors are 3.21% and 12.49 % for C1 and C2 centers, respectively.

TABLE 2.11: Fermi contact values (in MHz) of $^2A'$ state of C_2H_3 radical using EPR-III basis set, where the total number of AOs is 113.

Method	C1	C2	H1	H2	H3
DMRG-CASSCF(15e,33o)	311.21	−27.11	21.14	158.03	101.59
UHF	479.40	−116.56	−37.44	193.94	138.91
B3LYP	324.59	−12.05	55.29	173.55	112.14
TPSS	314.72	−17.59	60.97	181.30	109.47
BP86	293.77	−9.38	49.06	173.69	112.57
CCSD	316.12	−16.90	39.00	157.13	96.83
Exp.[a]	301.54	−24.10	38.67	184.80	110.97

[a] Taken from Ref. [121]

We now discuss the FC terms of three H centers. Although all absolute values of HF results are reasonable, the sign of FC term of H1 center is different from that of experimental values. All the DFT calculations provide the FC terms of H2 and H3 centers in good agreement with experimental values, however, they overestimate the FC term of H1 center. In contrast to DFT, the CCSD method gives an accurate FC term for H1 center, while the FC terms for H2 and H3 centers of this method are far away from experimental values. The DMRG-CASSCF(15e,33o) calculation underestimates the FC terms of all H centers. The large discrepancy between DMRG results and experimental values seems to arise because we only included the H $1s$ orbital in active space. In order to get more accurate FC terms for H centers, we should include more orbitals of H atom in active space.

2.4.5   Accuracy of DMRG method for HFCC prediction

The quality of a DMRG wavefunction is dependent on the number of renormalized basis states M, and variationally converges to an exact description with increasing M. A more accurate DMRG wavefunction requires a larger M, which implies greater computational cost. Therefore, it is useful to reveal the convergence of HFCCs calculated by the DMRG method with respect to M.

Table 2.12 presents the differences in DMRG energy as well as total discarded weight between the last two DMRG sweeps in DMRG-CASSCF calculations with the largest active spaces for each system studied in this work. The total discarded weights of the last DMRG sweep is also provided. From this Table, we can see that the change in DMRG energy measured in the last two sweeps is negligible.

TABLE 2.12: The different in DMRG energy as well as total discarded weight between last two DMRG sweeps for DMRG-CASSCF calculations with largest active spaces for each system studied in this work. The total discarded weight of last DMRG sweep is also included.

Molecules	DMRG-CASSCF calculations	Deviation of energies (mE_h)	Deviation of total discarded weight	Total discarded weight
BO	DMRG-CASSCF(13e,30o)	0.00143	6.96157×10^{-6}	3.69354×10^{-6}
CO^+	DMRG-CASSCF(13e,30o)	0.00066	7.77564×10^{-6}	4.65225×10^{-6}
CN	DMRG-CASSCF(13e,30o)	0.00132	1.36235×10^{-5}	8.14189×10^{-6}
AlO	DMRG-CASSCF(21e,36o)	0.00249	4.73789×10^{-5}	1.60101×10^{-5}
C_2H_3	DMRG-CASSCF(15e,33o)	0.00105	3.66949×10^{-5}	3.36053×10^{-5}

Let us illustrate the convergence of DMRG results with increasing calculation level. We have chosen the CN radical as an example for this purpose. DMRG calculations with $M = 128$, 256, and 1024 for CAS(13e,30o) were performed. The MOs from the DMRG-CASSCF(13e,30o) calculation with $M = 512$ was used as the orbital basis for the other calculations. To maintain consistence between the different DMRG calculations, the CASCI procedure was conducted with the same orbital basis. Table 2.13 presents the convergence of the total electronic energy, FC term, and SD term for the C center with respect to M. The energy with $M = 512$ is converged to 0.604 mE_H when compared to that of $M = 1024$. The FC term significantly decreases when going from $M = 128$ to 256 (approximately 13.00 MHz) and seems to be convergent with larger values of M. This situation also happens to the SD term.

TABLE 2.13: The total discarded weight, total energy, and HFCCs at the C center at different number of renormalized states M for CN radical. Only the first element is presented for the SD term. The active space is CAS(13e,30o). The convergent MOs of the DMRG-CASSCF(13e,30o) calculation with $M = 512$ were used as a reference for the other DMRG calculations and only the CASCI procedure was performed for these calculations.

M	Total discarded weight	Energy (E_h)	FC term $A^{(K;c)}$ (MHz)	SD term $A_{11}^{(K;d)}$ (MHz)
128	1.16877×10^{-4}	$-92.570\ 835$	576.80	-53.18
256	2.78911×10^{-5}	$-92.575\ 539$	563.79	-52.97
512	8.14189×10^{-5}	$-92.577\ 510$	561.95	-52.92
1024	1.35497×10^{-6}	$-92.578\ 114$	559.44	-52.86
∞		$-92.578\ 276$	558.99^a	-52.85^a

^{a} Linear extrapolation from two points at $M = 512$ and 1024 of HFCCs *vs* the total discarded weight (see Figure 2.3)

In Figure 2.3, we plotted the total energy, FC term, and SD term *vs* the discarded weights at different values of M. We excluded the data with $M = 128$ for extrapolation.

It is known that the least-square fitting represents a near direct proportionality between the total energy and total discarded weight [64, 70] as shown in upper panel of Figure 2.3. The extrapolation estimates the DMRG energy at $M = \infty$ to be $-92.578\,276\,E_h$; therefore, the DMRG energy at $M = 512$ (see Table 2.13) is found to be accurate to $0.766\,mE_h$. The HFCCs *vs* total discarded weight, however, are non-linear as shown in the middle (FC term) and lower (SD term) panels of Figure 2.3. Although the number of points from available data is not sufficient to generally extrapolate the FC and SD terms at $M = \infty$, we have attempted to linearly extrapolate from last two points (at $M = 512$ and 1024). We then obtained the approximate estimations of the FC and SD terms at $M = \infty$ to be 558.99 MHz and -52.85 MHz, respectively. Errors of FC and SD terms at $M = 512$ (see Table 2.13) from these approximate estimations are 0.53% and 0.13%, respectively.

Generally, due to the non-linearity of HFCCs *vs* total discarded weight, it is not feasible to provide the general trend for convergence of HFCCs with respect to M. However, from above approximate estimation of HFCCs at $M = \infty$ we found that the results at $M = 512$ are reliable.

2.5   Conclusion and outlook

In summary, DMRG calculations were performed to predict the HFCCs of 4 $^2\Sigma$ diatomic radicals (BO, CO^+, CN, and AlO) and vinyl (C_2H_3) radical. The HFCCs of the less electronegative centers (B, C, and Al) obtained were in excellent agreement with the experimental values. The present work not only provides some insight into the accuracy of HFCC predictions using the DMRG method, but also serves as the benchmark for further work. It should be emphasized that the DMRG algorithm used herein was considered as a near-FCI method and the electron correlation effects were systematically investigated using the CAS-type procedures, i.e. CASCI and CASSCF. At this point, we are able to answer the two questions addressed in the introduction. (i) Our assessment shows that the active space method has the potential to accurately describe the HFCCs, but the active space must be addressed by the construction of active orbitals. Generally, the FC term is particularly sensitive to the choice of active space. Moreover, the DMRG method is also suitable to deal with multireference cases such as the AlO radical. (ii) It is necessary to correlate the core electrons to correctly obtain the spin density at the nucleus; therefore, the core orbitals should be included in CAS. At the same time, the inclusion of polarization shells is necessary to describe the dynamical correlation, which provides the appropriate spin-polarized effects.
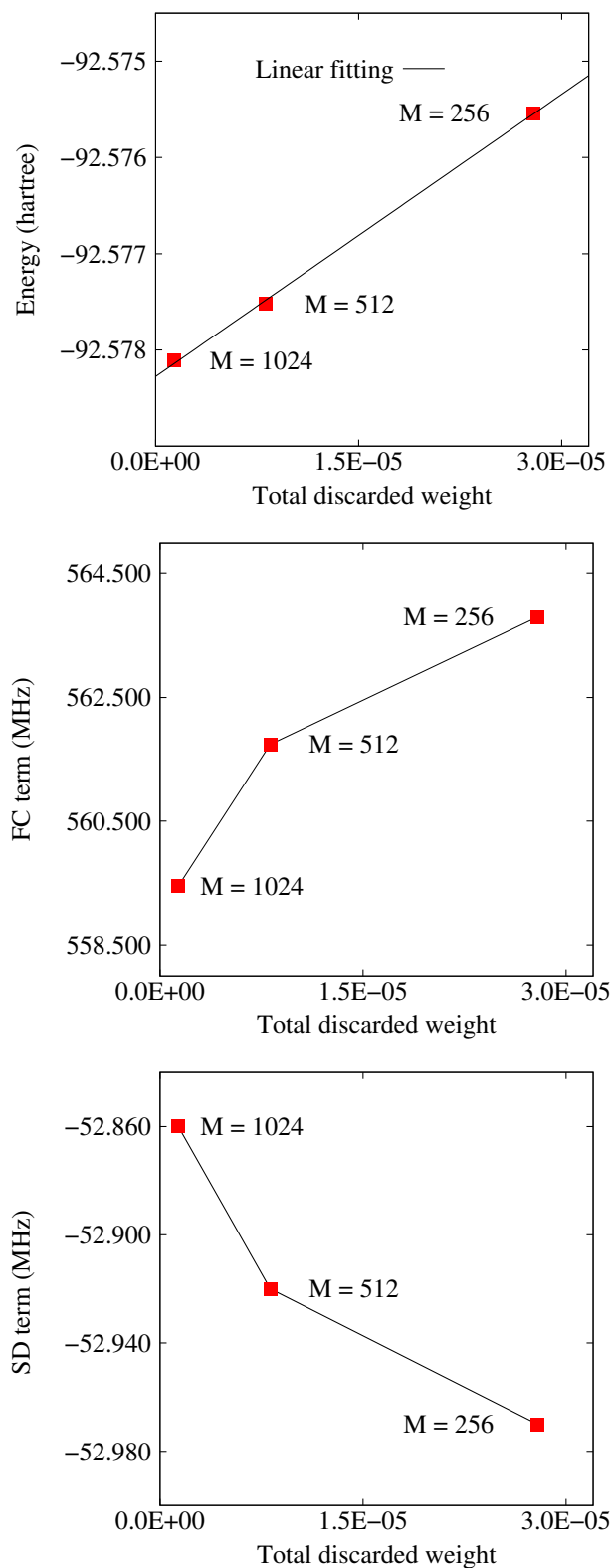
FIGURE 2.3: Total energy (upper panel), FC term (middle panel), and SD term (lower panel) *vs* the total discarded weight for DMRG calculations of CN radical at $M = 256$, 512, and 1024.

Most CASCI calculations provided FC terms that were in poor agreement with the experimental values, while reasonably accurate results were obtained when the orbital optimization procedure was employed with the same CAS. This situation can be attributed to the nature of the one-particle basis in which the DMRG calculations were performed. The canonical HF orbitals were used as the orbital basis for the DMRG-CASCI calculation, whereas the DMRG calculation in conjunction with the CASSCF procedure was conducted with much more compact orbitals that were obtained through the orbital optimization procedure. The SD term is generally less sensitive to the level of theory, as well as the size of the active space, than the FC term. The SD terms calculated using the DMRG-CASSCF approach with the largest active spaces were better to some extent than those calculated using conventional methods in most cases.

The assessment for the convergence of HFCCs with respect to the number of renormalized states M was also performed. We found that the HFCCs *vs* total discarded weight did not yield a linear relation, while energies were in direct proportional to total discarded weights. Although Boguslawski *et al.* [83] has recently claimed that reliable reference spin densities can be obtained even if the total energies are not converged with respect to M, the conclusion for HFCCs, which are calculated from spin density, is questionable. This is because the nature of HFCCs is different from that of total spin density, especially the FC term, which is the direct numerical measure of spin density at the position of nucleus. Despite this fact, we have attempted to estimate the HFCCs at $M = \infty$ by linear extrapolation from two points at $M = 512$ and 1024. Errors of HFCCs at $M = 512$ from these approximate estimations are negligible for our test cases.

Finally, we have explored the reliability of the DMRG method for the HFCC prediction of diatomic radicals. For molecules with more complicated structure, the active space must be sufficiently large to capture the electron correlation effect, which implies expensive computation. Therefore, the combination of the DMRG method with another multireference dynamical correlation model is useful to obtain accurate HFCCs. To accurately predict the HFCCs of species that contain heavy elements requires consideration of the relativistic effects, including the scalar and spin-orbit coupling effects.

Chapter 3

Scalar relativistic DMRG calculations of HFCCs for heavy molecules: case studies of $4d$ transition metals

T. N. Lan, Y. Kurashige, T. Yanai,

"Scalar reltativistic calculations of hyperfine coupling constants using ab initio density matrix renormalization group in combination with third-order Douglas-Kroll-Hess transformation: case studies of 4d transition metals",

In preparation

3.1   Introduction

As mentioned in Chapter 1, both electron correlations and relativistic effects are important for the accurate prediction of HFCCs for heavy molecules. In framework of modern quantum chemical calculation of HFCCs, while the relativistic DFT methods have been widely used [17–24, 27], there have been only a few studies employing the relativistic *ab initio* wavefunction methods [16, 25, 26, 28]. Generally, from the theoretical point of view, it is highly desirable to provide a computational scheme including both high-level correlations and relativistic effects for HFCC prediction.

The 4c-DMRG has been very recently developed by Knecht, Legeza, and Reiher [123]; however, it is still far from practical applications, especially for the isotropic HFCC that requires the core correlation. Therefore, the 2c approaches are still useful to provide a

good balance between computational cost and accuracy for isotropic HFCC calculations. As a continuation of the previous work given in Chapter 2, we have evaluated the HFCCs of molecules containing heavy elements using the DMRG-CASSCF in combination with the quasi-relativistic DKH transformation.

The quasi-relativistic DKH transformation can decouple the large and small components of the Dirac spinors in the presence of an external potential by repeating unitary transformations. The main advantage of DKH transformation is that the DKH Hamiltonian is variationally stable. In addition, the DKH transformation can be easily incorporated into any electron correlation methods. Recently, a numerous methods for higher-order unitary transformations have been developed, such as the exponential-type transformation [124], the generalized transformation [125], the infinite-order transformation [126], and the arbitrary-order transformation [127–129]. The DKH method therefore becomes one of the most successful tools in relativistic quantum chemistry. Along with the success of the DKH transformation for energy-related calculations, this method has been also widely applied to calculate molecular properties, such as magnetic shielding constants [130–132], nuclear magnetic resonance spin-spin coupling constants [133], Mössbauer electron density [134, 135], electric field gradients [136, 137], magnetizabilities [138], and HFCCs [23–25]. These studies have shown that the so-called "picture change" error (PCE) has a pronounced effect on molecular properties even for light molecules. While the higher-order DKH transformations have been applied to investigate the PCE correction for electric field gradient, Mössbauer electron density, and magnetic shielding constants; the DKH treatment for HFCCs was used only up to the second order. Moreover, Seino *et al.* [139] has shown that the higher than second-order corrections are necessary to calculate the expectation value of $\delta(r - R)$ operator with reliable accuracy. A similar statement was also recently made by Malkin *et al.* [17]. Thus, going beyond the second order is necessary to get the calculated HFCCs close to those of 4c calculation and experiment. In present work, we have employed the DKH transformation up to the third order (DKH3) for hyperfine coupling (hfc) operator.

The object of this study entails two new technical points: (i) the initial derivation and implementation of the DKH3 transformation for hfc operator, (ii) the assessment on the performance of the DMRG in combination with the DKH transformation for isotropic HFCC calculations.

For test cases, we have applied our DMRG-CASSCF/DKH3 method to characterize the HFCCs of doublet radicals containing fifth-row elements: Ag, PdH, and RhH_2. Because the spin density around the vicinity of Ag nuclei is dominated by the outermost $5s$ orbital, the evaluation of isotropic HFCC of Ag atom does not require a lot of effort. Recently, several works using *ab initio* calculations, such as QCISD/IORAmm,

MP2/IORAmm [26], and MCDF [16] accurately predicted the isotropic HFCC of Ag. Therefore, in order to validate our derivation and implementation, we have first evaluated the isotropic HFCC of Ag atom at different levels of DKH transformation and active space. Previous studies showed that PdH and RhH_2 are quite important in catalyses; therefore, understanding their electronic and magnetic properties is appealing and necessary. In these radicals, the unpaired electron is located in the σ orbitals containing predominant $4d_\sigma$ and $5s$ metal character and small amount of H $1s$. The reliable accuracy in characterization of isotropic HFCC for these metal centers is thus expected to require the high-order correlation and core-level spin-polarization effects. Although the calculations of EPR $g-$tensors have been carried out by many works using both DFT and *ab initio* methods, the calculated HFCCs for PdH radical were only published by Belanzoni and coworkers [19] using DFT/ZORA and by Quiney and Belanzoni [15] using DHF. The isotropic HFCC of Pd center was largely underestimated by DHF. More reasonable result can be provided by DFT/ZORA; however, the error from experimental value is still large. Quiney and Belanzoni have attributed the failure of DHF to the strong configuration mixing of the Pd orbitals, which is incapable to describe by single-configuration model like HF [15]. Thus, it is interesting to assess our DMRG-CASSCF/DKH3 scheme to characterize the isotropic HFCC of Pd center in PdH radical. To our best knowledge, the calculation of EPR parameters for RhH_2 radical has not been reported yet. Moreover, the experimental value is still controversial. Zee, Hamrick, and Weltner [140] have first measured the EPR parameters of RhH_2. In their experiment, the Rh atom was vaporized by laser radiation, and then the vapor was deposited with argon matrix containing hydrogen. Recently, Hayton and colleagues [141] have measured again the EPR parameters of RhH_2 by depositing Rh atoms from thermal sources into hydrocarbon matrices. Although their results were close to those in the work of Zee *et al.*, they suggested that the observed spectrum is assigned to Rh atoms instead of RhH_2 complexes. They also suggested that EPR parameters measured by Zee *et al.* may not result from the reactions of ground state atoms but from those of thermally or/and electronically excited Rh atoms formed in the laser plume. Therefore, it is quite valuable to have the calculated results using high-level theory in order to verify the experimental value.

The chapter is organized as follows. The background of theory used in this study is presented in Sec. 3.2 followed by the computational details in Sec. 3.3. Results and discussion are given in Sec. 3.4. Conclusions are drawn in Sec. 3.5.

3.2   Theoretical background

3.2.1   Direct DKH transformation for general property operator

We first introduce the direct scheme of DKH transformation for general property operator proposed by Wolf and Reiher [142]. The general electromagnetic 4c operator X can be written as follows

$$X^{(4)} = X_e^{(4)} + X_o^{(4)}. \tag{3.1}$$

The operators with the superscript (4) are in the 4c picture. The operator $X_e^{(4)}$ is even, i.e., block-diagonal operator, while the operator $X_e^{(4)}$ is odd, i.e., off-diagonal operator. In general, the operators $X_e^{(4)}$ and $X_o^{(4)}$ are the electric and magnetic property operators, respectively. In the direct scheme, the unitary transformation U only depends on an external potential V but not on property operator X, i.e., $U = U(V)$. The DKH property operator is then obtained by directly applying the unitary transformation U to the property operator $X^{(4)}$,

$$X_{\text{DKH}\infty}^{(4)} = U X^{(4)} U^+ = \cdots U_2 U_1 U_0 X^{(4)} U_0^+ U_1^+ U_2^+ \cdots , \tag{3.2}$$

with the free-particle Foldy-Wouthuysen (fpFW) transformation defined as

$$U_0 = \begin{pmatrix} A_p & A_p R_p \\ -A_p R_p & A_p \end{pmatrix}, \tag{3.3}$$

and operators A_p and R_p given by

$$A_p = \sqrt{\frac{E_p + mc^2}{2E_p}}, \tag{3.4}$$

$$R_p = \frac{c\boldsymbol{\sigma}\mathbf{p}}{E_p + mc^2} = K_p \boldsymbol{\sigma}\mathbf{p}, \tag{3.5}$$

$$E_p = c\sqrt{p^2 + m^2c^2}, \tag{3.6}$$

where $\boldsymbol{\sigma}$ denotes a 3-vector, whose elements consist of the standard (2×2) Pauli matrices. Wolf and Reiher [142] have argued that if the DKH property operator up to nth order in V is sought for, one has to apply all unitary transformations up to U_n. In other words, the DKH transformation of property operator follows the n rule instead of familiar $(2n + 1)$ rule. However, to be consistent with previous works [23–25], the DKH order for property operator has been defined to be the same as that for Hamiltonian in the present work. This definition has been recently used by Seino *et al.* [132, 139]. The

DKH operator $X^{(4)}$ up to the third order (DKH3) then reads

$$X^{(4)}_{\text{DKH3}} = U_2 U_1 U_0 X^{(4)} U_0 U_1 U_2. \tag{3.7}$$

In the present work, we employed the exponential parameterization of the unitary transformation $U_n = \exp(W_n)$, which was proposed by Nakajima and Hirao [124], for U_1 and U_2. After doing mathematics, the diagonal blocks of DKH property operators, which are exactly the same as those obtained by Wolf and Reiher [142], read

$$X^{(4)}_{e,1} = A_p \left(X^{(4)}_e + R_p X^{(4)}_e R_p \right) A_p + \boldsymbol{\beta} A_p \left\{ R_p, X^{(4)}_o \right\} A_p, \tag{3.8}$$

$$X^{(4)}_{e,2} = X^{(4)}_{e,1} + \left[W_1, X^{(4)}_{o,1} \right], \tag{3.9}$$

$$X^{(4)}_{e,3} = X^{(4)}_{e,2} + \frac{1}{2} \left[W_1, \left[W_1, X^{(4)}_{e,1} \right] \right] + \left[W_2, X^{(4)}_{o,1} \right], \tag{3.10}$$

with the first-order off-diagonal block

$$X^{(4)}_{o,1} = \boldsymbol{\beta} A_p \left[R_p, X^{(4)}_e \right] A_p + A_p \left(X^{(4)}_o - R_p X^{(4)}_o R_p \right) A_p. \tag{3.11}$$

The odd operators W_1 and W_2 are familiar perturbation-independent operators parameterizing the standard unitary transformation U_1 and U_2, respectively:

$$W_1(p, p') = \boldsymbol{\beta} \frac{O_1(p, p')}{E_{p'} + E_p}, \tag{3.12}$$

$$W_2(p, p') = \boldsymbol{\beta} \frac{[W_1(p, p'), E_1(p, p')]}{E_{p'} + E_p}. \tag{3.13}$$

Operators E_1 and O_1 are given by

$$E_1 = A_p V A_p + A_p R_p V R_p A_p, \tag{3.14}$$

$$O_1 = A_p R_p V A_p + A_p V R_p A_p. \tag{3.15}$$

3.2.2 Direct DKH transformation for magnetic operator

The 4c magnetic operator describing the interaction between the electron spin and external magnetic field is given by

$$X = \begin{pmatrix} 0 & \boldsymbol{\sigma} \mathbf{A} \\ \boldsymbol{\sigma} \mathbf{A} & 0 \end{pmatrix}, \tag{3.16}$$

where $\mathbf{A}$ is vector potential of the external magnetic field. We subtitute 4c operator 3.16 into Eqs. 3.8−3.10. Because magnetic operator 3.16 is odd, only terms related to $X^{(4)}_o$ are nonzero. After doing mathematics, we finally obtain the upper diagonal block

of DKH3 magnetic operator as follows

$$X_{e,1}^{(2)} = \ H_{\mathrm{mag}} + H_{\mathrm{mag}}^+, \tag{3.17}$$

$$
\begin{aligned}
X_{e,2}^{(2)} =\ & X_{e,1} - \left(A\tilde{V}A\right) H_{\mathrm{mag}} + \left(AR\tilde{V}RA\right) R_p^{-2} H_{\mathrm{mag}} \\
& - \left(AR\tilde{V}RA\right) H_{\mathrm{mag}}^+ + \left(A\tilde{V}A\right) R_p^2 H_{\mathrm{mag}}^+ \\
& - H_{\mathrm{mag}}^+ \left(A\tilde{V}A\right) + H_{\mathrm{mag}}^+ R_p^{-2} \left(AR\tilde{V}RA\right) \\
& - H_{\mathrm{mag}} \left(AR\tilde{V}RA\right) + H_{\mathrm{mag}} R_p^2 \left(A\tilde{V}A\right),
\end{aligned} \tag{3.18}
$$

$$
\begin{aligned}
X_{e,3}^{(2)} =\ & X_{e,2} + \left(AR\tilde{V}RA\right) H_{\mathrm{mag}}^+ \left(A\tilde{V}A\right) + \left(A\tilde{V}A\right) H_{\mathrm{mag}} \left(AR\tilde{V}RA\right) \\
& + \left(A\tilde{V}A\right) R_p^2 H_{\mathrm{mag}}^+ R_p^{-2} \left(AR\tilde{V}RA\right) + \left(AR\tilde{V}RA\right) R_p^{-2} H_{\mathrm{mag}} R_p^2 \left(A\tilde{V}A\right) \\
& - \left(A\tilde{V}A\right) R_p^2 H_{\mathrm{mag}}^+ \left(A\tilde{V}A\right) - \left(A\tilde{V}A\right) H_{\mathrm{mag}} R_p^2 \left(A\tilde{V}A\right) \\
& - \left(AR\tilde{V}RA\right) H_{\mathrm{mag}}^+ R_p^{-2} \left(AR\tilde{V}RA\right) - \left(AR\tilde{V}RA\right) R_p^{-2} H_{\mathrm{mag}} \left(AR\tilde{V}RA\right) \\
& + \left(AR\tilde{V}RA\right) R_p^{-2} \left(AR\tilde{V}RA\right) R_p^{-2} H_{\mathrm{mag}} - \left(AR\tilde{V}RA\right) R_p^{-2} \left(AR\tilde{V}RA\right) H_{\mathrm{mag}}^+ \\
& + \left(AR\tilde{V}RA\right) \left(A\tilde{V}A\right) H_{\mathrm{mag}} - \left(AR\tilde{V}RA\right) \left(A\tilde{V}A\right) R_p^2 H_{\mathrm{mag}}^+ \\
& - \left(A\tilde{V}A\right) \left(AR\tilde{V}RA\right) R_p^{-2} H_{\mathrm{mag}} + \left(A\tilde{V}A\right) \left(AR\tilde{V}RA\right) H_{\mathrm{mag}}^+ \\
& + \left(A\tilde{V}A\right) R_p^2 \left(A\tilde{V}A\right) H_{\mathrm{mag}} + \left(A\tilde{V}A\right) R_p^2 \left(A\tilde{V}A\right) R_p^2 H_{\mathrm{mag}}^+ \\
& - H_{\mathrm{mag}}^+ R_p^{-2} \left(AR\tilde{V}RA\right) \left(A\tilde{V}A\right) + H_{\mathrm{mag}}^+ R_p^{-2} \left(AR\tilde{V}RA\right) R_p^{-2} \left(AR\tilde{V}RA\right) \\
& - H_{\mathrm{mag}}^+ \left(A\tilde{V}A\right) R_p^2 \left(A\tilde{V}A\right) + H_{\mathrm{mag}}^+ \left(A\tilde{V}A\right) \left(AR\tilde{V}RA\right) \\
& + H_{\mathrm{mag}} \left(AR\tilde{V}RA\right) \left(A\tilde{V}A\right) - H_{\mathrm{mag}} \left(AR\tilde{V}RA\right) R_p^{-2} \left(AR\tilde{V}RA\right) \\
& + H_{\mathrm{mag}} R_p^2 \left(A\tilde{V}A\right) R_p^2 \left(A\tilde{V}A\right) - H_{\mathrm{mag}} R_p^2 \left(A\tilde{V}A\right) \left(AR\tilde{V}RA\right) \\
& - \left(A\tilde{V}A\right) \left(AR\tilde{V}RA\right) R_p^{-2} H_{\mathrm{mag}} + \left(A\tilde{V}A\right) \left(AR\tilde{V}RA\right) H_{\mathrm{mag}}^+ \\
& + \left(A\tilde{V}A\right) \left(A\tilde{V}A\right) H_{\mathrm{mag}} - \left(A\tilde{V}A\right) \left(A\tilde{V}A\right) R_p^2 H_{\mathrm{mag}}^+ \\
& - \left(AR\tilde{V}RA\right) \left(AR\tilde{V}RA\right) R_p^{-2} H_{\mathrm{mag}} + \left(AR\tilde{V}RA\right) \left(AR\tilde{V}RA\right) H_{\mathrm{mag}}^+ \\
& + \left(AR\tilde{V}RA\right) \left(A\tilde{V}A\right) H_{\mathrm{mag}} - \left(AR\tilde{V}RA\right) \left(A\tilde{V}A\right) R_p^2 H_{\mathrm{mag}}^+ \\
& + H_{\mathrm{mag}}^+ \left(A\tilde{V}A\right) \left(A\tilde{V}A\right) + H_{\mathrm{mag}}^+ \left(A\tilde{V}A\right) \left(AR\tilde{V}RA\right) \\
& - H_{\mathrm{mag}}^+ R_p^{-2} \left(AR\tilde{V}RA\right) \left(A\tilde{V}A\right) - H_{\mathrm{mag}}^+ R_p^{-2} \left(AR\tilde{V}RA\right) \left(AR\tilde{V}RA\right) \\
& - H_{\mathrm{mag}} R_p^2 \left(A\tilde{V}A\right) \left(A\tilde{V}A\right) - H_{\mathrm{mag}} R_p^2 \left(A\tilde{V}A\right) \left(AR\tilde{V}RA\right) \\
& + H_{\mathrm{mag}} \left(AR\tilde{V}RA\right) \left(A\tilde{V}A\right) + H_{\mathrm{mag}} \left(AR\tilde{V}RA\right) \left(AR\tilde{V}RA\right),
\end{aligned} \tag{3.19}
$$

where

$$A\tilde{V}A = A_p \frac{V(p,p')}{E_p + E_{p'}} A_p, \tag{3.20}$$

$$AR\tilde{V}RA = A_p R_p \frac{V(p,p')}{E_p + E_{p'}} R_p A_p, \tag{3.21}$$

and

$$H_{\text{mag}} = A_p K_p \left(\boldsymbol{\sigma}\mathbf{p}\right) \left(\boldsymbol{\sigma}\mathbf{A}\right) A_p, \tag{3.22}$$

$$H_{\text{mag}}^+ = A_p \left(\boldsymbol{\sigma}\mathbf{A}\right) \left(\boldsymbol{\sigma}\mathbf{p}\right) K_p A_p. \tag{3.23}$$

The superscript (2) in Eqs. 3.17−3.19 means that the DKH operators are in 2c picture.

Using the relation

$$\left(\boldsymbol{\sigma}\mathbf{a}\right) \left(\boldsymbol{\sigma}\mathbf{b}\right) = \mathbf{a} \cdot \mathbf{b} + i\boldsymbol{\sigma} \cdot \left(\mathbf{a} \times \mathbf{b}\right), \tag{3.24}$$

we have

$$\left(\boldsymbol{\sigma}\mathbf{p}\right) \left(\boldsymbol{\sigma}\mathbf{A}\right) = \mathbf{p} \cdot \mathbf{A} + i\boldsymbol{\sigma} \cdot \left(\mathbf{p} \times \mathbf{A}\right)$$

$$= [\mathbf{p} \cdot \mathbf{A}] + \mathbf{A} \cdot \mathbf{p} + i\boldsymbol{\sigma} \cdot [\mathbf{p} \times \mathbf{A}] - i\boldsymbol{\sigma} \cdot \left(\mathbf{A} \times \mathbf{p}\right), \tag{3.25}$$

$$\left(\boldsymbol{\sigma}\mathbf{A}\right) \left(\boldsymbol{\sigma}\mathbf{p}\right) = \mathbf{A} \cdot \mathbf{p} + i\boldsymbol{\sigma} \cdot \left(\mathbf{A} \times \mathbf{p}\right). \tag{3.26}$$

Herein, square brackets mean that the operator $\mathbf{p}$ only acts on the vector potential $\mathbf{A}$, but not on the wavefunction. It is easy to show that the first term in Eq. 3.25 vanishes. In fact, this term will vanish if we invoke the Coulomb gauge $\nabla \cdot \mathbf{A} = 0$ [86]. From Eqs. 3.25 and 3.26, it is easy to decompose the magnetic operator into various contributions. The terms being linear in σ represent the spin contribution, while the other terms represent the orbital contribution.

Substituting Eqs. 3.22 and 3.23 into Eqs. 3.17-3.19 and using the relations 3.25 and 3.26, we obtain the DKH transformation for magnetic operator. For example, the first order of DKH magnetic operator reads

$$\begin{aligned} X_{e,1}^{(2)} =& A_p K_p i\boldsymbol{\sigma} \left[\mathbf{p} \times \mathbf{A}\right] A_p - A_p i\boldsymbol{\sigma} \left\{K_p \left(\mathbf{A} \times \mathbf{p}\right) - \left(\mathbf{A} \times \mathbf{p}\right) K_p\right\} A_p \\ &+ A_p \left\{K_p \mathbf{A} \cdot \mathbf{p} + \mathbf{A} \cdot \mathbf{p} K_p\right\} A_p. \end{aligned} \tag{3.27}$$

Neyman *et al.* [30] neglected the second term in Eq. 3.27 in their implementation. Thereafter, Malkin *et al.* [31] confirmed that the contribution of this term is completely negligible. In the NR limit ($c \to \infty$), the kinetic factors $A_p \to 1$ and $K_p \to (2c)^{-1}$. The NR operator can be then obtained.

It is worth mentioning that although the expression of third order is relatively long, its computational cost is comparable to that of second order.

3.2.3   Hyperfine coupling operator

In the case of hfc operator, the vector potential created by nucleus N is given as follows

$$\mathbf{A}_N = \boldsymbol{\mu}_N \times \nabla G_N, \tag{3.28}$$

where $\boldsymbol{\mu}_N$ is the magnetic moment of nucleus N and

$$G_N = \int \frac{\chi_N (\mathbf{R} - \mathbf{R}_N)}{\mathbf{r} - \mathbf{R}_N} d\mathbf{R}. \tag{3.29}$$

Here $\mathbf{r}$ and $\mathbf{R}$ are the electronic and nuclear distributions, respectively, and χ_N is the funtion related to nuclear magnetization distribution, which is usually assumed to be the same as the nuclear charge distribution in quantum chemical calculations [25, 143]. Herein, we use the Gaussian nucleus model

$$\chi(\mathbf{R} - \mathbf{R}_N) = (\eta_N/\pi)^{3/2} \exp\left(-\eta_N (\mathbf{R} - \mathbf{R}_N)^2\right). \tag{3.30}$$

The nuclear exponent η_N is taken from database reported by Visscher and Dyall [144].

The additional integral $[\mathbf{A} \times \mathbf{p}]$ was implemented. However, we numerically found that the total contribution of the terms related to this integral is negligible not only at the first order, but also at higher orders. Thus, we will not discuss it hereafter. In the present work, we only consider the SR effects, so that the orbital contribution, which is related to the inner product $[\mathbf{A} \cdot \mathbf{p}]$, is also neglected.

Using vector potential 3.28, the third term of Eq. 3.25 reads [86]

$$h_{\mathrm{hfc}}^{(\sigma)} = i\boldsymbol{\sigma} \left[\mathbf{p} \times \mathbf{A}_N\right] = h_{\mathrm{iso}} + h_{\mathrm{ani}}, \tag{3.31}$$

where the first and second terms in Eq. 3.31 are the isotropic (iso) and anisotropic (ani) contributions, respectively:

$$h_{\mathrm{iso}} = \frac{2}{3} (i\boldsymbol{\sigma} \cdot \boldsymbol{\mu}_N)(\mathbf{p} \cdot \nabla G_N), \tag{3.32}$$

$$h_{\mathrm{ani}} = -\left[(\boldsymbol{\mu}_N \cdot \mathbf{p})(i\boldsymbol{\sigma} \cdot \nabla G_N) - \frac{1}{3}(i\boldsymbol{\sigma} \cdot \boldsymbol{\mu}_N)(\mathbf{p} \cdot \nabla G_N)\right]. \tag{3.33}$$

The HFCCs are then determined by the second derivative of the expectation value of hfc operators with respect to the electron spin and nuclear spin. For instance, the isotropic HFCC for nucleus N is given by

$$A_{\mathrm{iso}}(N) = \langle \psi | \frac{\partial^2 X_{\mathrm{DKH}n}^{\mathrm{iso}}}{\partial s \partial \mu_N} | \psi \rangle , \tag{3.34}$$

where $X_{\mathrm{DKH}n}^{\mathrm{iso}}$ is the DKHn isotropic operator.

3.3 Computational details

The DMRG code developed by our group [70] was employed to obtain the active-space wavefunction. The active spaces used in this work are presented in Table 3.1. The number of spin adapted renormalized states M was set to 512 in all DMRG calculations, unless otherwise noted. We have implemented the spin adaptation of Zgid and Nooijen [67] in our DMRG code; therefore, the number of actual bases that are not spin adapted is much larger than M (approximately twice). In the present work, the primitive ANO basis sets [95, 96] were used for all elements and have the following numbers of exponents: $21s18p13d6f$ for metal (Ag, Pd, and Rh), and $8s4p3d$ for H.

TABLE 3.1: Active orbitals.

Molecule	Active space	Active orbitals	
Ag	CAS(19e,18o)	$4s4p4d$ $5s5p5d$	
	CAS(37e,32o)	$3s3p3d$ $4s4p4d$ $5s5p5d$ $6d$	
	CAS(37e,39o)	$3s3p3d$ $4s4p4d$ $5s5p5d$ $6d$ $4f$	
PdH	CAS(21e,20o)	Pd: $3s$ $4s4p4d$ $5s5p5d$	H: $1s$
	CAS(21e,32o)	Pd: $3s$ $4s4p4d$ $5s5p5d$ $6d$ $4f$	H: $1s$
	CAS(37e,40o)	Pd: $3s3p3d$ $4s4p4d$ $5s5p5d$ $6d$ $4f$	H: $1s$
RhH$_2$	CAS(21e,21o)	Rh: $3s$ $4s4p4d$ $5s5p5d$	H: $1s$
	CAS(21e,33o)	Rh: $3s$ $4s4p4d$ $5s5p5d$ $6d$ $4f$	H: $1s$
	CAS(37e,41o)	Rh: $3s3p3d$ $4s4p4d$ $5s5p5d$ $6d$ $4f$	H: $1s$

The molecular geometry of PdH was taken from experiment, $r_e(\mathrm{Pd-H}) = 1.529$Å [19]. Because there is no available experimental geometry for the RhH$_2$ radical, we have adapted it from the MRCI-SD calculation reported by Balasubramanian and Liao [145]: $r_e(\mathrm{Rh-H}) = 1.510$Å and $\theta_e(\mathrm{H-Rh-H}) = 84°$ for the ground state $^2\mathrm{A}_1$.

For comparison, the HFCCs were also calculated using the DFT/ZORA method with three functionals: the hybrid-GGA functional B3LYP, meta-GGA functional TPSS, and pure-GGA functional BP86. The ORCA code [99] was used for this purpose.

In the present work, we use the same definitions of DKH order for both Hamiltonian and hfc operator; therefore a non-redundant notation DKHn was used instead of DKHn-DKHn (the first for Hamiltonian and the second for hfc operator). The finite nuclear (FN) model described by Gaussian distribution (Eq. 3.30) was used for all DMRG calculations.

3.4   Results and discussion

3.4.1   Ag atom

We have first evaluated the isotropic HFCC of the Ag atom in order to assess our derivation and implementation. The isotropic HFCC of the Ag atom as a function of DKH order and active space is presented in Figure 3.1.

Let us consider the correlation effects. Because the convergent behavior of isotropic HFCC with respect to active space at different DKH orders is similar, we only discuss the results at the DKH3 level. Obviously, the isotropic HFCC smoothly converges with respect to the size of active space. The DMRG-CASSCF(19e,18o) largely underestimates the isotropic HFCC. When the active space is up to CAS(37e,32o), including the extra core orbitals and one $6d$ shell, the calculated value compares reasonable with experimental value. With further extending the active space by polarization $4f$ shell, the isotropic HFCC slightly increases and is in excellent agreement with experimental value.

Next, we discuss the relativistic effects. Lower panel of Figure 3.1 presents the percentage errors of calculated results relative to the experimental value at different DKH orders using DMRG-CASSCF(37e,39o) calculation. Although the DKH1 level improves the isotropic HFCC upon the NR level, its result is still far from experimental value. This means that the wavefunction as well as magnetic operator at DKH1 level is insufficient to obtain the accurate result. Our observation is consistent with many previous works [130–133, 135, 139]. When the DKH level goes from the first to second order, the error significantly decreases from 30.05% to 4.48%. Finally, the correction from third order pushes the result quite close to experimental value.

In general, the performance of DMRG-CASSCF/DKH method at different levels of DKH order and active space for the prediction of isotropic HFCC for the Ag atom has
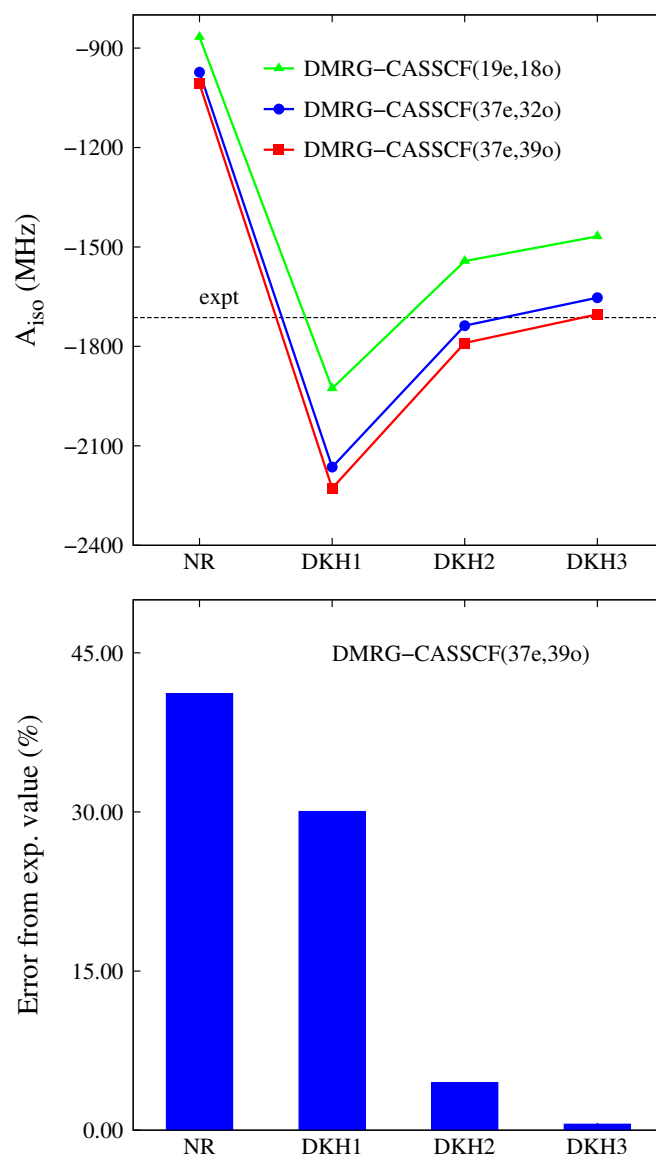
FIGURE 3.1: Upper panel: the isotropic HFCC of Ag atom at different levels of DKH transformation and active space. Lower panel: the percentage error relative to experimental value from DMRG-CASSCF(37e,39o) calculation as a function of DKH order.

been assessed. The error of the DMRG-CASSCF(37e,39o)/DKH3 result relative to the experimental value was found to be only 0.58%. Hereafter, we will only use the DKH3 level fo theory to calculate the isotropic HFCC of PdH and RhH$_2$.

3.4.2 PdH radical

We now consider the PdH radical. All theoretical results calculated in this work are summarized in Table 3.2, along with experimental values in Ar and Ne matrices. For comparison, the results reported by Belanzoni and coworkers are also presented. In

experiment and Belanzori *et al.* works, the parallel component $A_\parallel$ and the perpendicular component $A_\perp$ were provided; therefore, in order to extract the A_{iso} and A_{ani}, we used the following formulas:

$$A_{\mathrm{iso}} = \frac{\left(A_\parallel + 2A_\perp\right)}{3}, \tag{3.35}$$

$$A_{\mathrm{ani}} = \frac{\left(A_\parallel - A_\perp\right)}{3}. \tag{3.36}$$

TABLE 3.2: HFCCs (in MHz) of the Pd center in the PdH radical.

method	A_{iso}(Pd)	A_{ani}(Pd)
BP86/ZORA [a]	−910	29
DHF [b]	552	−7
B3LYP/ZORA	−1207.92	40.07
TPSS/ZORA	−1295.90	38.27
BP86/ZORA	−1358.05	34.84
DMRG-CASSCF(21e,20o)/DKH3	−842.02	40.82
DMRG-CASSCF(21e,32o)/DKH3	−895.35	45.89
DMRG-CASSCF(37e,40o)/DKH3	−867.36	38.68
expt − Ne matrix[c]	−857 (4)	16
expt − Ar matrix[c]	−823 (4)	22

[a] Quiney and Belanzoni, Ref. [15],
[b] Belanzoni *et al.*, Ref. [19],
[c] Taken from Ref. [146].

We mainly focus on the isotropic HFCC of the Pd center. According to the results reported by Belanzoni and coworkers, the DHF terribly underestimates the isotropic HFCC of the Pd center, while more reasonable result can be obtained using BP86/ZORA. The present DFT/ZORA calculations, however, significantly overestimate the isotropic HFCC of the Pd center with the smallest and largest errors relative to Ne matrix value up to 40.84 % (for B3LYP functional) and 58.46 % (for BP86 functional). One of the reasons for the overestimation of DFT/ZORA results is the neglect of FN effect. Previous studies [23, 24, 147] have shown that FN effect reduces the isotropic HFCC of Ag atom by 2.9 %; therefore, the correction of FN effect may not be large enough to get the isotropic HFCC of Pd in good agreement with experimental value.

For DMRG-CASSCF calculations, the result of CAS(21e,20o) is in good agreement with experimental values with an error of 1.75 % relative to the Ne-matrix value. However, when active space is enlarged to CAS(21e,32o), the isotropic HFCC of the Pd center increases. According to Filatov *et al.* [26, 28], the increase of isotropic HFCC is due to the contraction of the atomic inner shell electrons toward the nucleus under effect

of electron correlation. With further increasing the active space to CAS(37e,40o), the isotropic HFCC of the Pd center decreases and is close to Ne-matrix value with an eror of 1.21 %. This means that the DMRG-CASSCF(37e,40o) has captured the higher-order correlation, which is required for the *realistic* accuracy of the isotropic HFCC of the Pd center as expected.

Regarding the anisotropic HFCC, all the methods used in present work largely overestimate its values. The results of DFT are close to those of DMRG-CASSCF. Similarly to isotropic HFCC, the variation of anisotropic HFCC with respect to active space is also non-monotonous.

3.4.3   RhH$_2$ radical

All theoretical and experimental values are collected in Table 3.3. In experiment, only the absolute values of HFCCs were reported; therefore, we also present the absolute values of isotropic HFCCs for consistency. It would be valuable to adapt the HFCCs measured in the Ar matrix containing the methane (CH$_4$) molecules [148]. In such complex, the dipole interaction between RhH$_2$ and CH$_4$ affects the ground state orbitals of RhH$_2$. Thus, the observed EPR spectrum was assigned to the excited states of RhH$_2$ [148].

Because the DMRG-CASSCF(37e,41o)/DKH3 calculation with $M = 512$ has not finished yet, the results with $M = 256$ are reported instead. From the CAS(37e,40o) calculation for PdH in the previous Subsection, we found that the deviation of the result with $M = 256$ from that with $M = 512$ is less than 2.00 %. Thus, we believe that the results with $M = 256$ are reliable.

TABLE 3.3:   HFCCs (in MHz) of the Rh center in the RhH$_2$ radical.

method	$\|A_{\mathrm{iso}}\|$	A_{ani}^x	A_{ani}^y	A_{ani}^z
B3LYP/ZORA	196.59	11.98	-22.91	10.92
TPSS/ZORA	182.87	12.77	-20.02	7.24
BP86/ZORA	192.97	9.04	-24.02	14.97
DMRG-CASSCF(21e,21o)/DKH3	431.06	36.55	-48.92	12.36
DMRG-CASSCF(21e,33o)/DKH3	344.46	22.59	-21.20	-1.38
DMRG-CASSCF(37e,41o)/DKH3 [a]	297.96	20.77	-39.56	18.79
expt $-$ Ar matrix[b]	268($\pm$20)	12	-20	8
expt $-$ CH$_4$/Ar matrix[c]	309($\pm$20)	13	-28	15

[a] $M = 256$.
[b] The results measured in the Ar matrix, Ref. [140].
[c] The results measured in the Ar matrix containing the CH$_4$ molecules, Ref. [148].

We mainly discuss the isotropic HFCC of the Rh center. For DFT/ZORA calculations, the results are less sensitive to the functional. All functionals largely underestimate the isotropic HFCC of the Rh center with the relative errors of around 28.00 %. Similarly to the case of PdH, the inclusion of the FN effect in DFT calculations might not improve upon the calculated value.

For the DMRG-CASSCF/DKH3 calculations, the isotropic HFCC of the Rh center is smoothly converged with respect to the size of active space. The result of CAS(21e,21o) is much higher than the experimental value with an error relative to the average experimental value of 60.82 %. The inclusion of $6d$ and $4f$ shells in the active space, i.e., CAS(21e,33o), leads to a significant reduction in the relative error (28.35 %). From the results of these two active spaces, it is found that including only the inner shell $3s$ is not sufficient to obtain the result comparable to the experimental value. With enlarging the active space to CAS(37e,41o), the error relative to the average experimental value decreases to 11.18 % and the result is close to the upper limit (297.96 MHz compared to 288 MHz). When the FN effect is accounted for, the isotropic HFCC is nonlocal, and not only depends on the spin density at the nucleus position, but also on the spin density in the vicinity of nucleus. Thus, the inclusion of the $3p3d$ inner shells, i.e. CAS(37e,41o), might lead to a proper description of the spin density in the vicinity of the Rh center.

Obviously, the result of the DMRG-CASSCF(37e,41o)/DKH3 calculation falls between the values in the case with and without the presence of CH_4, in other words, between the ground and excited state values. Thus, although it is not straightforward to compare the theoretical value, which corresponds to the gas-phase value, with the value measured in inert gas matrices, we might be able to believe that the experimental isotropic value reported by Zee *et al.* [140] resulted not from the excited states as doubted by Hayton *et al.* [141], but from the ground state.

We now briefly discuss the anisotropic HFCC of the Rh center. The experimental anisotropic HFCCs were extracted using the formula: $A_{ani}^i = |A_i| - |A_{iso}|$, where $i = x, y, z$. According to Zee *et al.* [140], the experimental anisotropic HFCCs are *meaningless* because of the uncertainty in the $x-$component $[A_x = 280(\pm 60)$ MHz]. If the upper limit of A_x was used, A_{ani}^x, A_{ani}^y, and A_{ani}^z would be 52 MHz, -40 MHz, and -12 MHz, respectively. For all DFT/ZORA calculations, the anisotropic HFCCs are in good agreement with the average experimental values. This good agreement is also found for the UHF/DKH3 results (not shown here). For DMRG-CASSCF/DKH3 calculations, the anisotropic HFCCs are seemingly sensitive to the active space and fall in the range between the average and upper limit values.

3.5   Conclusion

In summary, we have newly developed a computational scheme including the high-level electron correlation effects as well as the SR effects for the accurate prediction of isotropic HFCC of heavy molecules. For electron correlation, we employed the DMRG method in framework of the CAS model. The orbital-optimization procedure, i.e., DMRG-CASSCF, was employed to obtain the compact orbitals required for the accuracy of the isotropic HFCC as shown in Chapter 2. For the SR effects, we have derived and implemented the DKH hfc operators up to third order by using the direct transformation scheme. The FN model was used for all DMRG calculations.

As test cases, we have evaluated the HFCCs for $4d$ transition metal radicals: Ag atom, PdH, and RhH_2. Good agreement between the isotropic HFCC values obtained from DMRG-CASSCF/DKH3 and experiment was found. In order to verify the convergence of the isotropic HFCC of the Rh center in RhH_2 radical with respect to active space, the calculation with larger active space is being performed.

It is worth emphasizing that the HFCCs of PdH and RhH_2 were measured in inert gas matrices. According to Filatov and Cremer [26, 28], the effect of the inert gas matrices on the experimental values may reach as much as $6-10\%$. Because there are no available gas-phase values for these radical in literatures, the results from high-level theory, as used in this work, can serve as the benchmark data.

Chapter 4

Molecular $g-$tensors from analytical response theory and quasi-degenerate perturbation theory in framework of CASSCF method

T. N. Lan, J. Chalupský, T. Yanai,

4.1   Introduction

The approaches based on DFT have been widely used for calculations of $g-$tensors due to their low computational requirements; however, they have some major disadvantages as follows. The exchange-correlation functionals appropriate for prediction of $g-$tensors are system-dependent. The use of DFT calculations for properties like $g-$tensors thus requires the careful validation for a given functional. Moreover, a general unsolved question in DFT calculations of magnetic properties is the uncontrollable dependence of the exchange-correlation potential on the paramagnetic current induced by the magnetic field. Thus, the calculation of molecular $g-$tensors using *ab initio* wavefunction methods is still highly desirable.

In the present work, two technical approaches for $g-$tensor calculations based on CASSCF method have been implemented: the first- and second-order perturbation approaches. For the first-order perturbation approach, we employed the QDPT method. For the second-order perturbation approach, we has implemented analytical response theory, referred to as CP-CASSCF, that is equivalent to untruncated SOS expansion within active space. The orbital relaxation under the effect of perturbation, which is the so-called perturbation-induced orbital relaxation, is also considered in this work. As a first step before employing the DMRG-CASSCF method for $g-$tensor calculations, which will be reported in Chapter 5, the FCI level of theory has been used to fully treat the correlation in active space. It is important to remind that the first-order perturbation approach (denoted QDPT herein) includes all orders of SOC effects, while the second-order perturbation approach (denoted CP herein) only includes the first-order (linear) SOC effects.

There are two main purposes of this study: (i) deriving and implementing the analytical response theory for CASSCF method to calculate the molecular $g-$tensors; (ii) making a comparison between the performance of first- and second-order perturbation approaches, which was already reported for DFT methods.

The chapter is organized as follows. The background of theory used in this study is presented in Sec. 4.2 followed by the computational details in Sec. 4.3. Results and discussion are given in Sec. 4.4. Conclusions are drawn in Sec. 4.5

4.2 Theoretical background

4.2.1 Introduction to molecular $g-$tensors

The interaction with the external magnetic field $\mathbf{B}$ is parameterized by the follwing effective spin Hamiltonian

$$H_{\text{eff}} = \mu_B \mathbf{B} \cdot \mathbf{g} \cdot \mathbf{S}_{\text{eff}}, \tag{4.1}$$

where μ_B is the Bohr magneton, $\mathbf{g}$ is the molecular $g-$tensor, and $\mathbf{S}_{\text{eff}}$ is an effective spin operator. Effective spin, which is a fictitious angular momentum, is used to represent the group of degenerate levels that split after application of an external magnetic field.

On the other hand, the molecular Hamiltonian in presence of an external magnetic field is given by

$$H = H_{\text{BO}} + H_{\text{SO}} + H_{\text{Ze}}. \tag{4.2}$$

Here, H_{BO} is the Born-Oppenheimer (BO) Hamiltonian, H_{SO} is the SO operator, and H_{Ze} is the Zeeman operator that can be decomposed into the spin-Zeeman (SZ) H_{SZ} and orbital-Zeeman (OZ) H_{OZ} operators,

$$H_{\mathrm{Ze}} = H_{\mathrm{SZ}} + H_{\mathrm{OZ}}. \tag{4.3}$$

The forms of operators H_{SZ}, H_{OZ}, and H_{SO} will be provided in Subsections 4.2.4 and 4.2.5.

The molecular $g−$tensors can be obtained by comparing the effective spin Hamiltonian (Eq. 4.1) and the molecular Hamiltonian (Eq. 4.2). In the next sections, we will provide two different ways to evaluate the molecular $g−$tensors from the molecular Hamiltonian.

4.2.2   Analytical response theory

Formalism of $g−$tensors

In analytical response theory, both SO and Zeeman operators are considered as perturbation. The $g−$tensor is defined by the second derivative of molecular energy with respect to electron spin and magnetic field,

$$g_{kl} = \frac{1}{\mu_B} \frac{\partial^2 \langle \psi | H | \psi \rangle}{\partial B_k \partial S_l}, \tag{4.4}$$

where $k, l = x, y, z$. Because the derivation of $g−$tensor formula from Eq. 4.4 was already provided in literature [38, 149], we only provide the resultant formula:

$$g_{kl} = \frac{1}{\mu_B} \mathbf{D}^{(\alpha-\beta)} \frac{\partial^2 \mathbf{h}^{\mathrm{SZ}}}{\partial B_k \partial S_l} + \frac{1}{\mu_B} \frac{\partial \mathbf{D}^{(\alpha-\beta)}}{\partial B_k} \frac{\partial \mathbf{h}^{\mathrm{SO}}}{\partial S_l}, \tag{4.5}$$

where $\mathbf{D}^{(\alpha-\beta)}$ is the spin density in atomic orbital (AO) basis, and $h_{\mu\nu}^{\mathrm{SZ}} = \langle \mu | H_{\mathrm{SZ}} | \nu \rangle$ and $h_{\mu\nu}^{\mathrm{SO}} = \langle \mu | H_{\mathrm{SO}} | \nu \rangle$ are SZ and SO integrals in AO basis, respectively. In Eq. 4.5, the first term describes the SZ contribution, while the second term is the cross term between the OZ and SOC contributions. Note that the reduced mass correction (RMC) and the gauge correction (GC) have not been included. According to Bolvin [54], the RMC can be included in the scalar relativistic term, which will be provided later. Also, the gauge-dependent error can be reduced by the choice of proper origin.

The evaluation of the first term is trivial because it only requires the unperturbed spin density. The second term, on the other hand, requires the calculation of the first derivative of the spin density.

The AO spin density from the CASSCF wavefunction is given by

$$D_{\mu\nu}^{(\alpha-\beta)} = \sum_{IJ}\sum_{pq} C_I^* C_J c_{p\mu}^* c_{q\nu} D_{IJ,pq}^{(\alpha-\beta)}, \tag{4.6}$$

where

$$D_{IJ,pq}^{(\alpha-\beta)} = \left\langle I | E_{pq}^- | J \right\rangle, \tag{4.7}$$

and $E_{pq}^- = \hat{a}_{p\alpha}^+ \hat{a}_{q\alpha} - \hat{a}_{p\beta}^+ \hat{a}_{q\beta}$. Taking derivative of spin density (Eq. 4.6), we have

$$\frac{\partial D_{\mu\nu}^{(\alpha-\beta)}}{\partial B_k} = \sum_{IJ}\sum_{pq} \left(\frac{\partial C_I^*}{\partial B_k} C_J + C_I^* \frac{\partial C_J}{\partial B_k} \right) c_{p\mu}^* c_{q\nu} D_{IJ,pq}^{(\alpha-\beta)}$$
$$+ \sum_{IJ}\sum_{pq} C_I^* C_J \left(U_{pn}^* c_{n\mu}^* c_{q\nu} + U_{qn} c_{p\mu}^* c_{n\nu} \right) D_{IJ,pq}^{(\alpha-\beta)}. \tag{4.8}$$

Here, we have employed the rotation matrix $\mathbf{U}$ defined as

$$\frac{\partial c_{p\mu}}{\partial B_k} = U_{pn} c_{n\mu}. \tag{4.9}$$

In the case of magnetic properties, the perturbation is purely imaginary and Hermitian; therefore, $\mathbf{U}$ is a purely imaginary and Hermitian matrix, i.e.,

$$\begin{cases} U_{pq}^* = -U_{pq}, \\ U_{pq} = -U_{qp}. \end{cases} \tag{4.10}$$

Also, we have the following relation

$$\frac{\partial C_I^*}{\partial B_k} = -\frac{\partial C_I}{\partial B_k}. \tag{4.11}$$

According to Eq. 4.8, to evaluate the first order derivative of spin density, we have to solve the CP-CASSCF equations to obtain the first derivatives of CI and MO coefficients. In the present work, we follow the derivation proposed by Yamaguchi and coworkers [150].

We would keep in mind that the external perturbation in the case of $g−$tensors is the OZ operator H_{OZ}. Hereafter, we will employ the operator $\hat{V}$ for the external perturbation for convenience.

MO part of CP-CASSCF equation

We first focus on the MO part. The variational condition in MO space requires a symmetric Lagrangian matrix at convergence

$$\epsilon_{pq} - \epsilon_{qp} = 0. \tag{4.12}$$

Thus, the CP equation for MO coefficients can be obtained by differentiating Eq 4.12

$$\frac{\partial \epsilon_{pq}}{\partial B_k} - \frac{\partial \epsilon_{qp}}{\partial B_k} = 0. \tag{4.13}$$

The Lagrangian is defined by

$$\epsilon_{pq} = \sum_{IJ} C_I^* C_J \epsilon_{pq}^{IJ}, \tag{4.14}$$

where the so-called bare Lagrangian is given by

$$\begin{aligned}
\epsilon_{pq}^{IJ} &= \epsilon_{pq}^{IJ[0]} + \sum_m D_{qm}^{IJ} V_m^p \\
&= \sum_m D_{qm}^{IJ} h_m^p + \sum_{mrs} D_{qmrs}^{IJ} v_{ms}^{pr} + \sum_m D_{qm}^{IJ} V_m^p. \tag{4.15}
\end{aligned}$$

Here, $\boldsymbol{\epsilon}^{[0]}$ is the unperturbed Lagrangian and $\mathbf{V}$ is the perturbation in MO basis, i.e., $V_q^p = \langle p| \hat{V} |q\rangle$. The reduced density matrices are defined by

$$D_q^p = \sum_{IJ} C_I^* C_J D_{pq}^{IJ} = \sum_{IJ} C_I^* C_J \langle I|E_{pq}|J\rangle, \tag{4.16}$$

$$D_{qs}^{pr} = \sum_{IJ} C_I^* C_J D_{pqrs}^{IJ} = \sum_{IJ} C_I^* C_J \langle I|E_{pq}E_{rs} - \delta_{qr} E_{ps}|J\rangle. \tag{4.17}$$

Taking derivative of Lagrangian (Eq. 4.14), we obtain

$$\frac{\partial \epsilon_{pq}}{\partial B_k} = \sum_{IJ} C_I^* C_J \frac{\partial \epsilon_{pq}^{IJ}}{\partial B_k}. \tag{4.18}$$

To obtain Eq. 4.18, we have used the relation 4.11. Substituting Eq. 4.15 into Eq. 4.18 and using the relation 4.10, we obtain the final equation for first derivative of Lagrangian as follows:

$$\frac{\partial \epsilon_{pq}}{\partial B_k} = \sum_{rs} U_{rs} \left(\delta_{pr} \epsilon_{qs}^{[0]} + Y_{qs}^{pr} \right) + V_q^{p[B]}. \tag{4.19}$$

Here, the 4-indices matrix is given by

$$Y_{qs}^{pr} = \sum_{mnrs} \left(D_s^q h_r^p + D_{sn}^{qm} v_{rn}^{pm} \right),$$
(4.20)

and we have defined

$$V_q^{p[B]} = \sum_{\mu\nu} c_{p\mu}^* c_{q\nu} \frac{\partial V_{\mu\nu}}{\partial B_k}.$$
(4.21)

Finally, substituting Eq. 4.19 into Eq. 4.13, we obtain the CP equation for MO part

$$\sum_{rs} U_{rs} \left(\delta_{pr} \epsilon_{qs}^{[0]} - \delta_{qr} \epsilon_{ps}^{[0]} + Y_{qs}^{pr} - Y_{ps}^{qr} \right) = -V_q^{p[B]} + V_p^{q[B]}.$$
(4.22)

The spin density matrices vanish unless both indices p and q in Eq. 4.8 are active. In addition, the interaction through the perturbation within the active space will be treated by CI part. Thus, the rotation matrix $\mathbf{U}$ can be decomposed into core-active and active-virtual contributions. It is expected that the contribution of core orbitals to molecular $g−$tensors is small [51, 53]. Therefore, we have neglected the core-active rotation by introducing a frozen core approximation in the current implementation.

CI part of CP-CASSCF equation

We now derive CP equation for CI part. The variational condition for CI part is

$$\sum_J C_J \left(H_{IJ} - \delta_{IJ} E_0 \right) = 0.$$
(4.23)

The CP equation for CI part is derived by differentiating the variational condition 4.23 with respect to magnetic field B_k subject to the normalized constrain

$$\frac{\partial}{\partial B_k} \left[\sum_J C_J \left(H_{IJ} - \delta_{IJ} E_0 \right) - \theta \left(1 - \sum_K C_K^* C_K \right) \right] = 0,$$
(4.24)

where θ is a Lagrangian multiplier. The derivative of second parentheses in Eq. 4.24 is zero because of the relation 4.11; therefore, we obtain

$$\sum_J \frac{\partial C_J}{\partial B_k} \left(H_{IJ} - \delta_{IJ} E_0 \right) + \sum_J C_J \frac{\partial H_{IJ}}{\partial B_k} = 0.$$
(4.25)

Here, the so-called bare Hamiltonian is given by

$$H_{IJ} = H_{IJ}^{[0]} + \sum_{pq} D_{pq}^{IJ} V_q^p$$

$$= \sum_{pq} D_{pq}^{IJ} h_q^p + \frac{1}{2} \sum_{pqrs} D_{pqrs}^{IJ} v_{qs}^{pr} + \sum_{pq} D_{pq}^{IJ} V_q^p, \tag{4.26}$$

where $H_{IJ}^{[0]}$ is the unperturbed bare Hamiltonian. Using the definition 4.9, we obtain

$$\frac{\partial h_q^p}{\partial B_k} = \sum_n \left(U_{pn}^* h_q^n + U_{qn} h_n^p \right), \tag{4.27}$$

$$\frac{\partial v_{qs}^{pr}}{\partial B_k} = \sum_n \left(U_{pn}^* v_{qs}^{nr} + U_{qn} v_{ns}^{pr} + U_{rn}^* v_{qs}^{pn} + U_{sn} v_{qn}^{pr} \right), \tag{4.28}$$

and

$$\frac{\partial V_q^p}{\partial B_k} = \sum_n \left(U_{pn}^* V_q^n + U_{qn} V_n^p \right) + V_q^{p[B]}. \tag{4.29}$$

Substituting Eqs. 4.27−4.29 into Eq. 4.25 and using the relation 4.10, the resultant CP equation for CI part is

$$\sum_J \frac{\partial C_J}{\partial B_k} \left(H_{IJ} - \delta_{IJ} E_0 \right) = -\sum_J C_J \sum_{pq} D_{pq}^{IJ} V_q^{p[B]}. \tag{4.30}$$

Generally, by solving Eqs. 4.22 and 4.30 we obtain the first derivatives of MO and CI coefficients, and then obtain the first derivative of spin density.

4.2.3 Quasi-degenerate perturbation theory

Formalism of $g−$tensors

If we suppose that the SOC effects have already been included in the wavefunction, the Zeeman energy is regarded as the first-order perturbation. According to Kramers theorem, for a molecule containing an odd number of electrons, all states remain at least two-fold degenerate in the absence of external magnetic field. Such a pair of states forms a Kramers doublet $\{\Phi, \bar{\Phi}\}$, in which the states are connected to each other by the time-reversal symmetry, i.e., $\Phi = K\bar{\Phi}$, where

$$K = \prod_{p=1}^n -i\sigma_y(p) K_0(p). \tag{4.31}$$

Here, $p = 1, 2, ..., n$ refers to the action of the operator on the p-th electron and K_0 is the operator converting a wavefunction into its complex conjugate., i.e., $\psi^* = K_0\psi$. From Eq. 4.31, we obtain $K^2 = -1$.

The Zeeman energy splitting in the basis of a Kramers doublet can be defined as

$$\Delta E_{\text{Ze}} = \begin{pmatrix} \langle\Phi|H_{\text{Ze}}|\Phi\rangle & \langle\Phi|H_{\text{Ze}}|\bar{\Phi}\rangle \\ \langle\bar{\Phi}|H_{\text{Ze}}|\Phi\rangle & \langle\bar{\Phi}|H_{\text{Ze}}|\bar{\Phi}\rangle \end{pmatrix}. \tag{4.32}$$

On the other hand, the energy splitting induced by the spin Hamiltonian 4.1 is

$$\Delta E_{\text{eff}} = \frac{\mu_B}{2} \sum_k B_k \begin{pmatrix} g_{kz} & g_{kx} - ig_{ky} \\ g_{kx} + ig_{ky} & -g_{kz} \end{pmatrix}. \tag{4.33}$$

The factor $^1/_2$ arises from the relation $\mathbf{S}_{\text{eff}} = {}^1/_2\,\boldsymbol{\sigma}$; where $\boldsymbol{\sigma}$ is a 3-vector of 2×2 Pauli matrices. The components of $g−$tensors are then obtained by requiring that both energy differences calculated from Eq. 4.32 and 4.33 are equal. Thus, the resulting formulas of $g−$tensor matrix elements are

$$\begin{aligned} g_{kx} &= \frac{2}{\mu_B}\text{Re}\,\langle\Phi|\,\frac{\partial H_{\text{Ze}}}{\partial B_k}\,|\bar{\Phi}\rangle = \frac{2}{\mu_B}\text{Re}\,\langle\bar{\Phi}|\,\frac{\partial H_{\text{Ze}}}{\partial B_k}\,|\Phi\rangle, \\ g_{ky} &= -\frac{2}{\mu_B}\text{Im}\,\langle\Phi|\,\frac{\partial H_{\text{Ze}}}{\partial B_k}\,|\bar{\Phi}\rangle = \frac{2}{\mu_B}\text{Im}\,\langle\bar{\Phi}|\,\frac{\partial H_{\text{Ze}}}{\partial B_k}\,|\Phi\rangle, \\ g_{kz} &= \frac{2}{\mu_B}\text{Re}\,\langle\Phi|\,\frac{\partial H_{\text{Ze}}}{\partial B_k}\,|\Phi\rangle = \frac{2}{\mu_B}\text{Im}\,\langle\bar{\Phi}|\,\frac{\partial H_{\text{Ze}}}{\partial B_k}\,|\bar{\Phi}\rangle. \end{aligned} \tag{4.34}$$

The wave functions of Kramers doublet $\{\Phi, \bar{\Phi}\}$ that include the SOC effects can be obtained either variationally, or by QDPT approach as we have done so in this work.

QDPT wavefunction

Supposing we have pre-calculated the wavefunctions of several one-component (1c) non-relativistic or SR electronic states

$$\left|\Psi_I^{SM}\right\rangle = \sum_i C_{iI}\,|\Phi_i\rangle, \tag{4.35}$$

where S is the total spin quantum number, M is the projection onto the z-axis ($M = -S, ..., S$), and $\{|\Phi_i\rangle\}$ is the determinant basis (CI space). These wavefunctions are the eigenfunctions of the spin-independent BO Hamiltonian H_{BO}. When the SO operator is turned on, the molecular Hamiltonian is spin-dependent. In QDPT method, the SOC effect is accounted for by constructing a matrix representation of molecular Hamiltonian

in the basis of states $\{\Psi_I^{SM}\}$

$$\left\langle \Psi_I^{SM} | H_{\mathrm{BO}} + H_{\mathrm{SO}} | \Psi_J^{S'M'} \right\rangle = \delta_{IJ}\delta_{SS'}\delta_{MM'}E_I + \left\langle \Psi_I^{SM} | H_{\mathrm{SO}} | \Psi_J^{S'M'} \right\rangle, \qquad (4.36)$$

where E_I is the eigenvalue of BO state I. By diagonalizing matrix 4.36, the eigenvalues yield SOC-corrected state energies, and the eigenvectors represent the relativistic 2c wavefunctions, which can be used for property calculations.

In practical QDPT calculations, the number of states used as basis for construction of matrix 4.36 is limited, and truncation errors are thus introduced.

4.2.4   Direct DKH transformation for Zeeman operators

Following the derivation of DKH transformation for magnetic operators using direct scheme provided in Chapter 3, the resultant equations for the DKH Zeeman operator up to the second order reads

$$H_{\mathrm{Ze},1}^{(2)} = H_{\mathrm{mag}} + H_{\mathrm{mag}}^+, \qquad (4.37)$$

$$\begin{aligned} H_{\mathrm{Ze},2}^{(2)} = \ & H_{\mathrm{Ze},1}^{(2)} - \left(A\tilde{V}A \right) H_{\mathrm{mag}} + \left(AR\tilde{V}RA \right) R_p^{-2} H_{\mathrm{mag}} \\ & - \left(AR\tilde{V}RA \right) H_{\mathrm{mag}}^+ + \left(A\tilde{V}A \right) R_p^2 H_{\mathrm{mag}}^+ \\ & - H_{\mathrm{mag}}^+ \left(A\tilde{V}A \right) + H_{\mathrm{mag}}^+ R_p^{-2} \left(AR\tilde{V}RA \right) \\ & - H_{\mathrm{mag}} \left(AR\tilde{V}RA \right) + H_{\mathrm{mag}} R_p^2 \left(A\tilde{V}A \right), \end{aligned} \qquad (4.38)$$

where

$$A\tilde{V}A = A_p \frac{V(p,p')}{E_p + E_{p'}} A_p, \qquad (4.39)$$

$$AR\tilde{V}RA = A_p R_p \frac{V(p,p')}{E_p + E_{p'}} R_p A_p, \qquad (4.40)$$

and

$$H_{\mathrm{mag}} = A_p K_p \left(\boldsymbol{\sigma}\mathbf{p} \right) \left(\boldsymbol{\sigma}\mathbf{A} \right) A_p, \qquad (4.41)$$

$$H_{\mathrm{mag}}^+ = A_p \left(\boldsymbol{\sigma}\mathbf{A} \right) \left(\boldsymbol{\sigma}\mathbf{p} \right) K_p A_p. \qquad (4.42)$$

The superscript (2) in Eqs 4.37 and 4.38 means that the DKH operators are in 2c picture. The kinetic energy E_p and kinetic factors A_p and K_p are defined by

$$E_p = c\sqrt{p^2 + m^2 c^2}, \tag{4.43}$$

$$A_p = \sqrt{\frac{E_p + mc^2}{2E_p}}, \tag{4.44}$$

$$K_p = \frac{c}{E_p + mc^2}. \tag{4.45}$$

Using the relation $(\boldsymbol{\sigma}\mathbf{a})(\boldsymbol{\sigma}\mathbf{b}) = \mathbf{a}\cdot\mathbf{b} + i\boldsymbol{\sigma}\cdot(\mathbf{a}\times\mathbf{b})$, we obtain, for example, the DKH1 Zeeman operator

$$\begin{aligned} H_{\mathrm{Ze},1}^{(2)} =& A_p K_p i\boldsymbol{\sigma}\left[\mathbf{p}\times\mathbf{A}\right] A_p - A_p i\boldsymbol{\sigma}\left\{K_p\left(\mathbf{A}\times\mathbf{p}\right) - \left(\mathbf{A}\times\mathbf{p}\right)K_p\right\} A_p \\ &+ A_p\left\{K_p\mathbf{A}\cdot\mathbf{p} + \mathbf{A}\cdot\mathbf{p}K_p\right\} A_p. \end{aligned} \tag{4.46}$$

Herein, square brackets mean that the operator $\mathbf{p}$ only acts on the vector potential $\mathbf{A}$, but not on the wavefunction. As mentioned in Chapter 3, the second term in Eq. 4.46 will be neglected.

In the case of $g−$tensors, the vector potential created by external magnetic field $\mathbf{B}$ is given by

$$\mathbf{A} = \frac{1}{2}\left(\mathbf{B}\times\mathbf{r}\right). \tag{4.47}$$

Therefore, we obtain

$$\mathbf{A}\mathbf{p} = \frac{1}{2}\left(\mathbf{B}\times\mathbf{r}\right)\mathbf{p} = \frac{1}{2}\mathbf{B}\left(\mathbf{r}\times\mathbf{p}\right) = \frac{1}{2}\mathbf{L}\mathbf{B}, \tag{4.48}$$

$$i\boldsymbol{\sigma}\left[\mathbf{p}\times\mathbf{A}\right] = i\frac{\boldsymbol{\sigma}}{2}\left[\mathbf{B}\left(\mathbf{p}\cdot\mathbf{r}\right) + \mathbf{r}\left(\mathbf{p}\cdot\mathbf{B}\right) - \left(\mathbf{B}\cdot\mathbf{p}\right)\mathbf{r} - \left(\mathbf{r}\cdot\mathbf{p}\right)\mathbf{B}\right] = \boldsymbol{\sigma}\cdot\mathbf{B}. \tag{4.49}$$

To obtain Eq. 4.49, we have used $\mathbf{p}\cdot\mathbf{B} = 0$ and $\mathbf{p}\cdot\mathbf{r} = 3$. Substituting Eqs. 4.48 and 4.49 into Eq. 4.46, we obtain

$$H_{\mathrm{Ze},1}^{(2)} = \mu_B\frac{g_e}{2}A_p R_p\left(\boldsymbol{\sigma}\cdot\mathbf{B}\right)A_p + \frac{\mu_B}{2}\left[A_p R_p\left(\mathbf{L}\cdot\mathbf{B}\right)A_p + A_p\left(\mathbf{L}\cdot\mathbf{B}\right)R_p A_p\right]. \tag{4.50}$$

The factor $g_e/2$ was introduced in order to account for small quantum-electrodynamic effects. The first term in Eq. 4.50 is the SZ interaction H_{SZ} and the second term is the OZ interaction H_{OZ}.

In the NR limit $(c\to\infty)$, the kinetic factors $A_p\to 1$ and $K_p\to(2c)^{-1}$. The usual NR operator can then be obtained.

4.2.5   Flexible nuclear screening spin-orbit approximation

In this subsection, we will briefly introduce the central idea of FNSSO approximation. In the quasirelativistic theory at the Breit-Pauli (BP) level, the SO operator can be written as a simple sum of one- and two-electron contributions and reads

$$\hat{H}^{\text{SO}} = \hat{H}^{1el\text{-SO}} + \hat{H}^{2el\text{-SO}} = \sum_i \hat{h}(i) + \frac{1}{2} \sum_i \sum_{j \neq i} \hat{g}(i,j). \tag{4.51}$$

The evaluation of SO matrix elements using the full SO operator is often too expensive to be practical. In order to simplify the evaluation, the mean-field approximation was introduced [151]

$$\hat{H}^{\text{SO}} \approx \hat{H}^{\text{MF}} = \sum_i \hat{\mathbf{f}}_i \cdot \hat{\mathbf{s}}_i, \tag{4.52}$$

where $\hat{\mathbf{f}}$ is a Fock-like operator.

The Fock-like matrix elements can be formally rewritten as

$$\mathbf{f}_{ij} = \mathbf{f}_{ij}^{1el} + \mathbf{f}_{ij}^{2el}, \tag{4.53}$$

and we may define quantity

$$Q_{ij}^{(\mu)} = \frac{f_{ij}^{1el(\mu)} - f_{ij}^{(\mu)}}{f_{ij}^{1el(\mu)}} = \frac{-f_{ij}^{2el(\mu)}}{f_{ij}^{1el(\mu)}}, \tag{4.54}$$

where μ is one of the three spatial components. This quantity represents the ratio of the two- and one-electron parts of the Fock matrix elements, i.e., the degree of screening of the one-electron SO interactions caused by the corresponding two-electron interactions. The $\mathbf{Q}_{ij}$ quantities are therefore referred to as *screening parameters*. A new effective one-electron SO Fock operator is then defined based on the screening parameters in two different ways. Firstly, the general *2-dimensional* screening parameters can be used to define the operator with the relation

$$f_{ij}^{\text{FNSSO}_{2\text{D}}(\mu)} = f_{ij}^{1el(\mu)} \left(1 - Q_{ij}^{(\mu)}\right), \tag{4.55}$$

or, secondly, the screening effect can be approximated using *1-dimensional* screening parameters, and the operator is defined as

$$f_{ij}^{\text{FNSSO}_{1\text{D}}(\mu)} = f_{ij}^{1el(\mu)} \left(1 - \sqrt{Q_{ii}^{(\mu)} Q_{jj}^{(\mu)}}\right). \tag{4.56}$$

Thus, once we know the screening parameters, which actually can be tabulated, the SO matrix elements can be obtained. For more details about this methodology, reader is referred to Ref. [84].

Note that all the formulas and arguments given above apply equally well to both BP and DKH formalisms.

TABLE 4.1: Active orbitals and geometries for small radicales used in this work.

Radical	Active space	Active orbitals	Bond length [Å] and angles [°]
BO	CAS(9e,8o)	B 2s2p; O 2s2p	1.212^a
CO^+	CAS(9e,8o)	C 2s2p; O 2s2p	1.150^a
CN	CAS(9e,8o)	C 2s2p; N 2s2p	1.172^a
AlO	CAS(9e,8o)	Al 3s3p; O 2s2p	1.618^a
BS	CAS(9e,8o)	B 2s2p; S 3s3p	1.620^a
CO_2^-	CAS(17e,12o)	C 2s2p; O 2s2p	C–O 1.233; O–C–O 137.60^b
H_2CO^+	CAS(11e,10o)	C 2s2p; O 2s2p; H 1s	H–C 1.112; C–O 1.195; H–C–O 118.76^b
H_2O^+	CAS(7e,6o)	O 2s2p; H 1s	H–O 0.997; H–O–H $1.09.17^b$
NF_2	CAS(19e,12o)	O 2s2p; F 2s2p	N–F 1.340; F–N–F 103.57^b
NO_2	CAS(17e,12o)	O 2s2p; N 2s2p	N–O 1.199; O–N–O 134.28^b
O_2	CAS(12e,8o)	O 2s2p	1.235^c
NH	CAS(6e,5o)	N 2s2p; H 1s	1.053^c
NF	CAS(12e,8o)	N 2s2p; F 2s2p	1.343^c
NCl	CAS(12e,8o)	N 2s2p; Cl 3s3p	1.643^c
NBr	CAS(12e,8o)	N 2s2p; F 3s3p	1.808^c
NI	CAS(12e,8o)	N 2s2p; I 3s3p	2.007^c
S_2	CAS(12e,8o)	S 3s3p	1.931^c
PH	CAS(6e,5o)	P 3s3p; H 1s	1.453^c
SO	CAS(12e,8o)	S 3s3p; O 2s2p	1.518^c
SeO	CAS(12e,8o)	Se 4s4p; O 2s2p	1.677^c
PdH	CAS(11e,15o)	Pd 4d5s5p5d; H 1s	1.529^d
CdH	CAS(3e,11o)	Cd 5s5p5d6s; H 1s	1.781^d
HgH	CAS(3e,11o)	Hg 6s6p6d7s; H 1s	1.766^d
RhH_2	CAS(11e,8o)	Rh 4d5s; H 1s	Rh–H 1.510; H–Rh–H 84.00^e
IrH_2	CAS(11e,8o)	Ir 5d6s; H 1s	Ir–H 1.540; H–Ir–H 91.90^f

[a] Ref. [98]
[b] Ref. [49]
[c] Ref. [35]
[d] Ref. [19]
[e] Ref. [145]
[f] Ref. [152]

4.3   Computational details

The active spaces and molecular geometries for small molecules used in the present work are collected in Table 4.1. The geometries of light and heavy diatomic $^2\Sigma$ radicals were taken from experiments reported in Ref. [98] and Ref. [19]; and those of light polyatomic $^2\Sigma$ radicals were adapted from MP2 calculations reported by Brownridge *et al.* [49]. Because there are no available experimental geometries for RhH_2 and IrH_2 radicals, we adapted them from MRCI-SD calculations reported by Balasubramanian and coworkers [145, 152]. We also used the optimized geometries for diatomic $^3\Sigma$ radicals provided by Patchkovskii and Ziegler [35]. The ANO-RCC-TZP basis set [153, 154] was used for all radicals studied herein.

The effect of quartet states is expected to be very small for light doublets. Their role was tested for heavy radicals and was found to be also negligible compared to the contribution of the doublet states. Thus, the quartet states were not considered in all QDPT calculations. In order to investigate the influence of pertubation-induced orbital relaxation, we employed two notations: CP-CI and CP-CAS. In the former, only the CP equation of CI part is solved; while in the later, the perturbation-induced orbital relaxation is accounted for too.

Throughout this work, the gauge-origin is taken as the center of electronic charge [155] to reduce the gauge-dependent error.

4.4   Results and discussions

4.4.1   Test cases: main group radicals

We first validate our implementation by calculating the $g−$tensors for small radicals. Here we consider two test sets: 10 $^2\Sigma$ and 10 $^3\Sigma$ radicals. The non-relativistic Hamiltonian and BP SO operator were used for these test cases. We will mainly focus on the performance of methods rather than the detailed analyses of calculated $g−$tensors.

Doublet radicals

Let us begin with discussing the set of doublet radicals. All calculated results are presented in Table 4.2 along with the experimental values. For comparison, the SOS-MRCI results by Brownridge *et al.* [49] and the CP-MRCI results by Neese [51] were also adapted for comparison. For diatomic radicals, only the $\Delta g_\perp$ component is reported.

From a comparison of the CP-CI and CP-CAS results, we found that the effect of the perturbation-induced orbital relaxation on g−values is generally small, although with exceptions in case of some diatomic radicals. The perturbation-induced orbital relaxation reduces the absolute value of CP-CI results in most cases. The largest effect was observed for the CN radical, where the magnitute of $\Delta g_\perp$ was reduced from -1732 to -1553 ppm.

TABLE 4.2: Δg values (ppm) for 10 $^2\Sigma$ radicals.

Radical	Δg	CP-CASSCF		QDPT-CASSCF		SOS-MRCI	CP-MRCI	expt [a]
		CP-CI	CP-CAS	10 states	30 states	Ref.[49]	Ref. [51]	
BO		-1118	-980	-375	-1143	-1735	-1482	-1100
CO^+		-2088	-1889	-479	-2109	-2015	-2094	-2400
CN	$\Delta g_\perp$	-1732	-1553	-1812	-1721	-1715	-1702	-2000
AlO		-1102	-1124	353	-1122	-1530	-1761	-1200
BS		-5356	-5194	-6169	-5331	-7740		-8455
CO_2^-	Δg_{xx}	1911	1606	1518	1664	655		700
	Δg_{yy}	-3455	-3328	-3509	-3437	-5080		-4800
	Δg_{zz}	-391	-446	-497	-391	-1110		-500
H_2CO^+	Δg_{xx}	4889	4995	5074	5138	5840		4600
	Δg_{yy}	1081	1281	1045	1082	240		-800
	Δg_{zz}	114	117	4	143	300		200
H_2O^+	Δg_{xx}	18	1	22	31	15	46	200
	Δg_{yy}	11540	11558	11529	11532	16025	11287	18800
	Δg_{zz}	4400	4068	4387	4390	4210	4178	4800
NF_2	Δg_{xx}	-398	-447	11	-31	-470		-100
	Δg_{yy}	5927	5765	5990	5941	5985		6200
	Δg_{zz}	3577	3510	3468	3553	3220		2800
NO_2	Δg_{xx}	4403	4297	3517	4036	3400		3900
	Δg_{yy}	-8207	-8059	-8158	-8216	-11830		-11300
	Δg_{zz}	-360	-377	-485	-344	-440		-300

[a] Experimental values taken from Refs. [38, 49]

For the QDPT-CASSCF calculations, we used two values of number of roots: 10 and 30. The convergence of the g−tensors with respect to the number of roots for polyatomic radicals is more rapid than that for diatomic radicals. The results from CP-CI and QDPT with 30 roots are comparable to each other. This means that the higher-order SOC effects are negligible for these test radicals.

Let us compare our CASSCF results with those from the MRCI and experiment. Because the QDPT results are quite close to the results from the CI part of CP-CASSCF, we only discuss the CP-CASSCF results.

For BO, both MRCI calculations significantly overestimate the absolute value of $\Delta g_\perp$, while our CP-CASSCF results are consistent with the experimental value.

For CO^+ and CN, the $\Delta g_\perp$ calculated by CP-CI agree well with the MRCI results and seem to be comparable to the experimental values. The perturbation-induced orbital relaxation reduces the $\Delta g_\perp$, leading to worse agreement with errors of 21.29 % for CO^+ and 22.35 % for CN.

For AlO, the perturbation-induced orbital relaxation has a minor effect on $g−$tensors. It is well known that the AlO radical is a difficult case [39, 49, 52]. Our results are, however, quite close to the experimental value. The error was found to be only 6.33 %. It is possible that this good agreement resulted from an error cancellation.

For BS, our CP-CASSCF result is less negative than the MRCI and experimental values. The error of CP-CAS result relative to the experimental value is up to 38.57 %.

For CO_2^-, the Δg_{xx} and Δg_{yy} values determined by CP-CASSCF are more positive and less negative than the experimental values, respectively. The reasonable agreement was only observed for Δg_{zz}.

For H_2CO^+, the SOS-MRCI significantly overestimate the Δg_{xx}, while that from CP-CASSCF is in good agreement with the experimental value (errors of 6.28 % for CP-CI and 8.28 % for CP-CAS).

For H_2O^+, the Δg_{yy} value of CP-CASSCF calculation is far from that of experiment. According to previous studies [39, 49, 52], the Δg_{yy} component of H_2O^+, which is dominated by the excitation of electron from doubly occupied σ to singly occupied oxygen lone pair orbital, is quite sensitive to the level of theory. Interestingly, the Δg_{yy} of H_2O^+ calculated by the CP-CI is quite close to that calculated by the CP-MRCI. Neese has attributed the failure of the CP-MRCI for the case of H_2O^+ to the lack of the perturbation-induced orbital relaxation. However, we have found that the effect of the perturbation-induced orbital relaxation on the Δg_{yy} of H_2O^+ is negligible.

For NF_2, all components of Δg calculated by the CP-CASSCF are close to those calculated by the SOS-MRCI. Good agreement with the experimental value was found for Δg_{yy} with an error of around 7.00 %.

For NO_2, the CP-CASSCF Δg_{xx} and Δg_{zz} seem to agree well with the experimental value, while the CP-CASSCF Δg_{yy} is less negative.

Triplet radicals

Let us now turn to the test set consisting of ten $^3\Sigma$ radicals. The calculated and experimental values are collected in Table 4.3. For comparison, the results from the linear response CASSCF (LR-CASSCF) by Engström *et al.* [156], the SOS-MRCI and multireference spin-orbit configuration interction (MRSOCI) by Tatchen *et al.* [55], as well as the CP-MRCI by Neese [51] were adapted. To be consistent with previous theoretical results, we presented the $\Delta g_\perp$ in ppt instead of ppm, which was used above for doublet molecules.

Obviously, the effect of perturbation-induced orbital relaxation on $g−$tensors is much smaller than that for the doublet radicals. The largest change was observed for SeO radical, in which the $\Delta g_\perp$ value increases about 5.00 % under perturbation-induced orbtial relaxation.

Our results are generally consistent with the LR-CASSCF results except for the case of SO, for which the CP-CASSCF provides much higher values. This large inconsistency originates mainly from the difference in $r_e(S−O)$ used in the present (1.518 Å) and previous (1.481 Å) calculation.

We now compare our CP-CASSCF results with the MRCI and experimental values. We will only focus on the results with perturbation-induced orbital relaxation.

TABLE 4.3: $\Delta g_\perp$ values (ppt) for 10 $^3\Sigma$ radicals.

Radical	CP-CASSCF		LR-CASSCF	SOS-MRCI	MRSOCI	CP-MRCI	expt [a]
	CP-CI	CP-CAS	Ref. [156]	Ref.[55]	Ref. [55]	Ref. [51]	
O_2	2.9	2.9	3.0	2.5	2.7		2.9
NH	1.2	1.2	1.5	1.3	1.3	1.3	1.7
NF	1.8	1.7	2.1	1.8	1.8		2.0
NCl	4.4	4.4	4.1	4.4	4.8		5.4
NBr	16.0	16.7		14.3	16.4		19.3
NI	35.3	36.6					31.0
S_2	13.0	12.9	11.2	12	12.9		14.5
PH	3.6	3.6	4.0	3.8	3.8	3.9	4.5
SO	5.9	6.0	4.1				3.6
SeO	25.2	26.7					32.7

[a] Experimental values taken from Ref [35]

First of all, O_2 is one of the well-studied test cases of a triplet radical. While the MRCI results are lower than the experimental value, excellent agreement is found for the CASSCF results.

For NH, NF, NCl, and NBr, it is interesting that our CP-CASSCF results are quite close to that from the MRCI caculations. Because the SOS-MRCI and MRSOCI results are comparable to each other, it is possible to conclude that the higher-order SOC contribution is negligible in these systems. The theoretical results are smaller than the experimental values with the largest error for NH (~ 29 %).

For NI, our CP-CASSCF result is in reasonable agreement with the experimental value. As previously shown by Malkin *et al.* [31] the higher-order SOC effects are non-negligible for this radical and the agreement of CP-CASSCF result is questionable.

For S_2, all CP-CASSCF and MRCI results are consistent with each other. The effects of higher-order SOC are small and good agreement with the experimental value was found.

For PH, our CP-CASSCF result is a bit lower than the MRCI results and significantly lower than the experimental value with an error of 20.00 %.

For SO, it is unfortunate that our CP-CASSCF largely overestimates the $\Delta g_\perp$ with an error of up to 66.67 % relative to the experimental value.

Finally, for SeO, CP-CASSCF provides the result that is in reasonable agreement with the experimental value. However, similarly to NI, the higher-order SOC effects play an important role for this radical [31], and this agreement might be fortuitous.

In summary, we have assessed our implementation to evaluate the $g−$tensors for two test sets containing main group radicals: 10 $^2\Sigma$ and 10 $^3\Sigma$ radicals. It has been shown that our results generally agree well with MRCI results, especially for triplet radicals. Good agreement with the experimental values has been found in many cases. We do not aim to provide the highly accurate data for these test cases. Rather, we want to validate our approach, formulation and implementation, especially for the new CP-CASSCF implementation.

4.4.2 Transition metal hydrides and dihydrides

In this subsection, we will evaluate the $g−$tensors for selected hydride and dihydride radicals, namely PdH, CdH, HgH, RhH_2, and IrH_2. While the characterization of $g−$tensors for three hydrides was already published, this is the first time to present the *ab initio* calculations of $g−$tensors for the two dihydrides.

Picture change error

We define the relativistic notation A–B–C, in which the A, B, and C symbols stand for the BO Hamiltonian (DKH2 for all calculations), the SO operator (BP, DKH1, or DKH2), and the Zeeman operator (NR, DKH1, or DKH2), respectively. We next define the quasi-relativistic (qrel) levels as follows

+ qrel-1: DKH2–BP–NR,

+ qrel-2: DKH2–DKH1–NR,

+ qrel-3: DKH2–DKH1–DKH1,

+ qrel-4: DKH2–DKH2–DKH2.

See Subsection 4.2.4 for the detailed derivation of the DKH Zeeman operator. Comparing the qrel-2 and qrel-3 values, we will be able to figure out the PCE of the Zeeman operator.

Let us first consider the effect of the qrel-level on the g−tensors of these radicals. The QDPT-CASSCF method, in which the number of roots was set to 10 for PdH radical and to 30 for others, was used. All calculated results are summarized in Table 4.4.

TABLE 4.4: Δg values (ppt) for hydrides and dihydrides at different quasi-relativistic (qrel) levels. See the text for the definition of the qrel levels.

Radical	Δg	qrel-1	qrel-2	qrel-3	qrel-4
PdH	$\Delta g_{\parallel}$	−17.7	−16.9	−17.3	−17.3
	$\Delta g_{\perp}$	261.4	256.3	255.8	256.7
CdH	$\Delta g_{\parallel}$	−1.3	−1.0	−1.1	−1.0
	$\Delta g_{\perp}$	−55.4	−47.2	−47.3	−48.3
HgH	$\Delta g_{\parallel}$	−73.1	−21.4	−21.6	−23.6
	$\Delta g_{\perp}$	−495.1	−251.3	−251.4	−264.2
RhH$_2$	Δg_{xx}	−64.2	−61.9	−62.4	−62.8
	Δg_{yy}	722.9	712.4	711.6	713.2
	Δg_{zz}	846.6	834.4	833.6	835.4
IrH$_2$	Δg_{xx}	−344.2	−323.6	−324.1	−326.2
	Δg_{yy}	1475.4	1448.6	1447.5	1450.1
	Δg_{zz}	1198.7	1188.8	1187.8	1188.8

The qrel-1 value is significantly different in comparison with the value at the qrel-4 level, which is the highest qrel level used in this work. The largest effect was observed for HgH, where the qrel-1 $\Delta g_{\perp}$ is almost twice as big as that of the qrel-4 level. This confirms the

well-known conclusion that only scalar relativistic wavefunction is insufficient and relativistic level of SO operator needs to go beyond the BP level to accurately characterize $g-$tensors of radicals containing heavy elements.

On the other side, the qrel-2 and qrel-3 levels provide the values that are comparable to the qrel-4 value. The negligibility of the PCE for the Zeeman operator is reflected by very small deviation between the qrel-2 and qrel-3 values. In general, the DKH2 wavefunction in combination with the DKH1 SO operator is sufficient for reliable predictions of $g-$tensors for heavy molecules studied herein.

Interestingly, the change in $\Delta g-$values when the relativistic level of the SO operator goes from BP to DKH1 is more significant for CdH and HgH than for RhH$_2$ and IrH$_2$. The SOC in the formers are dominated by coupling between p orbtials, while that in the laters is dominated by coupling between d orbitals. Because the relativistic effects are stronger when the orbitals localize closer to the nucleus, this explains the observed behavior.

First-order versus second-order perturbation treatments

For light radicals studied in Subsection 4.4.1, SOC is relatively weak. Thus, the higher-order SO contributions are negligible. That is the reason why $g-$tensors obtained by CP- and QDPT-CASSCF are close to each other. It is well known that the SOC increases significantly with larger nuclear charge; therefore, it is interesting to compare the performance of CP- and QDPT-CASSCF for the heavy radicals.

To this end, we have evaluated the $g-$tensors using CP- and QDPT-CASSCF with the qrel-4 level. For CP-CASSCF, both CP-CI and CP-CAS calculations were performed. For QDPT-CASSCF, we have used two numbers of roots, 10 and 30, except for PdH, where only 10 roots were used. All calculated results are presented in Table 4.5 along with the experimental references. For comparison, the recent results from the single-reference 4c-CI calculations reported by Vad and coworkers [58] are also taken into account.

First of all, because the main contribution to the $\Delta g_\perp$ value of PdH is due to $1^2\Pi$ state characterized by ($d_{\mathrm{Pd}} \to \sigma$) excitation, it is known to be the difficult case for single-reference methods [52]. This statement is supported by the large overestimation of CCSD(T) calculation (454.1 ppt) carried out by Bolvin [54]. Also, the inclusion of the triples in CI treatment is necessary to obtain a comparable value as seen from Table 4.5. The perturbation-induced orbital relaxation slightly affects the $g-$values. Our CP- and QDPT-CASSCF $\Delta g_\perp$ values are quite close to each other and comparable to the

TABLE 4.5: Δg values (ppt) for hydride and dihydride using CP- and QDPT-CASSCF. The very recent 4c-CI results are also presented for comparison.

Radical	Δg	CP-CASSCF		QDPT-CASSCF		4c-CI[a]		expt[b]
		CP-CI	CP-CAS	10 states	30 states	CISD	CISDT	
PdH	$\Delta g_\parallel$	−0.2	−0.2	−17.3		−49.3	−25.0	−37.3
	$\Delta g_\perp$	248.9	247.8	256.7		480.8	325.0	290.6
CdH	$\Delta g_\parallel$	0.0	0.0	−1.0	−1.0	1.6	−1.6	−5.3
	$\Delta g_\perp$	−45.7	−43.0	−48.3	−48.3	−55.74	−56.1	−49.9
HgH	$\Delta g_\parallel$	−0.1	−0.1	−23.2	−23.6	−20.0	−21.7	−26.3
	$\Delta g_\perp$	−203.1	−182.4	−257.9	−264.2	−220.0	−232.0	−174.0
RhH$_2$	Δg_{xx}	12.7	12.1	−58.5	−62.8			−52.3
	Δg_{yy}	961.5	960.3	717.5	713.2			678.6
	Δg_{zz}	1077.9	1076.8	839.4	835.4			860.6
IrH$_2$	Δg_{xx}	21.0	21.2	−283.2	−326.2			−454.2
	Δg_{yy}	3629.9	3658.1	1433.7	1450.1			1712.6
	Δg_{zz}	3333.5	3359.5	1198.6	1188.8			661.6

[a] Ref. [58].
[b] Ref. [157] for hydrides and Ref. [140] for dihydrides.

experimental value. The relative error of QDPT-CASSCF result is 11.48 %. For the parallel component, our QDPT-CASSCF value is less negative than the values from 4c-CI calculations and experiment.

Although Cd is a transition metal atom, the d orbital do not contribute to the bonding description of CdH radical and the main contribution to the $\Delta g_\perp$ results from the first excited state $1^2\Pi$ characterized by $(\sigma \rightarrow \pi)$ excitation [52]. As seen from Table 4.5, the effect of the perturbation-induced orbital relaxation is small. The CP-CI $\Delta g_\perp$ value seems to be close to that of QDPT-CASSCF. The increasing number of roots in QDPT calculation does not change the $g−$values. Generally, all theoretical results agree well with the experimental values.

It is known that the electronic character of HgH is similar to that of CdH, the behavior of results for HgH is, however, more complicated. The $\Delta g_\perp$ is reduced by about 10.00 % under the perturbation-induced orbital relaxation, leading to good agreement with the experimental value (error of 4.83 %). Our QDPT-CASSCF provides the $\Delta g_\perp$ that is more negative in comparison with the experimental value. With increasing number of roots, the value slightly increases. This situation was also obtained by Ganyushin and Neese [57]. Those authors showed that the dynamical correlation can greatly improve upon the calculated value. On the other side, the $\Delta g_\parallel$ values from QDPT-CASSCF

calculations are less sensitive to the number of roots and seem to be consistent with the experimental value. In general, our QDPT-CASSCF results are fairly comparable with the 4c-CI results.
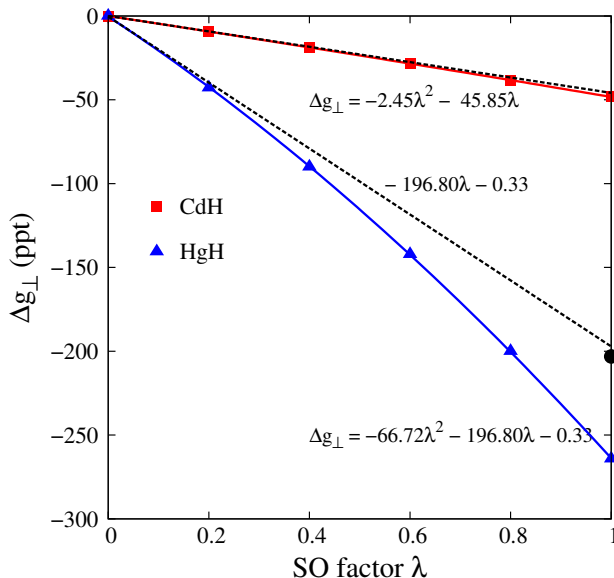
FIGURE 4.1: Dependence of $\Delta g_\perp$ component from QDPT-CASSCF calculations for CdH and HgH radicals on the SO-scaling factor λ. The black-dashed line indicates the second-order perturbation treatment, which includes only first-order SOC effects. The black circle dot indicates the $\Delta g_\perp$ value from CP-CI calculation.

Comparing the CP-CI and QDPT results, it is found that the higher-order SOC effects for CdH radical are negligible, while they become important for HgH radical. In order to clarify this statement, we employed the so-called SO-scaling analysis proposed by Malkin and coworkers [31]. In this analysis, the SO integrals are scaled by a factor λ such that $\lambda = 0$ corresponds to SR calculation, and $\lambda = 1$ correspond to full SO calculation. The dependence of $\Delta g_\perp$ for CdH and HgH on the SO-scaling factor λ is shown in Figure 4.1. The equations from the regression analyses are also provided. The plot for CdH, in which the linear prefactor is almost twenty times larger than the quadratic prefactor, is nearly linear. This explains why the result from the CP-CI calculation including only first-order SOC effects are quite consistent with that from QDPT calculation. Regarding the plot of HgH, the non-linear behavior is more pronounced. The quadratic prefactor is only three times smaller than the linear prefactor. The inclusion of higher-order SOC effects is thus necessary for the calculation of $\Delta g_\perp$ value of HgH. Note that the value obtained by neglecting the quadratic contribution at $\lambda = 1$ (-197.1 ppt) agrees very closely with the CP-CI value (-203.1 ppt), which is indicated by the black circle dot in Figure 4.1. This supports the reliability of QDPT value. Thus, the good agreement with the experimental value of CP-CAS value may be fortuitous.
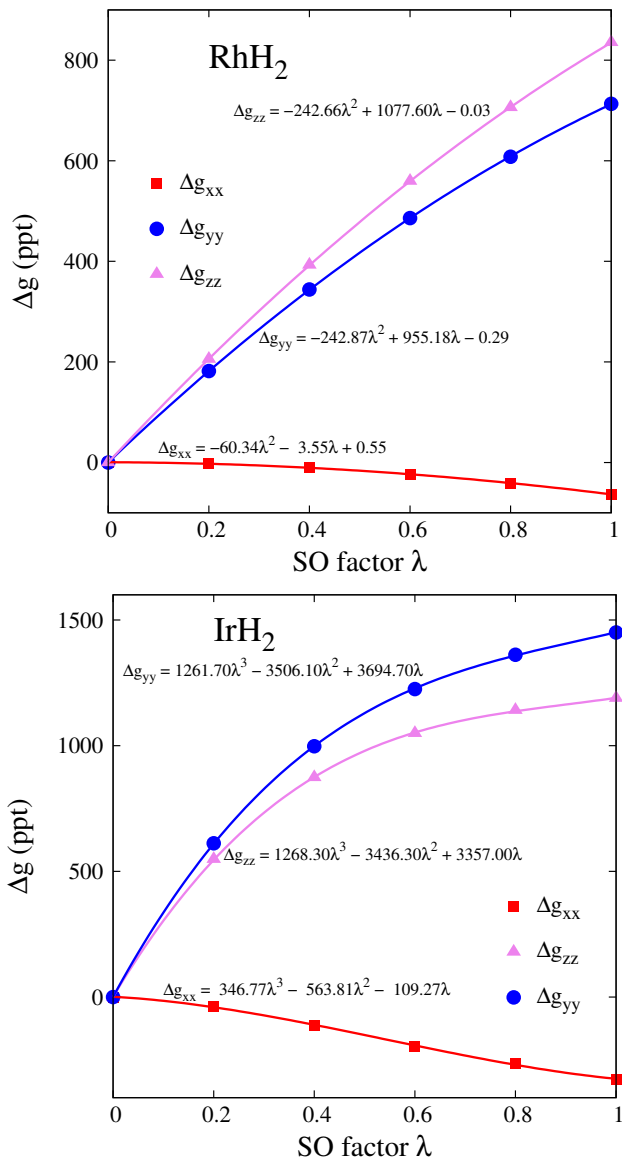
FIGURE 4.2: Dependence of $\Delta g-$values from QDPT-CASSCF calculations for RhH_2 (upper panel) and IrH_2 (lower panel) radicals on the SO-scaling factor λ.

We now discuss the results for RhH_2 and IrH_2. Generally, the perturbation-induced relaxation in CP-CASSCF insignificantly affects the CP-CI results. Increasing the number of roots only slightly changes the QDPT-CASSCF results. Difference between the results from CP- and QDPT-CASSCF calculations are quite large, especially for IrH_2, where the Δg_{yy} and Δg_{zz} components from the CP-CASSCF calculations are three times larger than those from QDPT-CASSCF.

For RhH_2, the CP-CASSCF calculations significantly overestimate the $g-$values, the QDPT-CASSCF results, on the contrary, agree well with the experimental values. The smallest and largest errors from the QDPT-CASSCF calculations with 30 roots are

2.86 % (for Δg_{zz} component) and 20.70 % (for Δg_{xx} component). For IrH$_2$, the CP-CASSCF results are clearly unacceptable. Reasonable agreement can be found for QDPT-CASSCF results. They are, however, still far from the experimental values. The largest error from QDPT-CASSCF calculation with 30 roots is up to 79.84 % (for Δg_{zz}). Similarly to the case of HgH, the dynamical correlation is expected to be necessary for the accuracy of the $g-$tensor calculation for IrH$_2$.

In order to investigate the large inconsistency between CP- and QDPT-CASSCF calculations, the $g-$values of RhH$_2$ and IrH$_2$ as functions of the SO-scaling factor λ are plotted in Figure 4.2. For RhH$_2$, the dependence of $g-$values on the SO-scaling factor displays the appreciable curvatures. The quadratic prefactor even clearly exceeds the linear one in the case of Δg_{xx}. For IrH$_2$, the regression analyses, which are insufficient at second-order, are up to third-order for the proper curve fitting. The most complicated behavior is also observed for the Δg_{xx} component, where the third-order perfactor is more than three times larger than the linear one. Generally, the linear term is insufficient to describe the behavior. Thus, the higher-order SOC effects are required for the accurate characterization of the $g-$tensors for these radicals.

Finally, it would be useful to provide the origin of the anisotropy of the $g-$tensors. To this end, we analyze the state contributions to the OZ part of the $g-$values. In this analysis, the OZ part is constructed by allowing the 1c ground state to interact only with the 1c excited state of interest. One has to bear in mind that the cross terms between the excited states are neglected; therefore, the total contribution is generally not the sum over the one-state contributions. The consistency can be obtained if the SOC effects are relatively weak and the contributions of the cross terms almost vanish.

The symmetry of RhH$_2$ and IrH$_2$ is C$_{2v}$, where the C$_2$ axis coincides with the $z-$axis. The ground state of these radicals was found to be $1^2 A_1$ [145, 152]. The $y-$component of the OZ part then results from the coupling of the ground state $^2 A_1$ *via* $\hat{L}_y$ with the excited states $^2 B_1$; whereas, the $z-$component originates from the coupling of the ground state $^2 A_1$ *via* $\hat{L}_z$ with the excited states $^2 A_2$. Table 4.6 presents the analysis of the most important contributions of excited states to $y-$ and $z-$components of the OZ part, $\Delta g_{yy}^{\text{OZ}}$ and $\Delta g_{zz}^{\text{OZ}}$. Obviously, two lowest excited states $1^2 B_1$ ($d_{xz} \rightarrow d_{x^2-y^2}$) and $1^2 A_2$ ($d_{xy} \rightarrow d_{x^2-y^2}$) dominate the $y-$ and $z-$components of the OZ part, respectively. There are also small contributions of the higher excited states. These contributions have the same order of magnitude but opposite signs; therefore, they cancel out each other.

TABLE 4.6: Analysis of the most important contributions (more than 5 ppt) to the OZ part of the g−values for RhH_2 and IrH_2. State symmetry and excitation energies $[cm^{-1}]$ are also reported.

Radical	State	ΔE	Δg_{yy}^{OZ}	Δg_{zz}^{OZ}
	1^2A_1			
	1^2A_2	5203	0.0	903.5
	1^2B_1	5790	799.4	0.0
RhH_2	2^2A_2	52888	0.0	6.0
	2^2B_1	52168	6.4	0.0
	4^2A_2	61090	0.0	−8.5
	4^2B_1	60684	−7.3	0.0
	1^2A_1			
	1^2A_2	4976	0.0	1566.6
	1^2B_1	4642	1745.3	0.0
IrH_2	2^2A_2	59871	0.0	21.6
	2^2B_1	60311	20.6	0.0
	4^2A_2	68924	0.0	−27.2
	4^2B_1	69092	−23.9	0.0

Perfomance of SO integral approximations

We now compare the performance of the following SO integral approximations: FNSSO, SNSO, and ENC. All calculations were carried out using QDPT-CASSCF with 10 roots for PdH and 30 roots for other molecules. The errors (in %) of calculated values relative to the experimental values are given in Figure 4.3. For diatomic radicals, only the errors of $\Delta g_\perp$ component are presented.

The relative errors of SNSO is seemingly close to those of FNSSO except for Δg_{xx} component of RhH_2, where the relative error of FNSSO (20.00 %) is almost two times smaller than that of SNSO (36.76 %). While FNSSO and SNSO provide negligible errors for $\Delta g_\perp$ of CdH, the error obtained from ENC is relatively big (33.27 %). Also, the ENC badly fails in the case of RhH_2, especially for Δg_{xx} component with an error up to 104.80 %. For HgH and IrH_2 radicals, the errors of ENC are comparable to those of FNSSO and SNSO.

In general, the trend is similar for all SO integrals. FNSSO performs best among three SO integral approximations considered herein. The ENC performs better for heavier radicals like HgH and RhH_2 than for lighter radicals like CdH and RhH_2. This is because the contribution of two-electron part of SOC is less important for heavier radicals.
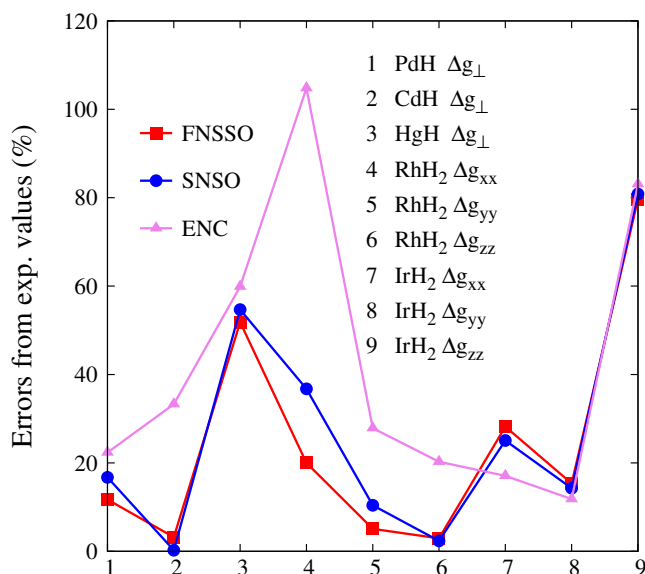
FIGURE 4.3: Errors (in percent) relative to the experimental values of QDPT-CASSCF results obtained with different SO integrals: FNSSO, SNSO, and ENC.

4.5 Conclusion

We have newly implemented the CP-CASSCF method, which is equivalent to an untruncated SOS expansion within the active space, for calculating molecular $g-$tensors. As the first step before employing the DMRG method, the FCI has been used to fully treat the correlation in active space. The perturbation-induced orbital relaxation was also taken into account. In the current implementation, only active-virtual rotation is considered, while the core-active rotation is neglected by introducing a frozen core approximation. In principle, the CP-CASSCF equation can be applied to any multiplicity. Our CP-CASSCF was tested to evaluate the $g-$values for a series of small light radicals, including both doublets and triplets. Our results are quite consistent with the MRCI results and comparable to the experimental values, especially for triplet radicals. The effect of the perturbation-induced orbital relaxation is generally small except for some light doublet radicals.

For comparison, the QDPT approach was also employed. For light radicals, the results obtained from CP-CASSCF and QDPT-CASSCF with sufficiently large number of roots are close to each other. This is because the SOC effects in these radicals are relatively weak. For PdH radical, which is known to be difficult for single-reference methods like 2c-CCSD(T) or 4c-CI, both CP- and QDPT-CASSCF provide results in good agreement with the experimental value. The inconsistency between CP- and QDPT-CASSCF results is pronounced for RhH_2 and IrH_2, where the higher-order SOC effects become important. The SO-scaling analysis was employed to understand the origin of the inconsistency.

In general, we have calculated the molecular g−tensors for several small molecules. Further comparisons need to be performed in order to reveal the advantages and disadvantages of these two approaches. Working on this issue is in progress.

Chapter 5

New approach to $g-$tensors using coupled-perturbed DMRG method: formulation

5.1 Overview of DMRG method

The DMRG algorithm consists of a set of sweeps over the k MOs assigned to an 1D quantum lattice of sites. At every step of the *one-dot* algorithm, the lattice is conceptually divided into three parts: a left block consisting of sites $1 \cdots i - 1$, a single dot consisting of site i, and a right block consisting of sites $i + 1 \cdots k$. The left and right blocks are each associated with M many-body states, denoted by $\{|l_{i-1}\rangle\}$, and $\{|r_i\rangle\}$, respectively. The single dot is associated with the complete Fock space of its respective orbital $\{|n_i\rangle\} = \{|\,\rangle, |\!\uparrow\rangle, |\!\downarrow\rangle, |\!\uparrow\downarrow\rangle\}$.

The DMRG wavefunction in terms of many-body quantum states reads

$$|\Psi\rangle = \sum_{l_{i-1}n_ir_i} c^{n_i}_{l_{i-1}r_i} |l_{i-1}n_ir_i\rangle, \tag{5.1}$$

where the left and right basis states, $\{|l_{i-1}\rangle\}$ and $\{|r_i\rangle\}$, are of the forms

$$|l_{i-1}\rangle = \sum_{n_1\cdots n_{i-1}} \mathbf{L}^{n_1}\cdots\mathbf{L}^{n_{i-1}} |n_1\cdots n_{i-1}\rangle, \tag{5.2}$$

$$|r_i\rangle = \sum_{n_{i+1}\cdots n_k} \mathbf{R}^{n_{i+1}}\cdots\mathbf{R}^{n_k} |n_{i+1}\cdots n_k\rangle. \tag{5.3}$$

Here, the $\mathbf{L}^n$ and $\mathbf{R}^n$ are the renormalization matrices, which satisfy the orthogonality conditions

$$\sum_n \mathbf{L}^{n+}\mathbf{L}^n = \mathbf{1}, \tag{5.4}$$

$$\sum_n \mathbf{R}^{n+}\mathbf{R}^n = \mathbf{1}. \tag{5.5}$$

The DMRG wavefunction (Eq. 5.1) can be rewritten in the matrix product state (MPS) ansatz, which is known as the canonical form of the DMRG wavefunction,

$$|\Psi\rangle = \sum_{n_1 \cdots n_k} \mathbf{L}^{n_1} \cdots \mathbf{L}^{n_{i-1}} \mathbf{C}^{n_i} \mathbf{R}^{n_{i+1}} \cdots \mathbf{R}^{n_k} |n_1 \cdots n_k\rangle, \tag{5.6}$$

where $\mathbf{C}^n$ is a coefficient matrix, which gives the expansion coefficients of wavefunction in superblock $\{l_{i-1}\}\{n_i\}\{r_i\}$. $|n_1 \cdots n_k\rangle$ denotes Slater determinant in an occupation number form; and n_i is the occupation number of orbital i.

The coefficient matrix $\mathbf{C}^n$ can be viewed as a flattened vector $\mathbf{c}$, which satisfies the normalization condition $\mathbf{cc}^+ = 1$. The DMRG wavefunction at each site is an eigenstate of the Schrödinger equation

$$\mathbf{Hc} = E\mathbf{c}, \tag{5.7}$$

where the Hamiltonian matrix elements in the superblock basis are written as

$$H^{l_{i-1}n_i r_i}_{l'_{i-1}n'_i r'_i} = \langle l_{i-1}n_i r_i | \hat{H} |l'_{i-1}n'_i r'_i \rangle \tag{5.8}$$

The key procedure of DMRG algorithm is the unique way of selecting the renormalized states. Once $\mathbf{c}$ is determined from Eq. 5.7, the density matrices of left and right block can be constructed,

$$\mathbf{D}_L = \mathrm{Tr}_R \left[\mathbf{C}^n \mathbf{C}^{n+} \right], \tag{5.9}$$

$$\mathbf{D}_R = \mathrm{Tr}_L \left[\mathbf{C}^{n+} \mathbf{C}^n \right]. \tag{5.10}$$

Let us define the eigenvector of left and right density matrices as $\mathbf{l}_\mu$ and $\mathbf{r}_\mu$, we have

$$\mathbf{D}_L \mathbf{l}_\mu = \mathbf{l}_\mu \sigma_\mu, \tag{5.11}$$

$$\mathbf{D}_R \mathbf{r}_\mu = \mathbf{r}_\mu \sigma_\mu. \tag{5.12}$$

The renormalization matrices $\mathbf{L}^n$ and $\mathbf{R}^n$ are then obtained from the M eigenvectors with largest weights ($\sigma_1 \geq \sigma_2 \geq \cdots \geq \sigma_M$). This procedure is termed decimation.

5.2   Analytical respone DMRG method for g−tensors

We recall the resultant formula of g−tensors derived from analytical response theory

$$g_{kl} = \frac{1}{\mu_B}\mathbf{D}^{(\alpha-\beta)}\frac{\partial^2\mathbf{h}^{SZ}}{\partial B_k \partial S_l} + \frac{1}{\mu_B}\frac{\partial\mathbf{D}^{(\alpha-\beta)}}{\partial B_k}\frac{\partial\mathbf{h}^{SO}}{\partial S_l}, \tag{5.13}$$

where $k, l = x, y, z$. See Section 4.2.2 for the meaning of notation. To obtain the second term, which is the cross term of OZ and SOC contributions, we need to evaluate the first derivative of the spin density with respect to magnetic field.

Hereafter, we will use the "first-order" instead of the "first derivative" for convenience. Also, the superscripts [0] and [1] will be used to denote the zeroth order and first order with respect to magnetic field, respectively.

We would like to note that in this Chapter, we only focus on the first-order CI part, which is obtained from analytical DMRG method, whereas the first-order MO part is the same as that described in Chapter 4.

5.2.1   First-order spin density

The spin density reads

$$D_{pq}^{(\alpha-\beta)} = \langle\Psi|\,\hat{E}_{pq}^{(-)}\,|\Psi\rangle, \tag{5.14}$$

where $\hat{E}_{pq}^{(-)} = \hat{a}_{p\alpha}^+\hat{a}_{q\alpha} - \hat{a}_{p\beta}^+\hat{a}_{q\beta}$ is the spin density operator; p, q are the spatial orbital labels; and $|\Psi\rangle$ is the DMRG wavefunction. The first-order spin density is then obtained as

$$D_{pq}^{(\alpha-\beta)[1]} = \left\langle\Psi^{[1]}|\hat{E}_{pq}^{(-)}|\Psi\right\rangle + \left\langle\Psi|\hat{E}_{pq}^{(-)}|\Psi^{[1]}\right\rangle. \tag{5.15}$$

The perturbation expansion of renormalization matrices $\mathbf{L}^n$ and $\mathbf{R}^n$, and coefficient matrix $\mathbf{C}^n$ are given by

$$\mathbf{L}^n = \mathbf{L}^{n[0]} + \mathbf{L}^{n[1]} + \cdots, \tag{5.16}$$

$$\mathbf{R}^n = \mathbf{R}^{n[0]} + \mathbf{R}^{n[1]} + \cdots, \tag{5.17}$$

$$\mathbf{C}^n = \mathbf{C}^{n[0]} + \mathbf{C}^{n[1]} + \cdots. \tag{5.18}$$

The first-order DMRG wavefunction (Eqs. 5.6) can be then explicitly written as follows

$$
\left| \Psi^{[1]} \right\rangle = \sum_{n_1 \cdots n_k} \{ \, \mathbf{L}^{n_1[1]} \cdots \mathbf{C}^{n_i[0]} \cdots \mathbf{R}^{n_k[0]} \; + \; \cdots
$$
$$
+ \, \mathbf{L}^{n_1[0]} \cdots \mathbf{C}^{n_i[1]} \cdots \mathbf{R}^{n_k[0]} \; + \; \cdots
$$
$$
+ \, \mathbf{L}^{n_1[0]} \cdots \mathbf{C}^{n_i[0]} \cdots \mathbf{R}^{n_k[1]} \} \left| n_1 \cdots n_k \right\rangle , \tag{5.19}
$$

where the zeroth-oder $\mathbf{L}^{n[0]}$, $\mathbf{R}^{n[0]}$, and $\mathbf{C}^{n[0]}$ are determined from unperturbed DMRG equation (Eq. 5.7).

Substituting Eq. 5.19 into Eq. 5.15, we obtain the first-order spin density

$$
D_{pq}^{(\alpha-\beta)[1]} = \mathbf{c}^{[1]+} \mathbf{E}_{pq}^{(-)} \mathbf{c}^{[0]} + \mathbf{c}^{[0]+} \mathbf{E}_{pq}^{(-)} \mathbf{c}^{[1]} + \mathbf{c}^{[0]+} \mathbf{E}_{pq}^{-[1]} \mathbf{c}^{[0]}, \tag{5.20}
$$

where $\mathbf{E}_{pq}^{(-)}$ is the spin density operator in the superblock basis, $\langle l_{i-1} n_i r_i | \, \hat{E}_{pq}^{(-)} \, | l'_{i-1} n'_i r'_i \rangle$. Note that there is the additional contribution $\mathbf{E}_{pq}^{-[1]}$. This is the first-order change in the spin density operator due to the first-order change in the renormalization matrices $\mathbf{L}^{n[1]}$ and $\mathbf{R}^{n[1]}$. This quantity is constructed in the similar way to the first-order change in Hamiltonian, which will be discussed later. Generally, to obtain the first-order DMRG spin density, the first-order renormalization and coefficient matrices $\mathbf{L}^{n[1]}$, $\mathbf{R}^{n[1]}$, and $\mathbf{C}^{n[1]}$ need to be evaluated.

5.2.2 First-order coefficient matrix

In the superblock basis, the external perturbation operator $\hat{V}$, which is the OZ operator in the case of $g−$tensors, is described by a matrix $\mathbf{V}$ with elements

$$
V_{l'_{i-1} n'_i r'_i}^{l_{i-1} n_i r_i} = \langle l_{i-1} n_i r_i | \, \hat{V} \, | l'_{i-1} n'_i r'_i \rangle , \tag{5.21}
$$

and molecular Hamiltonian is of the form

$$
\mathbf{H} = \mathbf{H}^{[0]} + \mathbf{V}, \tag{5.22}
$$

where $\mathbf{H}^{[0]}$ is the unperturbed BO Hamiltonian.

The first-order coefficient matrix can be obtained by solving the coupled-perturbed DMRG (CP-DMRG) equation, which is analogous to CP-CI equation described in Chapter 4. We can write down the perturbation expansion of DMRG equation (Eq. 5.7) for

each site

$$\left(\mathbf{H}^{[0]} + \mathbf{\Delta H}^{[1]} + \mathbf{V}^{[1]} + \cdots\right)\left(\mathbf{c}^{[0]} + \mathbf{c}^{[1]} + \cdots\right)$$
$$= \left(E^{[0]} + E^{[1]} + \cdots\right)\left(\mathbf{c}^{[0]} + \mathbf{c}^{[1]} + \cdots\right), \qquad (5.23)$$

where we have introduced the first-order change in Hamiltonian $\mathbf{\Delta H}^{[1]}$. This arises from the fact that Hamiltonian in the superblock basis depends on the renormalized matrices $\mathbf{L}^n$ and $\mathbf{R}^n$, so that the first-order change in these matrices leads to the change in the Hamiltonian.

In DMRG algorithm, the Hamiltonian is expressed as the matrix product of operators on the left, right, and single dot blocks. The general form of the Hamiltonian reads

$$\mathbf{H} = \mathbf{O}_L \cdot \mathbf{O}_R \cdot \mathbf{O}_\Delta, \qquad (5.24)$$

where operators $\mathbf{O}_L$, $\mathbf{O}_R$, and $\mathbf{O}_\Delta$ act on the left, right, and single dot blocks, respectively. The first-order change in Hamiltonian $\mathbf{\Delta H}^{[1]}$ is then obtained by

$$\mathbf{\Delta H}^{[1]} = \left(\mathbf{O}_L^{[1]} \cdot \mathbf{O}_R^{[0]} \cdot \mathbf{O}_\Delta + \mathbf{O}_L^{[0]} \cdot \mathbf{O}_R^{[1]} \cdot \mathbf{O}_\Delta\right). \qquad (5.25)$$

Note that the operator on the single dot ($\mathbf{O}_\Delta$) is unchanged during DMRG sweeping. The first-order operators are constructed through the blocking step similarly to the zeroth-order operators. The renormalization transformation for the first-order operator at a given block configuration in a left $\rightarrow$ right sweep is given by

$$R\left[\mathbf{O}_{L^*}^{[1]}\right] = \mathbf{L}^{n[0]}\mathbf{O}_{L^*}^{[1]}\mathbf{L}^{n[0]} + \mathbf{L}^{n[1]}\mathbf{O}_{L^*}^{[0]}\mathbf{L}^{n[0]} + \mathbf{L}^{n[0]}\mathbf{O}_{L^*}^{[0]}\mathbf{L}^{n[1]}, \qquad (5.26)$$

where the notation L^* means the extended left block, i.e. the left block plus the single dot. Analogous expressions holds for the right $\rightarrow$ left sweeps and operator $\mathbf{O}_R^{[1]}$.

For the molecular $g−$tensors, where the $\hat{V}^{[1]}$ is the angular momentum operator $\hat{L}$, the first-order energy $E^{[1]} = \left\langle\Psi^{[0]}\right|\hat{V}^{[1]}\left|\Psi^{[0]}\right\rangle$ is zero. This is because the interaction of an electronic state with itself through the angular momentum operator vanishes, i.e., it is forbidden by symmetry.

Finally, gathering the first-order term in Eq. 5.23 and enforcing the intermediate normalization through the projector $\mathbf{Q}_C = \mathbf{1} - \mathbf{c}^{[0]}\mathbf{c}^{[0]+}$, which ensures that $\mathbf{c}^{[1]+} \cdot \mathbf{c}^{[0]} = 0$, we obtain the first-order CP-DMRG equation as follows:

$$\left(\mathbf{H}^{[0]} - E^{[0]}\mathbf{1}\right)\mathbf{c}^{[1]} = -\mathbf{Q}_C\left(\mathbf{\Delta H}^{[1]} + \mathbf{V}^{[1]}\right)\mathbf{c}^{[0]}. \qquad (5.27)$$

5.2.3 First-order renormalization matrix

According to Dorando and coworkers [85], the first-order eigenvectors $\mathbf{l}_\mu$ and $\mathbf{r}_\mu$ of density matrices, which are used to construct the first-order renormalization matrices in the similar way to the zeroth-order renormalization matrices, are first obtained from response equations. In order to derive response equations for eigenvectors of density matrices, we write the eigenvalue equation for density matrices, i.e., Eqs. 5.11 and 5.12, in the perturbation expansion as follows

$$\left(\mathbf{D}_L^{[0]} + \mathbf{D}_L^{[1]} + \cdots\right)\left(\mathbf{l}_\mu^{[0]} + \mathbf{l}_\mu^{[1]} + \cdots\right) = \left(\mathbf{l}_\mu^{[0]} + \mathbf{l}_\mu^{[1]} + \cdots\right)\sigma_\mu, \tag{5.28}$$

$$\left(\mathbf{D}_R^{[0]} + \mathbf{D}_R^{[1]} + \cdots\right)\left(\mathbf{r}_\mu^{[0]} + \mathbf{r}_\mu^{[1]} + \cdots\right) = \left(\mathbf{r}_\mu^{[0]} + \mathbf{r}_\mu^{[1]} + \cdots\right)\sigma_\mu, \tag{5.29}$$

where the first-order density matrices $\mathbf{D}_L^{[1]}$ and $\mathbf{D}_R^{[1]}$ are given by

$$\mathbf{D}_L^{[1]} = \mathrm{Tr}_R\left[\mathbf{C}^{n[1]}\mathbf{C}^{n[0]+}\right] + \mathrm{Tr}_R\left[\mathbf{C}^{n[0]}\mathbf{C}^{n[1]+}\right], \tag{5.30}$$

$$\mathbf{D}_R^{[1]} = \mathrm{Tr}_L\left[\mathbf{C}^{n[1]+}\mathbf{C}^{n[0]}\right] + \mathrm{Tr}_L\left[\mathbf{C}^{n[0]+}\mathbf{C}^{n[1]}\right]. \tag{5.31}$$

We can set up response equation for eigenvectors of density matrices from Eqs. 5.28 and 5.29,

$$\left(\mathbf{D}_L^{[0]} - \sigma_\mu\mathbf{1}\right)\mathbf{l}_\mu^{[1]} = -\mathbf{Q}_L\mathbf{D}_L^{[1]}\mathbf{l}_\mu^{[0]}, \tag{5.32}$$

$$\left(\mathbf{D}_R^{[0]} - \sigma_\mu\mathbf{1}\right)\mathbf{r}_\mu^{[1]} = -\mathbf{Q}_R\mathbf{D}_R^{[1]}\mathbf{r}_\mu^{[0]}, \tag{5.33}$$

where the projectors $\mathbf{Q}_L$ and $\mathbf{Q}_L$ are defined similarly to $\mathbf{Q}_C$, i.e.,

$$\mathbf{Q}_L = \mathbf{1} - \sum_{\mu=1}^{M}\mathbf{l}_\mu^{[0]}\mathbf{l}_\mu^{[0]+}, \tag{5.34}$$

$$\mathbf{Q}_R = \mathbf{1} - \sum_{\mu=1}^{M}\mathbf{r}_\mu^{[0]}\mathbf{r}_\mu^{[0]+}. \tag{5.35}$$

The first-order eigenvectors of density matrices are obtained by using the explicit Rayleigh-Schrödinger expressions as follows

$$\mathbf{l}_\mu^{[1]} = -\sum_{\nu=M+1}\frac{\mathbf{l}_\nu^{[0]}\mathbf{D}_L^{[1]}\mathbf{l}_\mu^{[0]}}{\sigma_\nu^{[0]} - \sigma_\mu^{[0]}}\mathbf{l}_\nu^{[0]}, \tag{5.36}$$

$$\mathbf{r}_\mu^{[1]} = -\sum_{\nu=M+1}\frac{\mathbf{r}_\nu^{[0]}\mathbf{D}_R^{[1]}\mathbf{r}_\mu^{[0]}}{\sigma_\nu^{[0]} - \sigma_\mu^{[0]}}\mathbf{r}_\nu^{[0]}. \tag{5.37}$$

Nakatani and coworkers [158] have very recently proposed another approach to obtain

the first-order renormalization matrices, which are transformed directly from the first-order coefficient matrices. Reader is referred to Ref. [158] for the detailed formulation.

Once the first-order renormalization matrices $\mathbf{L}^{n[1]}$ and $\mathbf{R}^{n[1]}$ are obtained, the first-order change in Hamiltonian $\mathbf{\Delta H}^{[1]}$ (Eq. 5.25) and the first-order spin density operator $\mathbf{E}_{pq}^{[1]}$ can be computed.

5.3 Implementation

Supposing the standard DMRG calculation has been converged, the zeroth-order wavefunction $\mathbf{C}^{n[0]}$, zeroth-order renormalization matrices $\mathbf{L}^{n[0]}$ and $\mathbf{R}^{n[0]}$, and zeroth-order operators $\mathbf{O}_L^{[0]}$ and $\mathbf{O}_R^{[0]}$ were stored. Note that the perturbation operator $\mathbf{V}^{[1]}$ is constructed in the similar way to Hamiltonian operator in standard DMRG sweep. The full sweep algorithm to evaluate the first-order spin density is summarized as follows:

1. Set all $\mathbf{O}_L^{[1]}$, $\mathbf{O}_R^{[1]} = 0$.

2. Star a sweep left → right. At each block configuration:

   - Solve CP-DMRG equation (Eq. 5.27) with current $\mathbf{\Delta H}^{[1]}$ and $\mathbf{V}^{[1]}$.

   - Construct first-order renormalization matrices $\mathbf{L}^{n[1]}$ and $\mathbf{L}^{n[1]}$ from first-order eigenvectors of density matrices (Eqs. 5.36 and 5.37).

   - Update all $\mathbf{O}_L^{[1]}$ (Eq. 5.26) and construct first-order change in Hamiltonian $\mathbf{\Delta H}^{[1]}$ (Eq. 5.25).

   - Renormalize the perturbation $\mathbf{V}^{[1]}$ using zeroth-oder renormalization matrix $\mathbf{L}_n^{[0]}$.

   - Construct and store first-order spin operator $\mathbf{E}_{pq}^{-[1]}$.

3. Reverse the sweep right → left, analogous to the left → right sweep.

4. Loop to step 2 until convergence.

5. Evaluate the first-order spin density (Eq. 5.20) using converged $\mathbf{c}^{[1]}$ and $\mathbf{E}_{pq}^{-[1]}$.

Chapter 6

Correlated one-body potential from second-order Møller-Plesset perturbation theory: Alternative to orbital-optimized MP2 method

T. N. Lan, T. Yanai,

6.1   Introduction

The molecular orbitals (MOs) are a key concept in quantum chemistry to interpret the role of electrons in chemical bondings and reactions [159, 160]. They represent the behavior of one electron moving in the effective potential to which Coulomb interactions with many other electrons are averaged out. The effective mean field description is formulated in the Hartree-Fock (HF) theory as a result of using a single determinant as the model wave function in which electron correlation is dismissed in the solution of many-electron Schrödinger equation [161, 162]. In addition to the shapes of MOs, the orbital energies play a central role to characterize molecular electronic structures. The energy levels and associated canonical MOs are determined as eigenspectrum of the one-electron effective Hamiltonian or the so-called Fock operator that includes the mean field interaction potential. The density functional theory (DFT) calculations [163–167],

80

the workhorse approach of quantum chemistry, also heavily rely on the orbital picture for the analysis of bonding nature and fundamentally the formulation of the underlying Kohn-Sham (KS) theory[166].

The HF orbitals are in a general sense conveniently used as the optimal one-electron basis for post-mean-field calculations. However, their optimality as the basis is brought into question when they are applied to highly-correlated electronic systems, such as radicals and transition metal complexes [25, 103, 168–182]. The spin contamination is often observed in these systems. It significantly deteriorates the quality of the subsequent second-order Møller-Plesset perturbation (MP2) correction [183] which does not incorporate any orbital relaxation. The HF reference tends to make odd electrons or hole too delocalized because of neglecting electron correlation.

Various approaches to optimize orbitals in the presence of electron correlation have been developed to rectify the resultant correlated descriptions. Brueckner orbitals were introduced as a set of relaxed orbitals for which the single excitation coefficients are zero in the full configuration interaction (CI) expansion [184, 185]. The concept of Brueckner orbitals was incorporated into coupled-cluster (CC) theory and led to the algorithms called the Brueckner CC (BCC) theory [186–194]. They find the rotation of orbitals that makes single excitation amplitudes vanishing in the cluster expansion, virtually accounting for the singles contributions in an infinite order. As an alternative to BCC, the variational optimization of orbitals to minimize the CC energy has been investigated by several works and is known as the orbital-optimized CC (OCC) [195–205]. It may be appealing in the sense that the orbital response contribution can be removed to CC gradients [206].

The KS equation describes the quantum mechanism of non-interacting fictitious electrons moving in the KS potential which mainly involves dynamic electron correlation effects. The KS description is known to be less spin-contaminated [207–213] and yield chemically reasonable energy levels [214–217], relative to the uncorrelated HF counterparts. Also, the KS orbital energies has shown to be similar to quasi-particle band structure, and the band calculations with the exchange correlation potentials in the local density (LDA) or generalized gradient (GGA) approximations produce accurate valence bands [218, 219]. The interpretations of one-electron KS orbitals and energies for chemical applications have been presented by several works [214–217, 220–227]. The KS energies can be linked to the electron addition and removal energies by the many-body perturbation treatment with the GW approximation, which considers a system of quasi-particles associated with the non-local and energy(or frequency)-dependent self-energy [218, 228–232].

The self-energy operator in the Dyson equation of the propagator theory or the one-electron Green's function theory is the oldest realization of the correlated one-body

potential [233–236]. The Dyson equation accounts for relaxation and correlation effects, and its solutions occur when the frequencies ω, dependences of the self energy $\Sigma(\omega)$, correspond to electron binding energies. The associated Dyson orbitals are ampltides that help to measure the pole strength of an ionization. The complication of Dyson's theory, however, arises because of the built-in frequency dependence. The next step along this path was recently taken by Bartlett, showing $\Sigma(\omega)$ can be reduced to a frequency-independent yet non-local 'self-energy', which is provided from '*ab initio*' solutions of CC or MP theory [237–239]. In connection to KS theory, the optimized effective potential (OEP) method has been extensively studied to develop improved exchange-correlation potentials, which permit orbital dependence [240–246]. Also, the linking of the one-particle OEP functionals and many-body wave functions was investigated in the development of *ab initio* DFT methods by Bartlett *et al.*, deriving the local one-body correlation potential [247–249]. His recent work showed that there is little need for a post DFT GW if the local correlation potential is correctly described [238, 239].

Multiconfigurational self-consistent field (MCSCF) method is a widely-used model for treating static electron correlation, which is accounted for by the selected CI expansion of many-electron wave function, dealing with only chemically-related correlation space [250–253]. Multireference description is directly modeled by selection of correlated orbitals and electrons that are incorporated into the active correlation space. In the MCSCF calculations, the variational parameters of expansion for both CI and orbitals are optimized by energy minimization. The resulting orbitals are viewed as the mean-field representations of the statically-correlated wave function. Recently, the density matrix renormalization group method [254–257] is combined with the MCSCF approach, enabling to handle much larger-size active space than is possible with the traditional algorithm [258–261].

In the present work, we will explore an alternative approach to consider the orbital relaxation under the influence of dynamic correlation at the MP2 level. The efficient implementation of the orbital-optimized MP2 (OO-MP2) method has recently been studied by several groups [25, 103, 168–175]. Head-Gordon *et al.* developed the OO-MP2 approach in conjunction with the scaled opposite-spin treatment [262], which offers a radical computational saving [168–171]. It demands only fourth-order cost while involves an empirical factor for the scaled opposite-spin approximation to the MP2 energy. The resolution-of-identity (RI) approximation to the required Coulomb integrals also enhances the efficiency. The OO-MP2 with the RI approximation was implemented by Neese *et al.* as an algorithm that minimizes Hylleraas functional with respect to orbital rotations [25, 103, 172]. Improvement in accuracy at the cost of OO-MP2 was achieved by its combination with spin-component scaling treatment [263]. The optimized orbitals were shown to offer improved performance of MP2 for open-shell systems, especially

in the prediction of molecular hyperfine coupling constants [25, 103]. Bozkaya *et al.* reported a Lagrangian-based approach to the second- and third-order OO-MP methods, introducing the formulation based on the minimization of the MP2 or MP3 Λ-functionals [173–175].

In our approach, a correlated one-body (Fock-like) Hamiltonian of the MP2 theory is derived through the canonical transformation theory (CT), which has been developed by one of the authors and his coworkers [264–271]. In the CT approach, the dynamic correlation is described by a similarity transformation of the molecular Hamiltonian $\hat{H}$ using an unitary operator $e^{\hat{A}}$ with the anti-Hermitian excited operator $\hat{A} = -\hat{A}^\dagger$:

$$\hat{\bar{H}} = e^{\hat{A}^\dagger} \hat{H} e^{\hat{A}} \,. \tag{6.1}$$

The CT is closely related to Kutzelnigg and Mukherjee's general unitary transformation methods [272–274]. In this study, the cluster operator $\hat{A}$ is modeled with the use of the double-substitution amplitudes of the MP1 wave function, whose analytic form is given in canonical orbital basis. The mean-field approximation to $\hat{\bar{H}}$ [Eq. (6.1)] is introduced, which systematically reduces high-rank operators into one-body ones. Optimized orbitals are then obtained as eigenfunctions of the Schrödinger equation of the one-body MP2 Hamiltonian. A key feature in our theory is that orbital energies are also optimized, arising in a natural form as associated eigenvalues. Using these correlated orbitals and orbital energies in the canonical orbital representation, we repeat the evaluation of the MP1 amplitudes, subsequently updating the correlated one-body descriptions. The orbital optimization is achieved in the light of finding a self-consistent field instead of energy minimization. Related to this study, we previously reported the approach that uses the F12 transcorrelation factor [275–278] for $\hat{A}$, achieving a general two-body form of the explicitly-correlated effective Hamiltonian [279].

The chapter is organized as follows. We will give the detail of our theory in Section 6.2. The numerical performance will be shown in Section 6.3. The present study focuses on only closed-shell systems. Finally, we summarize our study in the Section 6.4.

6.2 Theory

6.2.1 Mean-field (one-body) approximation

A central physical technique exploited in our approach is a systematic way of reducing high-rank many-body operators into an effective one-body form. Let us begin by introducing the mean-field (MF) or one-body approximation to general-rank operators.

Given that a many-body operator is expanded into a sum of normal-ordered operators on the basis of Wick's theorem, the MF approximation to it is obtained by neglecting the two-rank normal-ordered operators or higher. For example, two-body and three-body operators in the orthonormal spin-orbital basis, labeled by $\{p, q, r, s, t, u\}$, are written in the MF form as,

$$\hat{a}_{qs}^{pr} \overset{\mathrm{MF}}{\Longrightarrow} \gamma_q^p \hat{a}_s^r + \gamma_s^r \hat{a}_q^p - \gamma_s^p \hat{a}_q^r - \gamma_q^r \hat{a}_s^p - \gamma_q^p \gamma_s^r + \gamma_s^p \gamma_q^r \tag{6.2}$$

$$\begin{aligned}
\hat{a}_{qsu}^{prt} \overset{\mathrm{MF}}{\Longrightarrow} &\left(\gamma_s^r \gamma_u^t - \gamma_u^r \gamma_s^t\right) \hat{a}_q^p \; - \left(\gamma_q^r \gamma_u^t - \gamma_u^r \gamma_q^t\right) \hat{a}_s^p \; - \left(\gamma_s^r \gamma_q^t - \gamma_q^r \gamma_s^t\right) \hat{a}_u^p \\
&+ \left(\gamma_q^p \gamma_u^t - \gamma_u^p \gamma_q^t\right) \hat{a}_s^r \; - \left(\gamma_s^p \gamma_u^t - \gamma_u^p \gamma_s^t\right) \hat{a}_q^r \; - \left(\gamma_q^p \gamma_s^t - \gamma_s^p \gamma_q^t\right) \hat{a}_u^r \\
&+ \left(\gamma_q^p \gamma_s^r - \gamma_s^p \gamma_q^r\right) \hat{a}_u^t \; - \left(\gamma_u^p \gamma_s^r - \gamma_s^p \gamma_u^r\right) \hat{a}_q^t \; - \left(\gamma_q^p \gamma_u^r - \gamma_u^p \gamma_q^r\right) \hat{a}_s^t \\
&- 2\left(\gamma_q^p \gamma_s^r \gamma_u^t \; - \gamma_s^p \gamma_q^r \gamma_u^t \; - \gamma_u^p \gamma_s^r \gamma_q^t \; - \gamma_q^p \gamma_u^r \gamma_s^t \; + \gamma_s^p \gamma_u^r \gamma_q^t \; + \gamma_u^p \gamma_q^r \gamma_s^t\right)
\end{aligned} \tag{6.3}$$

where $\hat{a}_q^p$, $\hat{a}_{qs}^{pr}$, and $\hat{a}_{qsu}^{prt}$ are the one-, two-, and three-body second-quantized operators, respectively: $\hat{a}_q^p = \hat{a}_p^\dagger \hat{a}_q$, $\hat{a}_{qs}^{pr} = \hat{a}_p^\dagger \hat{a}_r^\dagger \hat{a}_s \hat{a}_q$, $\hat{a}_{qsu}^{prt} = \hat{a}_p^\dagger \hat{a}_r^\dagger \hat{a}_t^\dagger \hat{a}_u \hat{a}_s \hat{a}_q$. The constant γ_q^p is an element of the reduced one-body density matrix, given by

$$\gamma_q^p = \langle \Psi_0 | \, \hat{a}_q^p \, | \Psi_0 \rangle . \tag{6.4}$$

In this study, we consider the reference Ψ_0 to be a single Slater determinant. The density matrix elements are then diagonal and those elements γ_p^p correspond to the occupancy (0 or 1). The multireference generalization was investigated by Kutzelnigg and Mukherjee [280, 281].

We hereafter use the following notation for indices: $\{p, q, r, \ldots\}$ refer to general spinless orbitals, $\{i, j, k, \ldots\}$ to occupied spinless orbitals, $\{a, b, c, \ldots\}$ to virtual spinless orbitals, and $\{\sigma, \tau, \lambda\}$ to spin indices. Einstein's convention is used to present the summations over repeated indices.

The spin-free analogue of Eqs. (6.2) and (6.3) is written as

$$\hat{E}_{qs}^{pr} \overset{\mathrm{MF}}{\Longrightarrow} D_q^p \hat{E}_s^r + D_s^r \hat{E}_q^p - \tfrac{1}{2} D_s^p \hat{E}_q^r - \tfrac{1}{2} D_q^r \hat{E}_s^p \; - D_q^p D_s^r + \tfrac{1}{2} D_s^p D_q^r \tag{6.5}$$

$$\begin{aligned}
\hat{E}_{qsu}^{prt} \overset{\mathrm{MF}}{\Longrightarrow} &\left(D_s^r D_u^t - \tfrac{1}{2} D_u^r D_s^t\right) \hat{E}_q^p \; - \tfrac{1}{2}\left(D_q^r D_u^t - \tfrac{1}{2} D_u^r D_q^t\right) \hat{E}_s^p \; - \tfrac{1}{2}\left(D_s^r D_q^t - \tfrac{1}{2} D_q^r D_s^t\right) \hat{E}_u^p \\
&+ \left(D_q^p D_u^t - \tfrac{1}{2} D_u^p D_q^t\right) \hat{E}_s^r \; - \tfrac{1}{2}\left(D_s^p D_u^t - \tfrac{1}{2} D_u^p D_s^t\right) \hat{E}_q^r \; - \tfrac{1}{2}\left(D_q^p D_s^t - \tfrac{1}{2} D_s^p D_q^t\right) \hat{E}_u^r \\
&+ \left(D_q^p D_s^r - \tfrac{1}{2} D_s^p D_q^r\right) \hat{E}_u^t \; - \tfrac{1}{2}\left(D_u^p D_s^r - \tfrac{1}{2} D_s^p D_u^r\right) \hat{E}_q^t \; - \tfrac{1}{2}\left(D_q^p D_u^r - \tfrac{1}{2} D_u^p D_q^r\right) \hat{E}_s^t \\
&- 2 D_q^p D_s^r D_u^t \; + \left(D_s^p D_q^r D_u^t + D_u^p D_s^r D_q^t + D_q^p D_u^r D_s^t\right) \; - \tfrac{1}{2}\left(D_s^p D_u^r D_q^t + D_u^p D_q^r D_s^t\right)
\end{aligned} \tag{6.6}$$

where the one-, two-, and three-body spin-free excitation operators $\hat{E}_q^p$, $\hat{E}_{qs}^{pr}$ and $\hat{E}_{qsu}^{prt}$ are defined by $\hat{E}_q^p = \hat{a}_{p\sigma}^\dagger \hat{a}_{q\sigma}$, $\hat{E}_{qs}^{pr} = \hat{a}_{p\sigma}^\dagger \hat{a}_{r\tau}^\dagger \hat{a}_{s\tau} \hat{a}_{q\sigma}$, and $\hat{E}_{qsu}^{prt} = \hat{a}_{p\sigma}^\dagger \hat{a}_{r\tau}^\dagger \hat{a}_{t\lambda}^\dagger \hat{a}_{u\lambda} \hat{a}_{s\tau} \hat{a}_{q\sigma}$, and

the spin-free one-body density matrix is given by

$$D_q^p = \langle \Psi_0 | \, \hat{E}_q^p \, | \Psi_0 \rangle = \gamma_{q\alpha}^{p\alpha} + \gamma_{q\beta}^{p\beta} \tag{6.7}$$

Hereafter, all formulas will be written in the spin-free form.

Given the molecular Hamiltonian:

$$\hat{H} = h_q^p \hat{E}_p^q + \tfrac{1}{2} g_{qs}^{pr} \hat{E}_{pr}^{qs} \tag{6.8}$$

where h_q^p and g_{qs}^{pr} are one- and two-electron integrals, respectively, it is well-known that the HF approximation can be simply derived by inserting the MF form of $\hat{E}_{pr}^{qs}$ [Eq. (6.5)] to $\hat{H}$ [Eq. (6.8)]. This leads to the one-body Hamiltonian given as

$$\hat{H} \overset{\mathrm{MF}}{\Longrightarrow} \ \hat{H}_{\mathrm{HF}} = \ C + \hat{F} \tag{6.9}$$

with the Fock operator $\hat{F} = f_q^p \hat{E}_p^q$, where f_q^p and C are the Fock matrix and a constant, respectively:

$$f_q^p = h_q^p + 2g_{qi}^{pi} - g_{iq}^{pi}, \tag{6.10}$$

$$C = -2g_{ij}^{ij} + g_{ji}^{ij}. \tag{6.11}$$

The expectation value $\langle \hat{H}_{\mathrm{HF}} \rangle$ certainly gives an expression of the HF energy.

6.2.2   One-body MP2 Hamiltonian

We now proceed to the introduction of the correlated one-body effective Hamiltonian. In this study, the dynamic correlation at the MP2 level of theory is incorporated into the Hamiltonian. On the basis of the CT theory [264–271], the reduction of the MP2 theory to the one-body description is formulated by modeling the one-body MP2 (OB-MP2) Hamiltonian as:

$$\hat{H}_{\mathrm{OB\text{-}MP2}} = \hat{H}_{\mathrm{HF}} + \left[\hat{H}, \hat{A}_{\mathrm{MP1}} \right]_1 + \tfrac{1}{2} \left[\left[\hat{F}, \hat{A}_{\mathrm{MP1}} \right], \hat{A}_{\mathrm{MP1}} \right]_1, \tag{6.12}$$

where $[\ldots]_1$ denotes that the commutator involving high-rank operators is replaced by its MF approximation [Eqs. (6.5) and (6.6)] in terms of one-body operators and constants only. The amplitude $\hat{A}_{\mathrm{MP1}}$ is the anti-Hermitian doubly-excited operator given in the canonical orbital basis as:

$$\hat{A}_{\mathrm{MP1}} = \tfrac{1}{2} T_{ij}^{ab} (\hat{E}_{ij}^{ab} - \hat{E}_{ab}^{ij}), \tag{6.13}$$

with the spin-free form of the MP1 amplitude

$$T_{ij}^{ab} = \frac{g_{ij}^{ab}}{\epsilon_i + \epsilon_j - \epsilon_a - \epsilon_b} \, . \tag{6.14}$$

where ϵ_i is the orbital energy of the canonical orbital i. The OB-MP2 Hamiltonian [Eq. (6.12)] is derived by truncating the Baker-Campbell-Hausdorff expansion of the CT Hamiltonian [Eq. (6.1)] and is correct through the second order in perturbation. Also note that it bears some resemblance to the second-order Hylleraas functional.

Let us write the OB-MP2 Hamiltonian as

$$\hat{H}_{\text{OB-MP2}} = \hat{H}_{\text{HF}} + \hat{V}_{\text{OB-MP2}} \tag{6.15}$$

where $\hat{V}_{\text{OB-MP2}}$ is the perturbative one-body potential associated with MP2 electron correlation and takes the following general one-body form as

$$\hat{V}_{\text{OB-MP2}} = C' + \hat{V} \tag{6.16}$$

with $\hat{V} = v_q^p \hat{E}_p^q$. The working tensor contraction expressions for the evaluation of $\hat{V}$ and C' are given as follows:

$$\begin{aligned}
\hat{V} = {}& 2\overline{T}_{ij}^{ab} \left[f_a^i \, \hat{\Omega}\left(\hat{E}_j^b \right) + \nu_{ab}^{ip} \, \hat{\Omega}\left(\hat{E}_j^p \right) - \nu_{ij}^{aq} \, \hat{\Omega}\left(\hat{E}_q^b \right) \right] + 2 f_a^i \overline{T}_{ij}^{ab} \overline{T}_{jk}^{bc} \, \hat{\Omega}\left(\hat{E}_c^k \right) \\
& + f_c^a T_{ij}^{ab} \overline{T}_{il}^{cb} \, \hat{\Omega}\left(\hat{E}_j^l \right) + f_c^a T_{ij}^{ab} \overline{T}_{kj}^{cb} \, \hat{\Omega}\left(\hat{E}_i^k \right) \\
& - f_i^k T_{ij}^{ab} \overline{T}_{kl}^{ab} \, \hat{\Omega}\left(\hat{E}_l^j \right) - f_i^p T_{ij}^{ab} \overline{T}_{kj}^{ab} \, \hat{\Omega}\left(\hat{E}_k^p \right) \\
& + f_i^k T_{ij}^{ab} \overline{T}_{kj}^{ad} \, \hat{\Omega}\left(\hat{E}_b^d \right) + f_k^i T_{ij}^{ab} \overline{T}_{kj}^{cb} \, \hat{\Omega}\left(\hat{E}_a^c \right) \\
& - f_c^a T_{ij}^{ab} \overline{T}_{ij}^{cd} \, \hat{\Omega}\left(\hat{E}_d^b \right) - f_p^a T_{ij}^{ab} \overline{T}_{ij}^{cb} \, \hat{\Omega}\left(\hat{E}_c^p \right) \, ,
\end{aligned} \tag{6.17}$$

and

$$C' = -4\overline{T}_{ij}^{ab} \nu_{ab}^{ij} + 4 f_i^k T_{ij}^{ab} \overline{T}_{kj}^{ab} - 4 f_a^c T_{ij}^{ab} \overline{T}_{ij}^{cb} , \tag{6.18}$$

where $\overline{T}_{ij}^{ab} = T_{ij}^{ab} - \frac{1}{2} T_{ji}^{ab}$ and the symmetrization operator $\hat{\Omega}\left(\hat{E}_q^p \right) = \hat{E}_q^p + \hat{E}_p^q$. At the end, we rewrite $\hat{H}_{\text{OB-MP2}}$ [Eqs. (6.12) and (6.15)] in a similar form to Eq. (6.9) (for $\hat{H}_{\text{HF}}$) as follows:

$$\hat{H}_{\text{OB-MP2}} = \bar{C} + \hat{\bar{F}} \tag{6.19}$$

with $\hat{\bar{F}} = \bar{f}_q^p \hat{E}_p^q$. The elements $\bar{f}_q^p$ and $\bar{C}$ are *perturbed* analogues of the Fock matrix f_q^p [Eq. (6.10)] and C [Eq. (6.11)] of the HF theory and are given as

$$\bar{f}_q^p = f_q^p + v_q^p, \quad \bar{C} = C + C'. \tag{6.20}$$

This indicates that the perturbation matrix v_q^p serves as the correlation potential, which additively alters the uncorrelated HF picture, and the central energy operator is replaced by the *correlated* Fock operator $\hat{\bar{F}}$. The MO coefficients and energies can be redetermined by the matrix diagonalization of $\bar{f}_q^p$, which gives rise to orbital relaxation in the presence of dynamic correlation effects. Note that $\langle \Psi_0 | \hat{H}_{\text{OB-MP2}} | \Psi_0 \rangle$ is identical to the MP2 energy when using the HF wave function (with the HF orbitals) for Ψ_0.

6.2.3 Implementation

In our approach, the fully relaxed orbitals are obtained by repeatedly diagonalizing the correlated Fock matrix $\bar{f}_q^p$ [Eq. (6.20)] until the self-consistency or equivalently the Brillouin condition ($\bar{f}_a^i = 0$) is satisfied. A sketch of our implementation is as follows:

1. Set up starting canonical MOs ψ_p and orbital energies ϵ_p, which may be guessed from HF or KS calculations.

2. Transform one- and two-electron integrals from atomic orbital (AO) basis to MO basis.

3. Evaluate the MP1 amplitude T_{ij}^{ab} [Eq. (6.14)] followed by $\bar{f}_q^p$ and $\bar{C}$ [Eqs. (6.20)]. The total electronic energy is given by $E_{\text{elec}} = 2\bar{f}_i^i + \bar{C}$.

4. Diagonalize the correlated Fock matrix $\bar{f}_q^p$. The transformation matrix U_{pq} and the updated orbital energies ϵ_p are obtained as eigenvectors and eigenvalues, respectively.

5. Update MOs by the linear transformation: $\psi_p \leftarrow \sum_{pq} U_{pq} \psi_q$. The new orbitals associated with the $N_{\text{elec}}/2$ lowest eigenvalues are treated as occupied orbital states.

6. Repeat the steps 2-5 until convergence.

Note that the denominator of the MP1 amplitude [Eq. (6.14)] is altered by the updated orbital energies in our approach, whereas it is fixed with use of the HF orbital energies in the previous OO-MP2 implementations. The computational cost of each iteration scales as $O(N^5)$, which is the same scaling as the ordinal MP2 calculation including the four-index integral transformation. It might be interesting to explore a possibility to

construct the correlated Fock matrix in AO basis using the AO integral driven algorithm in a similar fashion to the direct SCF method.

6.3 Results and discussions

In this paper, unless otherwise noted, all the geometries were optimized by the DFT using the B3LYP functional [282] with aug-cc-pVDZ basis sets [283–287]. The DFT, HF, MP2, and CC singles, doubles, and perturbative triples (CCSD(T)) [288] calculations with the restricted closed-shell treatment were performed using the GAUSSIAN 09 program package [102]. The OO-MP2 calculations with the Resolution-of-Identity approximation (OO-RI-MP2) [25, 103, 172] were carried out with the ORCA program package[99] (version 2.8). The frozen-core approximation was used for all the MP2, OO-RI-MP2, OB-MP2, and CCSD(T) calculations.

6.3.1 Reaction energies

We first assessed the performance of the OB-MP2 method for thermochemical applications, having 25 reactions of the second-row element molecules (Table 6.1) as a benchmark set. In this benchmark, the accuracy of the OB-MP2 prediction of reaction energies is examined by comparing it with those measured for the MP2 and OO-RI-MP2 calculations. The reference data were calculated at the CCSD(T) level. Two levels of the basis sets cc-pVDZ and cc-pVTZ [283, 283–287] were tested.

Figure 6.1 shows the deviations of the reaction energies of MP2, OO-RI-MP2, and OB-MP2 from the CCSD(T) counterparts. The errors of MP2, OO-RI-MP2, and OB-MP2 are of the same sign in most cases. The statistical errors are summarized in Table 6.2. The mean absolute deviation (MAD) values of OB-MP2 are marginally smaller than those of MP2 and OO-RI-MP2 by 0.5 and 0.2 mE_h, respectively, for cc-pVDZ and by 0.5 and 0.6 mE_h, respectively, for cc-pVTZ.

For a further test, we combine the the F12 explicit correlation[275–278] with the OB-MP2 method through the canonical transcorrelated Hamiltonian, which was recently derived by Yanai and Shiozaki.[279] The aug-cc-pVXZ/OptRI (X=D and T) basis sets[289] were used for the complementary auxiliary orbital basis (CABS) space[290] in the F12 treatment. Figure 6.2 shows the errors of the reaction energies obtained by OB-MP2 with F12 (termed OB-MP2-F12) relative to the reference CCSD(T)/cc-pVQZ data. As shown in Table 6.3, the root mean square (RMS) drops from 8.2 to 5.9 mE_h with the increasing level of basis sets from cc-pVDZ to cc-pVTZ. With the cc-pVDZ basis, the

TABLE 6.1: Benchmark set of 25 reactions.

No.	Reaction
1	$H_2 + F_2 \rightarrow 2HF$
2	$F_2O + H_2 \rightarrow F_2 + H_2O$
3	$H_2 + H_2O_2 \rightarrow 2H_2O$
4	$H_2 + C_2H_2 \rightarrow C_2H_4$
5	$HCN + NH_3 \rightarrow N_2 + H_2O$
6	$CO + H_2O \rightarrow CO_2 + H_2$
7	$N_2O + H_2 \rightarrow N_2 + H_2O$
8	$CO + H_2 \rightarrow CH_4 + H_2O$
9	$CO + H_2 \rightarrow CH_2O$
10	$2H_2 + O_2 \rightarrow 2H_2O$
11	$C_2H_4 \rightarrow C_2H_2$
12	$CH_4 + O_2 \rightarrow CO + H_2 + H_2O$
13	$CH_4 + F_2 \rightarrow CH_3F + HF$
14	$CH_4 + O_2 \rightarrow CH_3Cl + HCl$
15	$H_2 + O_2 \rightarrow H_2O$
16	$2H_2O_2 \rightarrow 2H_2O + O_2$
17	$N_2 + 3\,H_2 \rightarrow 2NH_3$
18	$CH_2{=}C \rightarrow C_2H_2$
19	$H_2 + Cl_2 \rightarrow 2HCl$
20	$HCN + H_2O \rightarrow CO + NH_3$
21	$CO + NH_3 \rightarrow HCN + H_2O$
22	$C_2H_2 + HF \rightarrow C_2H_3F$
23	$C_2H_2 + HCl \rightarrow C_2H_3Cl$
24	$CH_4 + O_2 \rightarrow CH_3OH$
25	$CO + H_2 \rightarrow CH_3OH$

F12 treatment had a certain impact on the reduction of basis set errors, with the MADs of 10.6 and 6.2 mE_h for OB-MP2 and OB-MP2-F12, respectively. The MADs of OB-MP2/cc-pVTZ with and without the F12 correction resulted in a more or less similar value: 4.2 and 4.1 E_h, respectively. This indicates that the basis set description is nearly convergent at the cc-pVTZ level. The MADs of OB-MP2-F12 with the cc-pVDZ and cc-pVTZ basis sets are comparable to those of MP2 and OO-RI-MP2 with the cc-pVQZ basis sets.

Overall, the improvement upon the MP2 reaction energies from the orbital optimization in the OB-MP2 and OO-RI-MP2 methods was not of great significance. This indicates that the influence of orbital relaxation seems to be negligible on reaction energies for the
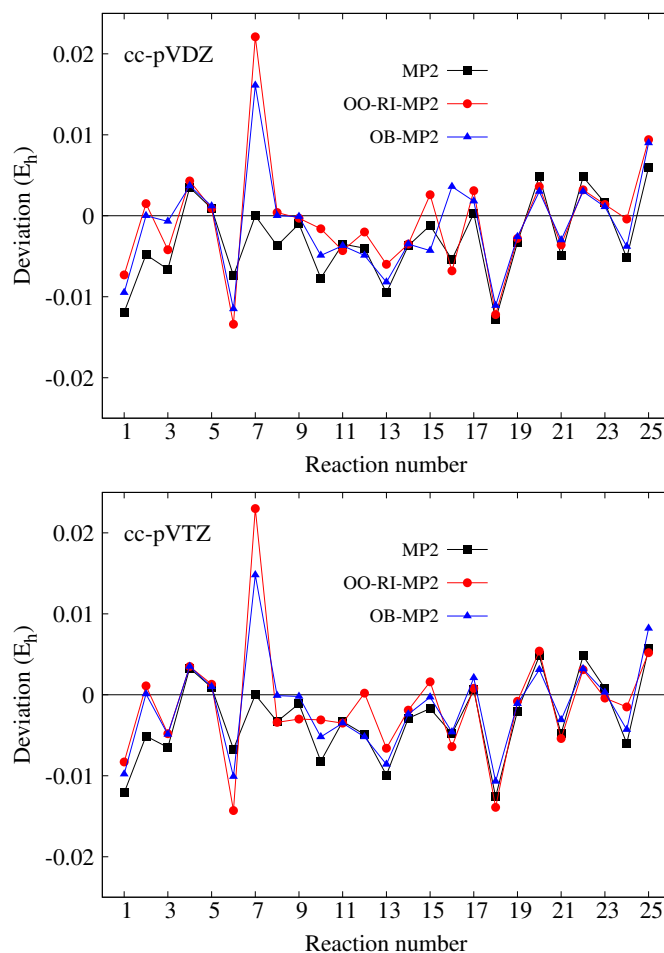
FIGURE 6.1: Deviations of the reaction energies of the MP2, OO-RI-MP2, and OB-MP2 methods with the cc-pVDZ (upper panel) and cc-pVTZ (lower panel) basis sets from the CCSD(T) reference data.
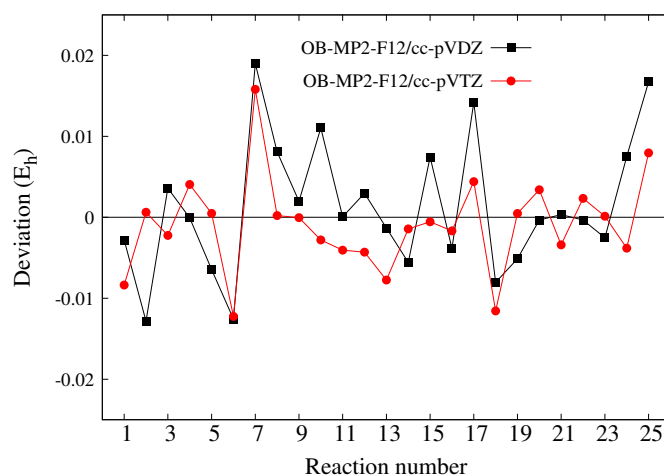
FIGURE 6.2: Errors of the reaction energies of the OB-MP2-F12 method with the cc-pVDZ and cc-pVTZ basis sets in comparison with the CCSD(T)/cc-pVQZ values.

test systems consisting of the closed-shell main group molecules. A similar observation was also reported by Neese *et al.* [172] in the previous assessment of the OO-RI-MP2.

TABLE 6.2: Statistical deviations of MP2, OO-RI-MP2 and OB-MP2 reaction energies from CCSD(T) reference data with the cc-pVDZ and cc-pVTZ basis sets. Maximum absolute deviation (MAX), difference between maximum and minimum absolute deviations ($\Delta_{\text{Max-Min}}$), root mean square (RMS), and mean absolute deviation (MAD) are shown in E_h.

	MP2	OO-RI-MP2	OB-MP2
cc-pVDZ			
$\Delta_{\text{Max-Min}}$	0.0125	0.0218	0.0161
MAX	0.0128	0.0221	0.0161
RMS	0.0060	0.0069	0.0061
MAD	0.0051	0.0048	0.0046
cc-pVTZ			
$\Delta_{\text{Max-Min}}$	0.0120	0.0228	0.0147
MAX	0.0126	0.0230	0.0148
RMS	0.0059	0.0071	0.0059
MAD	0.0050	0.0049	0.0044

TABLE 6.3: Statistical performance (in E_h) against the reaction energies calculated with CCSD(T)/cc-pVQZ for the reaction set in Table I.

	MP2	OO-RI-MP2	OB-MP2	OB-MP2	OB-MP2-F12	OB-MP2-F12
(basis sets)	(cc-pVQZ)	(cc-pVQZ)	(cc-pVDZ)	(cc-pVTZ)	(cc-pVDZ)	(cc-pVTZ)
$\Delta_{\text{Max-Min}}$	0.0120	0.0202	0.0333	0.0169	0.0189	0.0158
MAX	0.0126	0.0209	0.0342	0.0169	0.0190	0.0158
RMS	0.0060	0.0066	0.0063	0.0058	0.0082	0.0059
MAD	0.0051	0.0047	0.0106	0.0041	0.0062	0.0042

6.3.2 Ionization potentials and electron affinities

The Koopmans' theorem states that in the closed-shell Hartree-Fock theory, the ionization potential (IP) and the electron affinity (EA) are equal to the negatives of the highest occupied molecular orbital (HOMO) and lowest unoccupied molecular orbital (LUMO) energies, respectively [291]. It is well-known that this theorem is no longer applicable for the Kohn-Sham (KS) calculations using approximate exchange-correlation functionals [219, 224, 225, 292–294]. The molecular energies are poorly predicted by DFT calculations and strongly dependent on exchange-correlation functionals. Recent DFT studies, however, showed that accurate orbital energies can be provided by the generalized KS methods using the long-range corrected (LC) functionals [224, 225, 231, 232, 295, 296].

Let us here show a brief discussion to get insights into the analytic relation between

TABLE 6.4: Test molecules and reference IP and EA values (in eV) used for benchmark calculations. The values obtained at the CCSD(T)/cc-pVTZ level of theory are used for reference where experimental data are not available.

Test molecule	Exp. IPs [a]	EAs	
		Exp.	CCSD(T)
group A	Be	9.323		−0.900
	Mg	7.646		−0.653
	Ca	6.113	0.025	
	Na$_2$	4.892	0.430	
	Li$_2$	5.113		0.327
	K$_2$	4.062	0.497	
group B	NaCl	9.200	0.730	
	NaBr	8.300	0.790	
	LiCl	10.010	0.580	
	LiBr	9.310	0.640	
	Ne	21.565		−29.097
	Ar	15.760		−14.319
	HF	16.030		−3.449
	CO$_2$	13.773		−4.524
	H$_2$O	12.610		−3.279
	NH$_3$	10.070		−3.110
	CH$_4$	14.400		−3.280
	C$_2$H$_2$	11.400		−3.740

[a] The experimental values are taken from Ref.[297].

HOMO and LUMO energies versus IPs and EAs of OB-MP2, respectively. Our formulations will be expressed using canonical HF orbitals instead of OB-MP2 orbitals. This is just for clarity to reduce complexity of expressions but would not alter the essence of the consequences. The HOMO and LUMO energies of the OB-MP2 theory are then in turn written as

$$\epsilon_{\text{HOMO}}^{\text{OB-MP2}} = \epsilon_{\text{HOMO}}^{\text{HF}} + 2\overline{T}_{ih}^{ab}g_{ab}^{ih} \tag{6.21a}$$

$$\epsilon_{\text{LUMO}}^{\text{OB-MP2}} = \epsilon_{\text{LUMO}}^{\text{HF}} - 2\overline{T}_{ij}^{al}g_{al}^{ij} \tag{6.21b}$$

which are derived from the h-th and l-th diagonal elements of the Fock matrix [Eq. (6.20)] where h and l refer to the HOMO and LUMO, respectively.
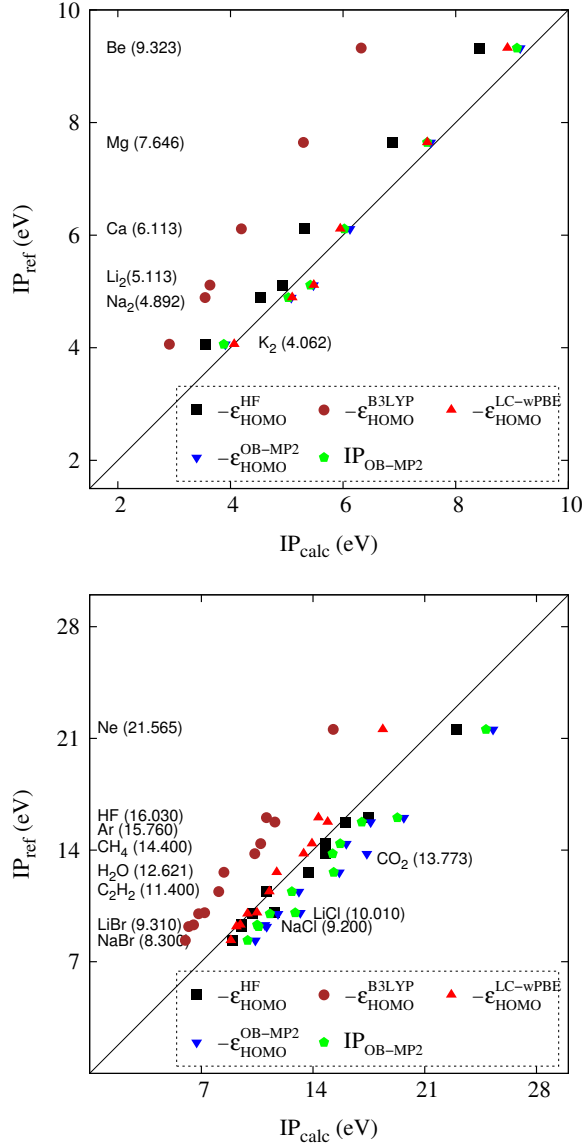
FIGURE 6.3: Reference IPs versus minus HOMO energies ($-\epsilon_{\mathrm{HOMO}}$) from HF, B3LYP, LC-wPBE, and OB-MP2 calculations as well as $\mathrm{IP_{OB\text{-}MP2}}$ [Eq. (6.22a)] for alkali metals (upper panel) and non-metallic molecules (lower panel). The straight line represents perfect correlation of measurements. The values in the parentheses inside the plots are the experimental IPs in units of eV (see Table 6.4 for details).

The IP and EA of the MP2 method are derived from a direct difference between the energy expressions of the neutral and ionized states [298, 299] as follows,

$$\mathrm{IP_{OB\text{-}MP2}} = -\epsilon_{\mathrm{HOMO}}^{\mathrm{OB\text{-}MP2}} + 2\overline{T}_{ij}^{ah}\, g_{ah}^{ij} \tag{6.22a}$$

$$\mathrm{EA_{OB\text{-}MP2}} = -\epsilon_{\mathrm{LUMO}}^{\mathrm{OB\text{-}MP2}} - 2\overline{T}_{il}^{ab}\, g_{ab}^{il} \tag{6.22b}$$

where the same set of the HF orbitals are used for the neutral and ionized states just as assumed in the Koopmans' theorem. This analysis reveals that the Koopmans' theorem does not hold true for the OB-MP2 method, i.e. $\mathrm{IP_{OB\text{-}MP2}} \neq -\epsilon_{\mathrm{HOMO}}^{\mathrm{OB\text{-}MP2}}$ and $\mathrm{EA_{OB\text{-}MP2}} \neq$

$-\epsilon_{\text{LUMO}}^{\text{OB-MP2}}$. Despite this fact, it is worth investigating to what extent the correlation effects considered in OB-MP2 calculations affect the prediction of IPs and EAs with use of orbital energies. It should be underscored that in the OO-MP2 formalism [25, 103, 168–175] the definition of the orbital energies is conceptually not unique.

TABLE 6.5: Subtraction of refernce IPs from minus HOMO energies calculated by the HF, B3LYP, LC-wPBE, and OB-MP2 methods and the values of IP$_{\text{OB-MP2}}$ [Eq. (6.22a)]. The units are in eV. The reference values are given in Table 6.4.

Molecules	$-\epsilon_{\text{HF}}^{\text{HOMO}}$	$-\epsilon_{\text{B3LYP}}^{\text{HOMO}}$	$-\epsilon_{\text{LC-wPBE}}^{\text{HOMO}}$	$-\epsilon_{\text{OB-MP2}}^{\text{HOMO}}$	IP$_{\text{OB-MP2}}$
Group A: alkali metals					
Be	−0.908	−3.002	−0.405	−0.178	−0.237
Mg	−0.760	−2.350	−0.151	−0.092	−0.154
Ca	−0.792	−1.920	−0.164	0.009	−0.091
Na$_2$	−0.355	−1.342	0.204	0.189	0.135
Li$_2$	−0.190	−1.477	0.368	0.361	0.305
K$_2$	−0.501	−1.147	0.006	−0.154	−0.180
MAD	0.584	1.873	0.216	0.164	0.184
RMS	0.638	1.980	0.255	0.196	0.197
Group B: non-metallic molecules					
NaCl	0.329	−2.991	−0.004	1.891	1.383
NaBr	0.599	−2.346	0.513	2.045	1.560
LiCl	0.202	−3.181	−0.120	1.792	1.284
LiBr	0.229	−2.800	0.130	1.675	1.191
Ne	1.440	−6.302	−3.196	3.715	3.275
Ar	0.299	−4.155	−0.843	1.854	1.293
HF	1.449	−4.950	−1.692	3.659	3.253
CO$_2$	0.988	−3.428	−0.359	3.601	1.456
H$_2$O	1.099	−4.197	−0.885	3.039	2.681
NH$_3$	1.513	−2.862	0.416	3.134	2.814
CH$_4$	0.369	−3.682	−0.466	1.684	1.301
C$_2$H$_2$	−0.298	−3.313	−0.142	1.713	1.271
MAD	0.734	3.684	0.731	2.484	1.897
RMS	0.891	3.829	1.133	2.617	2.060

Two groups of molecules were constructed for the benchmarks; the group A consists of 6 alkali metals, and the group B is the so-called non-metallic group consisting of 4 alkali metal halides, 2 noble gases, and 6 small covalent compounds. Table 6.4 shows the details of test molecules and corresponding reference values. The experimental IPs and EAs in units of eV have been adapted from Ref.[297]. The vertical EAs calculated at the CCSD(T)/cc-pVTZ level of theory are used as the reference where experimental data

are not available The negative value of EAs means that the anionic state is unbound. We performed the calculations of orbital energies on these molecules using the cc-pVTZ basis sets except for the K_2 molecule using the 6-31G basis sets [300]. In addition, $IP_{\text{OB-MP2}}$ and $EA_{\text{OB-MP2}}$ were evaluated with the optimized OB-MP2 orbitals through Eqs. (6.22a) and (6.22b), respectively.
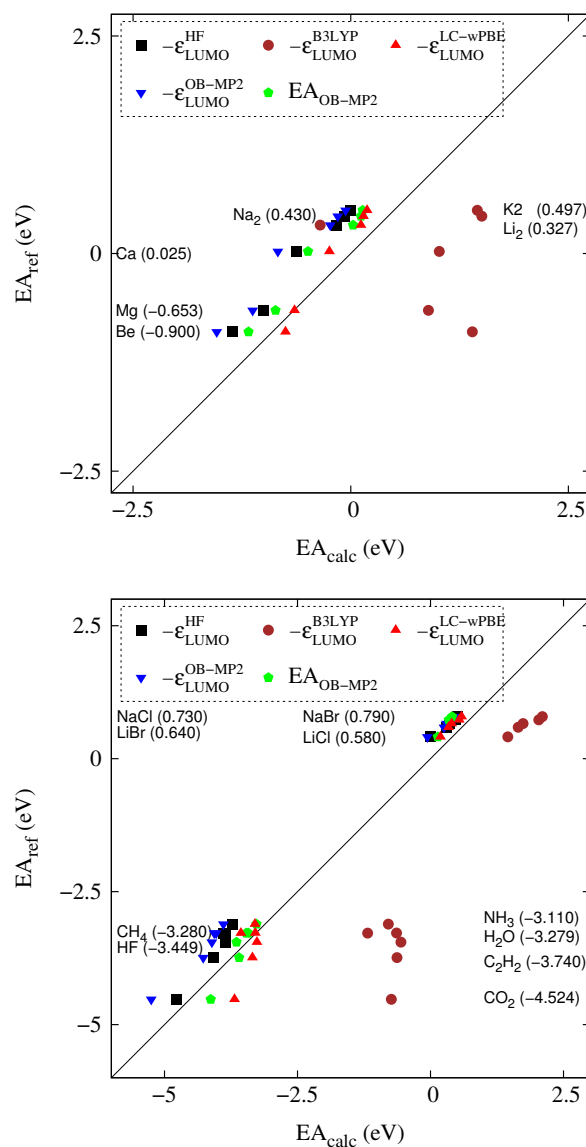
FIGURE 6.4: Reference EAs versus minus LUMO energies ($-\epsilon_{\text{LUMO}}$) from HF, B3LYP, LC-wPBE, and OB-MP2 calculations as well as $EA_{\text{OB-MP2}}$ [Eq. (6.22b)] for alkali metals (upper panel) and non-metallic molecules excluding Ar and Ne gases (lower panel). The straight line represents perfect correlation of measurements. The values in the parentheses inside the plots are the experimental or vertical CCSD(T) EAs in units of eV (see Table 6.4 for details).

Figure 6.3 presents the correlations between the experimental IPs and the minus HOMO energies of HF, B3LYP, LC-wPBE [301–303], and OB-MP2, as well as the values of $IP_{\text{OB-MP2}}$. The deviations of the calculated IPs from the experiments are shown in

Table 6.5. With the minus HOMO energies, B3LYP underestimated the IPs enormously. The OB-MP2 in general overcorrected the HF orbital energies. The prediction of the OB-MP2 theory was quite accurate for the alkali metals [group A] (the largest error 0.279 eV (5.5%) for Li_2), where the minus HOMO energies of HF underestimated the IPs with the MAE of 0.584 eV. The IPs of the non-metallic molecules [group B] were overestimated with the values of $-\epsilon_{HOMO}^{OB\text{-}MP2}$, while they were obtained to a good accuracy by the Koopmans' theorem with the HF orbitals. The values of $IP_{OB\text{-}MP2}$ [Eq. (6.22a)] generally reduced the overestimation of the OB-MP2 orbital energies, and thus the results for the non-metallic group were improved from the MAD of 2.484 eV ($-\epsilon_{HOMO}^{OB\text{-}MP2}$) to the MAD of 1.897 eV ($IP_{OB\text{-}MP2}$). The degree of this error reduction, however, does not seem to be so significant, implying that minus HOMO energies of OB-MP2 are relatively a good approximation to $IP_{OB\text{-}MP2}$. The long-range correction in LC-wPBE was confirmed to give HOMO energies in good agreement with the experimental IPs. In the case of the alkali metal group, the OB-MP2 predictions were rather accurate compared to the LC-wPBE counterparts.

The correlations between the reference EAs and predictions from HF, DFT, as well as OB-MP2 theories are shown in Figure 6.4. The errors of calculated EAs from the reference are summarized in Table 6.6. Although the HF theory is widely recognized to give poor LUMO energies, the minus LUMO energies of the present HF calculations showed rather good agreement with the reference EAs, especially for non-metallic systems [group B]. The B3LYP calculations largely overestimated the EAs in most cases except for Na_2 molecule. Using either the minus LUMO energies or Eq. (6.22b), the OB-MP2 predictions of the EAs for non-metallic group were more accurate than those for alkali metal group. The minus LUMO energies of the OB-MP2 theory underestimated the reference EAs for both test groups, while this underestimation was reduced by using $EA_{OB\text{-}MP2}$ to some extent.

The MADs and RMSs of $EA_{OB\text{-}MP2}$ were approximately less than half those of $-\epsilon_{HOMO}^{OB\text{-}MP2}$. The LC-wPBE functional provided the negative of LUMO energies in good agreement with reference EAs, as likewise observed in the IP calculations. Interestingly, for the group B, the minus LUMO energies of OB-MP2 were somewhat comparable to those of the LC-wPBE functional, and OB-MP2 using $EA_{OB\text{-}MP2}$ outperformed LC-wPBE in the calculation of the EAs.

Overall, the results of OB-MP2 for computing IPs and EAs were found to be quite encouraging although the results contained some outliers. The accuracy of the prediction using orbital energies is in general improved by using $IP_{OB\text{-}MP2}$ [Eq. (6.22a)] and

$EA_{\text{OB-MP2}}$ [Eq. (6.22b)] instead, notably for EAs. Although the orbital energies of OB-MP2 theory do not satisfy the Koopmans' theorem, they provide a good estimation of IPs and EAs.

TABLE 6.6: Subtraction of reference EAs from minus LUMO energies calculated by the HF, B3LYP, LC-wPBE, and OB-MP2 methods and the values of $EA_{\text{OB-MP2}}$ [Eq. (6.22b)]. The units are in eV. The reference values are given in Table 6.4.

Molecules	$-\epsilon_{\text{HF}}^{\text{LUMO}}$	$-\epsilon_{\text{B3LYP}}^{\text{LUMO}}$	$-\epsilon_{\text{LC-wPBE}}^{\text{LUMO}}$	$-\epsilon_{\text{OB-MP2}}^{\text{LUMO}}$	$EA_{\text{OB-MP2}}$
Group A: alkali metals					
Be	-0.459	2.297	0.151	-0.640	-0.274
Mg	-0.345	1.546	0.007	-0.474	-0.210
Ca	-0.645	0.992	-0.270	-0.862	-0.516
Na_2	-0.497	1.076	-0.283	-0.579	-0.312
Li_2	-0.492	-0.678	-0.210	-0.563	-0.300
K_2	-0.496	0.957	-0.310	-0.556	-0.360
MAD	0.489	1.258	0.205	0.612	0.329
RMS	0.497	1.365	0.229	0.624	0.342
Group B: non-metallic molecules					
NaCl	-0.257	1.306	-0.189	-0.303	-0.218
NaBr	-0.280	1.313	-0.205	-0.328	-0.231
LiCl	-0.299	1.058	-0.251	-0.336	-0.246
LiBr	-0.313	1.079	-0.262	-0.358	-0.253
Ne	-0.804	5.740	1.998	-1.421	-0.645
Ar	-0.651	3.767	0.556	-0.944	-0.212
HF	-0.403	2.893	0.186	-0.660	-0.198
CO_2	-0.243	3.787	0.839	-0.727	0.393
H_2O	-0.572	2.640	-0.015	-0.787	-0.183
NH_3	-0.612	2.317	-0.189	-0.782	-0.162
CH_4	-0.609	2.099	-0.285	-0.750	-0.143
C_2H_2	-0.346	3.110	0.393	-0.535	0.142
MAD	0.449	2.592	0.447	0.661	0.252
RMS	0.484	2.915	0.678	0.730	0.286

6.3.3 Orbital energy levels: octahedral FeH_6^{2+}

In transition metal systems, a large amount of short-range Coulombic interaction arises from a number of electrons locally packed in atomic d-block space. Dynamic correlation associated with this type of interaction plays a significant role in determining their chemical picture in qualitative terms. The electron correlation is ignored in HF calculations,

so that, as is widely recognized, the chemical characterization using HF orbitals are not good for metal complexes. It is thus of great interest to illustrate how the OB-MP2 method alters the one-electron interpretation of the electronic structure of transition metals.
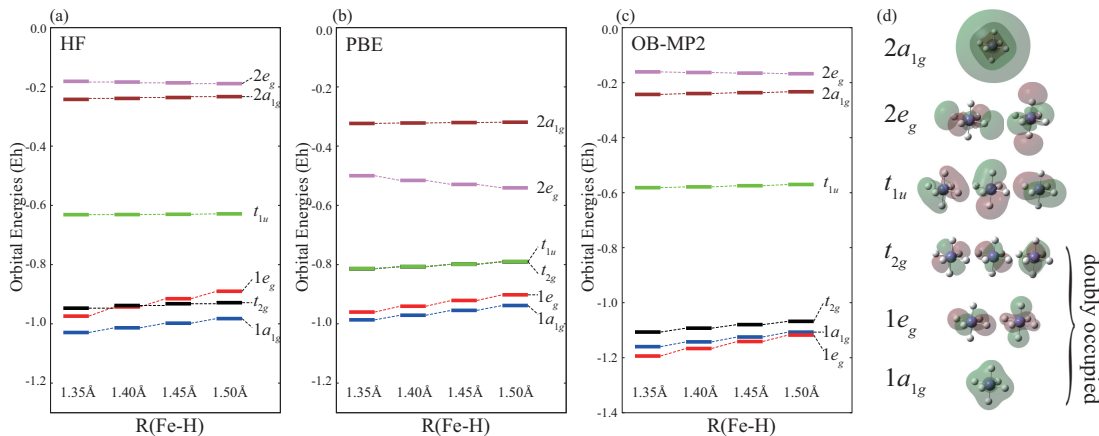
FIGURE 6.5: Energy levels of the valence orbital states ($1a_g$, $1e_g$, t_{2g}, t_{1u}, $2e_g$, and $2a_g$) of FeH_6^{2+} in the closed-shell singlet state $^1\Sigma$ with various bond lengths: R(Fe-H) = 1.35, 1.40, 1.45, and 1.50 Å, calculated by the (a) HF, (b) PBE, and (c) OB-MP2 methods. (d) The 3D plots of the MOs from the OB-MP2 calculation. The bonding $1a_{1g}$ and $1e_g$ orbitals and the nonbonding t_{2g} (d_{xy}, d_{yz}, d_{zx}) orbitals are doubly-occupied. The bonding t_{1u} and anti-bonding $2e_g$ and $2a_{1g}$ orbitals are empty states.

For the performance test, we examined the orbital energy levels of FeH_6^{2+}, an elemental octahedral coordination complex. It has H atoms as all the ligands along the x-, y-, and z-axes, so that the ligands only have σ-type interaction with the metal. In the ligand field theory (LFT), this metal-ligand interaction is characterized by MOs with e_g symmetry, which are involved with the $d_{x^2-y^2}$ and d_{z^2} orbitals of the Fe atom (Fig. 6.5(d)). The rest of the d-block orbitals, d_{xy}, d_{xz}, and d_{yz}, corresponding to t_{2g} symmetry, are of the nonbonding character in this system. The e_g orbitals are directly affected by the ligand field, splitting to the stabilized bonding ($1e_g$) and destabilized antibonding ($2e_g$) states, while the t_{2g} orbitals have no overlap with ligands. With this interaction structure, the LFT predicts the energy ordering of these MOs as $\epsilon_{1e_g} < \epsilon_{t_{2g}} < \epsilon_{2e_g}$.

We performed the OB-MP2 calculations on the FeH_6^{2+} molecule in the closed-shell singlet state $^1\Sigma$ with the cc-pVDZ basis sets. The strength of the ligand field was varied by changing the length of the Fe-H bonds under the O_h symmetry: R(Fe-H) = 1.35, 1.40, 1.45, and 1.50 Å. Figure 6.5 presents the orbital energy levels of OB-MP2 as a function of the bond length, along with the HF and PBE [10, 11] results for comparison.

With all the three methods, the antibonding $2e_g$ orbitals were shown to be higher in energy than the $1e_g$ and t_{2g} orbitals, in accordance with the LFT description. With increasing the bond length, namely with lessening the ligand field, the energy level of the bonding $1e_g$ orbitals grows increasingly higher in all cases. In the HF case, it crosses

the level of the nonbonding t_{2g} orbitals and can have a higher energy than t_{2g}. This is a surprising contradiction to the orbital picture of LFT. In the OB-MP2 and PBE calculations for all the tested bond lengths, we observed that the $1e_g$ orbitals is stabilized relative to the t_{2g} orbitals owing to the metal-ligand interaction. The OB-MP2 and PBE orbitals associated with d-block then resulted in the same energy ordering as the LFT prediction. This reveals the role of electron correlation in delivering a qualitative accuracy to the orbital picture.

Because the t_{2g} orbitals of FeH_6^{2+} are classified as nonbonding by symmetry, the effects of the ligand field on them cannot be accounted for by the LFT. As shown in Fig. 6.5, the OB-MP2 and PBE results presented a clear dependence of the t_{2g} orbital energies on the bond lengths. Note that the SCF calculations using the hybrid B3LYP and PBE0 [304] functionals failed to converge for this system. The difference in the t_{2g} orbital energy between R(Fe-H) = 1.35 and 1.50 Å is 0.0390 and 0.0238 E_h for OB-MP2 and PBE, respectively, while that for HF is 0.0183 E_h. This means that the electron correlation enhances the ligand effects on the t_{2g} orbitals. These orbital descriptions certainly go beyond the classical interpretation of coodination bonds based on the LFT.

6.3.4 Orbital energy levels: linear CoNO

As another test case, we examined the orbital energy levels of the linearly-coordinated CoNO molecule, which has σ- and π-type metal-ligand interactions. The HF, B3LYP and OB-MP2 calculations were carried out with the equilibrium geometry (R(Co-N) = 1.556 Å and R(N-O) = 1.171 Å). The following is the resulting valence configurations each written in increasing orbital energy order:

$$\text{HF: } (\ldots)\, \delta^4\, 3\sigma^{*2}\, 2\pi^4\, 4\sigma^{*0}\, 2\pi^{*0}$$
$$\text{B3LYP: } (\ldots)\, 2\pi^4\, 3\sigma^{*2}\, \delta^4\, 4\sigma^{*0}\, 2\pi^{*0}$$
$$\text{OB-MP2: } (\ldots)\, 2\pi^4\, \delta^4\, 3\sigma^{*2}\, 4\sigma^{*0}\, 2\pi^{*0}$$

where $(\ldots)$ denotes the lower-lying occupied orbitals, whose energy ordering was common among the three models.

Figure 6.6 displays the shapes of the occupied valence orbitals $3\sigma^*$, δ and 2π. The energies of these orbitals are shown in Table 6.7. The $3\sigma^*$ orbital is constructed from the metal d_{z^2} and the ligand $\sigma(NO)$ orbitals and is antibonding with respect to Co and NO. The δ orbitals are of nonbonding character, locally residing in the atomic d_{xy} and $d_{x^2-y^2}$ orbitals of Co. The 2π orbitals associated with d_{zx}, d_{yz} and $\pi^*(NO)$ are bonding with respect to Co and NO. Experimental evidence indicates that the NO ligand is one

of the strongest π-acceptor [305, 306]. The antibonding $\pi^*(\text{NO})$ is in favor of accepting metal d electrons, thus playing a role in the form of the stable π-type metal-ligand bonding. The energy of this 2π orbitals is thus considered to be the lowest of these three [306]. The correlated orbitals of OB-MP2 as well as B3LYP provided the orbital description in accordance with this speculation, whereas the HF orbitals failed to capture it.
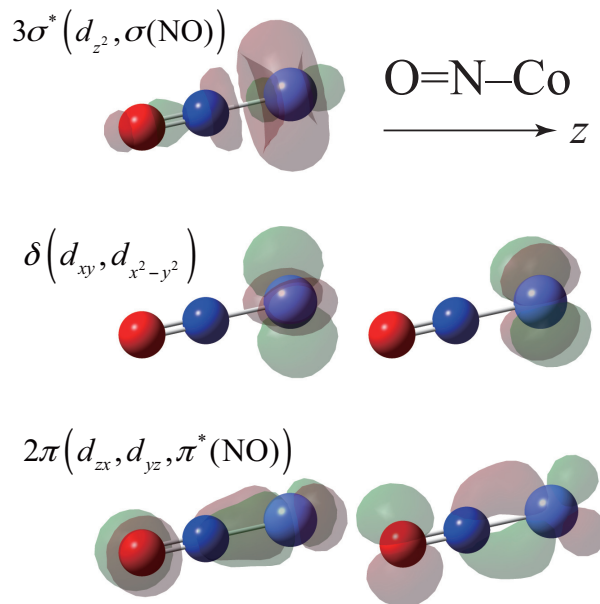
FIGURE 6.6: The 3D plots of the $2\pi\,(d_{zx}, d_{yz}, \pi^*(\text{NO}))$, $\delta\,(d_{xy}, d_{x^2-y^2})$ and $3\sigma^*\,(d_{d^2}, \sigma(\text{NO}))$ orbitals of the CoNO molecule. They are doubly-occupied in the HF, B3LYP, and OB-MP2 calculations. Co, N, and O atoms are shown in purple, blue, and red, respectively.

TABLE 6.7: Orbital energies (in E_h) of the occupied orbital states $2\pi\,(d_{zx}, d_{yz}, \pi^*(\text{NO}))$, $\delta\,(d_{xy}, d_{x^2-y^2})$ and $3\sigma^*\,(d_{d^2}, \sigma(\text{NO}))$ (shown in Fig. 6.6) of CoNO from the HF, B3LYP, and OB-MP2 calculations.

orbital state	orbital energies		
	HF	B3LYP	OB-MP2
$3\sigma^*\,(d_{d^2}, \sigma(\text{NO}))$	-0.4224	-0.2136	-0.5386
$\delta\,(d_{xy}, d_{x^2-y^2})$	-0.4483	-0.1955	-0.6303
$2\pi\,(d_{zx}, d_{yz}, \pi^*(\text{NO}))$	-0.2878	-0.2364	-0.6565

6.4 Conclusion

We have developed the effective one-body (or Fock-like) Hamiltonian which is perturbed with electron correlation at the MP2 level on the basis of canonical transformation.

The mean-field approximation was used to reduce a high-rank representation of many-electron correlation into the one-body potential. Orbital descriptions including energy levels are optimized by repeatedly diagonalizing the one-body MP2 (OB-MP2) Hamiltonian, where the amplitudes of transformation based on the MP1 wave function are concomitantly updated, including their denominators. When using HF orbitals, the expectation value of the OB-MP2 Hamiltonian, regarded as an orbital-dependent energy functional, reproduces the MP2 energy. The orbital energies arise as an intrinsic output of OB-MP2. This makes a strong contrast with OO-MP2, which does not have the canonical form of orbital picture. Thus, in the prevous OO-MP2 method, the denominators of the MP1 wave function are kept fixed using HF orbital energies.

The importance of including MP2-level correlation into the orbital (or mean-field) picture was highlighted in the illustrative calculations of reaction energies, ionization potentials and electron affinities from the Koopmans' theorem, and orbital energy levels of coordination complexes. The comparison of the MP2 and OB-MP2 calculations on reaction energies of closed-shell main group systems showed that the refinement associated with orbital optimization is rather minor. Our implementation based on the spin-free formalism is limited to the applications to the the closed-shell systems. Orbital optimization is considered to be effective for open-shell radical organic molecules, where the unrestricted-orbital variants of OB-MP2 should come into play. The ionitzation potentials and electron affinities of OB-MP2 were much better than those of B3LYP and in many cases comparable to those of the LC functional. The HF calculations of metal complexes yielded spurious valence energy levels, whereas OB-MP2 offered a qualitative improvement on them. Linear response or single CI formalism can be incorporated into the OB-MP2 Hamiltonian as an extension to calculate excited states at the MP2 level in a similar spirit of the CIS(D) [307] or CC2 [308] methods. Grimme's spin-component scaling factors might improve the description of the OB-MP2 potential [Eqs. (6.17) and (6.18)]. Another extension is to incorporate our one-body potential into the DFT calculations, developing a type of the double hybrid approach that combines MP2 and DFT at a deeper level than B2PLYP [309] and others. The developments along these lines are the subject of active investigation.

Chapter 7

General Conclusions

Generally, it is doubtless that the molecular EPR spectroscopy is one of the most powerful tools for investigating electronic and structural features of paramagnetic molecules. Beside experimental measurements, theoretical interpretations are also important not only for explaining what governs the observed spectra, but also for predicting parameters that are not easy to measure in experiment.

Although DFT has been extensively used due to its low computational requirements, it has some critical disadvantages. The most well-known problem of DFT is that the exchange-correlation functionals appropriate for prediction of molecular properties are system-dependent. In other words, the use of DFT calculations for molecular properties thus requires careful validation for a given functional and molecule. Moreover, a general unsolved question in DFT calculations of magnetic properties is the dependence of the exchange-correlation potential on the paramagnetic current induced by the magnetic field. Thus, the use of *ab initio* wavefunction methods for calculations of molecular magnetic properties is highly desirable. Based on this motivation, presented thesis is devoted to develop and/or assess new *ab initio* quantum chemical methods for accurate predictions of molecular EPR parameters: HFCCs and $g-$tensors. We particularly focus on the *ab initio* DMRG method, which has been shown to be successful for the prediction of molecular properties in large-scale multireference states.

The calculations of isotropic HFCCs, which require correlation of core electron, is known to be most demanding for modern theoretical methods. Apart from the electron correlation, relativistic effects also play an important role in the accurate prediction of isotropic HFCCs. Only a few computational schemes including both high-level correlations and relativistic effects were published so far, such as QCISD/IORAmm [26], QCISD/NESC, CCSD/NESC [28], and MCDF [16].

Regarding the molecular $g-$tensors, there are generally two different computational approaches employing first-order and second-order perturbation theory. In framework of *ab initio* wavefunction methods, both these approaches are usually based on the state expansion, which is practically truncated. There were several studies reporting methods that are equivalent to the untruncated expansion, such as LR-CASSCF [48], CP-MRCI [51], analytical CC [53], variational SO-CASSCF [57], and single-reference 4c-CI [58]. However, these methods are expensive and thus impractical for predicting the $g-$tensors for larger molecules. The DMRG based methods, such as analytical DMRG [85] or 4c-DMRG [123], are therefore expected to be helpful.

In Chapter 2, DMRG calculations were performed to predict HFCCs of 4 $^2\Sigma$ diatomic radicals (BO, CO$^+$, CN, and AlO) and vinyl (C$_2$H$_3$) radical. From the results, two technical points can be summarized as follows. (i) The active space method has the potential to accurately describe the HFCCs, but the active space must be addressed by the construction of active orbitals. Generally, the FC term is particularly sensitive to the choice of active space. Moreover, the DMRG method is also suitable to deal with multireference cases such as the AlO radical. (ii) It is necessary to correlate the core electrons to correctly obtain the spin density at the nucleus; therefore, the core orbitals should be included in CAS. At the same time, inclusion of polarization shells is necessary to describe the dynamical correlation effects, which provide the corresponding polarization.

In Chapter 3, we have newly developed a computational scheme, referred to as DMRG-CASSCF/DKH3, for the accurate prediction of HFCCs of heavy molecules. As test cases, we have evaluated the HFCCs for $4d$ transition metal radicals: Ag atom, PdH, and RhH$_2$. Good agreement between the isotropic HFCCs obtained from DMRG-CASSCF/DKH3 and experiment in inert gas matrices was found. Because there are no available gas-phase values for these radicals in literatures, the results from high-level theory, as used in this work, can serve as benchmark data.

In Chapter 4, we have newly implemented the CP-CASSCF method for calculating molecular $g-$tensors. As the first step before employing the DMRG method, FCI has been used to fully treat the correlation in active space. The perturbation-induced orbital relaxation was also taken into account. We have tested our implementation by evaluating the $g-$values for a series of small radicals including light doublet and light triplet radicals, as well as heavy doublet hydrides and dihydrides. For light molecules, our results are quite consistent with the MRCI results and comparable to the experimental values, especially for triplet radicals. For comparison, the QDPT approach was also employed. The inconsistency between CP- and QDPT-CASSCF results is pronounced

for heavy radicals, where the higher-order SOC effects become important. Further comparisons for larger molecules need to be performed in order to reveal the advantages and disadvantages of these two approaches. Working on this issue is in progress.

In Chapter 5, we formulated the CP-DMRG method for $g-$tensor calculations. Unlike the FCI method, the evaluation of first-order spin density requires not only the first-order wavefunction obtained by solving the CP-DMRG equation, but also the first-order spin density operator originating from the first-order renormalization bases. Details of algorithm and implementation were provided. The CP-DMRG is believed to be the useful tool to evaluate the molecular $g-$tensors of large organic radicals, where SOC is expected to be weak.

Apart from EPR parameter calculations, we presented our new development on the effective one-body (or Fock-like) Hamiltonian, which is perturbed with electron correlation at the MP2 level on the basis of canonical transformation in Chapter 6. Orbital descriptions including energy levels are optimized by repeatedly diagonalizing the one-body MP2 (OB-MP2) Hamiltonian, where the amplitudes of transformation based on the MP1 wave function are concomitantly updated, including their denominators. Numerical performance is illustrated in molecular applications for computing reaction energies, applying Koopman's theorem, and examining the effects of dynamic correlation on energy levels of metal complexes. Our implementation based on the spin-free formalism is limited to the applications to the closed-shell systems so far . Extending this method for the open-shell systems and applying to the EPR parameter calculations are appealing and interesting.

Bibliography

[1] H. Sekino and R. J. Bartlett, J. Chem. Phys. **82**, 4225 (1985).

[2] S. A. Perera, J. D. Watts, and R. J. Bartlett, J. Chem. Phys. **100**, 1425 (1994).

[3] T. Momose, H. Nakatsuji, and T. Shida, J. Chem. Phys. **89**, 4185 (1988).

[4] T. Momose, M. Yamaguchi, and T. Shida, J. Chem. Phys. **93**, 7284 (1990).

[5] D. M. Chipman, Theor. Chim. Acta **82**, 93 (1992).

[6] B. Engels, Chem. Phys. Lett. **179**, 398 (1991).

[7] B. Engels, J. Chem. Phys. **100**, 1380 (1994).

[8] C. Lee, W. Yang, and R. G. Parr, Phys. Rev. B **37**, 785 (1988).

[9] A. D. Becke, J. Chem. Phys. **98**, 5648 (1993).

[10] J. P. Perdew, K. Burke, and M. Ernzerhof, Phys. Rev. Lett. **77**, 3865 (1996).

[11] J. P. Perdew, K. Burke, and M. Ernzerhof, Phys. Rev. Lett. **78**, 1396 (1997).

[12] S. Kossmann, B. Kirchner, and F. Neese, Mol. Phys. **105**, 2049 (2007).

[13] J. Tao, J. P. Perdew, V. N. Staroverov, and G. E. Scuseria, Phys. Rev. Lett. **91**, 146401 (2003).

[14] S. Grimme, J. Chem. Phys. **124**, 034108 (2006).

[15] H. M. Quiney and P. Belanzoni, Chem. Phys. Lett. **353**, 253 (2002).

[16] S. Song, G. Wang, A. Ye, and G. Jiang, J. Phys. B **40**, 475 (2007).

[17] E. Malkin, M. Repiský, S. Komorovský, P. Mach, O. L. Malkina, and V. G. Malkin, J. Chem. Phys. **134**, 044111 (2011).

[18] E. van Lenthe, A. van der Avoird, and P. E. S. Wormer, J. Chem. Phys. **108**, 4783 (1998).

[19] P. Belanzoni, E. van Lenthe, and E. J. Baerends, J. Chem. Phys. **114**, 4421 (2001).

[20] F. Aquino, B. Pritchard, and J. Autschbach, J. Chem. Theory Comput. **8**, 598 (2012).

[21] J. Autschbach, S. Patchkovskii, and B. Pritchard, J. Chem. Theory Comput. **7**, 2175 (2011).

[22] P. Verma and J. Autschbach, J. Chem. Theory Comput. **9**, 1932 (2013).

[23] I. Malkin, O. L. Malkina, V. G. Malkin, and M. Kaupp, Chem. Phys. Lett. **396**, 268 (2004).

[24] E. Malkin, I. Malkin, O. L. Malkina, V. G. Malkin, and M. Kaupp, Phys. Chem. Chem. Phys. **8**, 4079 (2006).

[25] B. Sandhoefer, S. Kossmann, and F. Neese, J. Chem. Phys. **138**, 104102 (2013).

[26] M. Filatov and D. Cremer, J. Chem. Phys. **121**, 5618 (2004).

[27] M. Filatov and D. Cremer, J. Chem. Phys. **123**, 124101 (2005).

[28] M. Filatov, W. Zou, and D. Cremer, J. Phys. Chem. A **116**, 3481 (2012).

[29] E. Vanlenthe, P. Wormer, and A. Vanderavoird, J. Chem. Phys. **107**, 2488 (1997).

[30] K. M. Neyman, D. I. Ganyushin, A. V. Matveev, and V. A. Nasluzov, J. Chem. Phys. A **106**, 5022 (2002).

[31] I. Malkin, O. L. Malkina, V. G. Malkin, and M. Kaupp, J. Chem. Phys. **123**, 244103 (2005).

[32] S. Komorovský, M. Repiský, O. L. Malkina, V. G. Malkin, I. Malkin, and M. Kaupp, J. Chem. Phys. **124**, 084108 (2006).

[33] M. Repiský, S. Komorovský, E. Malkin, O. L. Malkina, and V. G. Malkin, Chem. Phys. Lett. **488**, 94 (2010).

[34] G. Schreckenbach and T. Ziegler, J. Phys. Chem. A **101**, 3388 (1997).

[35] S. Patchkovskii and T. Ziegler, J. Phys. Chem. A **105**, 5490 (2001).

[36] O. L. Malkina, J. Vaara, B. Schimmelpfennig, M. Munzarova, V. G. Malkin, and M. Kaupp, J. Am. Chem. Soc **122**, 9206 (2000).

[37] M. Kaupp, R. Reviakine, O. L. Malkina, A. Arbuznikov, B. Schimmelpfennig, and V. G. Malkin, J. Comput. Chem. **23**, 794 (2002).

[38] F. Neese, J. Chem. Phys. **115**, 11080 (2001).

[39] F. Neese, J. Chem. Phys. **118**, 3939 (2003).

[40] Z. Rinkevicius, L. Telyatnyk, P. Sałek, O. Vahtras, and H. Ågren, J. Chem. Phys **119**, 10489 (2003).

[41] P. Hrobárik, M. Repiský, S. Komorovský, V. Hrobáriková, and M. Kaupp, Theor. Chem. Acc. **129**, 715 (2011).

[42] J. Autschbach, S. Patchkovskii, and B. Pritchard, J. Chem. Theory Comput. **7**, 2175 (2011).

[43] P. Verma and J. Autschbach, J. Chem. Theory Comput. **9**, 1052 (2013).

[44] G. Lushington, P. Bündgen, and F. Grein, Int. J. Quantum Chem. **55**, 377 (1995).

[45] P. Bündgen, G. H. Lushington, and F. Grein, Int. J. Quantum Chem. **56**, 283 (1995).

[46] G. Lushington and F. Grein, Theor. Chim. Acta **93**, 259 (1996).

[47] P. J. Bruna, G. H. Lushington, and F. Grein, Chem. Phys. **225**, 1 (1997).

[48] O. Vahtras, B. Minaev, and H. Ågren, Chem. Phys. Lett. **281**, 186 (1997).

[49] S. Brownridge, F. Grein, J. Tatchen, M. Kleinschmidt, and C. M. Marian, J. Chem.l Phys. **118**, 9552 (2003).

[50] F. Neese, Chem. Phys. Lett. **380**, 721 (2003).

[51] F. Neese, Mol. Phys. **105**, 2507 (2007).

[52] S. Vancoillie, P.-Å. Malmqvist, and K. Pierloot, ChemPhysChem **8**, 1803 (2007).

[53] J. Gauss, M. Kállay, and F. Neese, J. Phys. Chem. A **113**, 11541 (2009).

[54] H. Bolvin, ChemPhysChem **7**, 1575 (2006).

[55] J. Tatchen, M. Kleinschmidt, and C. M. Marian, J. Chem. Phys **130**, 154106 (2009).

[56] L. F. Chibotaru and L. Ungur, J. Chem. Phys **137**, 064112 (2012).

[57] D. Ganyushin and F. Neese, J. Chem. Phys **138**, 104113 (2013).

[58] M. S. Vad, M. N. Pedersen, A. Nørager, and H. J. A. Jensen, J. Chem. Phys **138**, 214106 (2013).

[59] S. R. White, Phys. Rev. Lett. **69**, 2863 (1992).

[60] S. R. White, Phys. Rev. B **48**, 10345 (1993).

[61] S. R. White and R. L. Martin, J. Chem. Phys. **110**, 4127 (1999).

[62] A. O. Mitrushenkov, G. Fano, F. Ortolani, R. Linguerri, and P. Palmieri, J. Chem. Phys. **115**, 6815 (2001).

[63] G. K.-L. Chan and M. Head-Gordon, J. Chem. Phys. **116**, 4462 (2002).

[64] G. K.-L. Chan and M. Head-Gordon, J. Chem. Phys. **118**, 8551 (2003).

[65] Ö. Legeza, J. Röder, and B. A. Hess, Phys. Rev. B **67**, 125114 (2003).

[66] G. Moritz and M. Reiher, J. Chem. Phys. **126**, 244109 (2007).

[67] D. Zgid and M. Nooijen, J. Chem. Phys. **128**, 014107 (2008).

[68] D. Zgid and M. Nooijen, J. Chem. Phys **128**, 144116 (2008).

[69] K. H. Marti, I. M. Ondík, G. Moritz, and M. Reiher, J. Chem. Phys. **128**, 014104 (2008).

[70] Y. Kurashige and T. Yanai, J. Chem. Phys. **130**, 234114 (2009).

[71] D. Ghosh, J. Hachmann, T. Yanai, and G. K. Chan, J. Chem. Phys. **128**, 144117 (2008).

[72] T. Yanai, Y. Kurashige, D. Ghosh, and G. K. Chan, Int. J. Quantum Chem. **109**, 2178 (2009).

[73] G. K.-L. Chan, M. Kállay, and J. Gauss, J. Chem. Phys. **121**, 6110 (2004).

[74] G. K.-L. Chan, J. Chem. Phys. **120**, 3172 (2004).

[75] J. Hachmann, W. Cardoen, and G. K.-L. Chan, J. Chem. Phys. **125**, 144101 (2006).

[76] J. Hachmann, J. J. Dorando, M. Avilés, and G. K.-L. Chan, J. Chem. Phys. **127**, 134309 (2007).

[77] T. Yanai, Y. Kurashige, E. Neuscamman, and G. K.-L. Chan, J. Chem. Phys. **132**, 024105 (2010).

[78] Y. Kurashige and T. Yanai, J. Chem. Phys. **135**, 094104 (2011).

[79] Y. Kurashige, G. K.-L. Chan, and T. Yanai, Nature Chem. **5**, 660 (2013).

[80] M. Saitow, Y. Kurashige, and T. Yanai, J. Chem. Phys. **139**, 044118 (2013).

[81] G. Barcza, Ö. Legeza, K. Marti, and M. Reiher, Phys. Rev. A **83**, 012508 (2011).

[82] P. Tecmer, K. Boguslawski, Ö. Legeza, and M. Reiher, Phys. Chem. Chem. Phys. **16**, 719 (2014).

[83] K. Boguslawski, K. H. Marti, Ö. Legeza, and M. Reiher, J. Chem. Theory Comput. **8**, 1970 (2012).

[84] J. Chalupský and T. Yanai, J. Chem. Phys **139**, 204106 (2013).

[85] J. J. Dorando, J. Hachmann, and G. K.-L. Chan, J. Chem. Phys. **130**, 184111 (2009).

[86] W. Kutzelnigg, Theor. Chim. Acta **73**, 173 (1988).

[87] R. A. Frosch and H. Foley, Phys. Rev. **88**, 1337 (1952).

[88] J. W. Gauld, L. A. Eriksson, and L. Radom, J. Phys. Chem. A **101**, 1352 (1997).

[89] B. Lengsfield III and B. Liu, J. Chem. Phys. **77**, 6083 (1982).

[90] L. B. Knight Jr, T. J. Kirk, J. Herlong, J. G. Kaup, and E. Davidson, J. Chem. Phys. **107**, 7011 (1997).

[91] F. Grein, J. Phys. Chem. A **109**, 9270 (2005).

[92] F. Grein, Chem. Phys. Lett. **418**, 100 (2006).

[93] N. Gilka, J. Tatchen, and C. Marian, Chem. Phys. **343**, 258 (2008).

[94] M. Dupuis, J. Rys, and H. F. King, J. Chem. Phys **65**, 111 (1976).

[95] P.-O. Widmark, P.-Å. Malmqvist, and B. O. Roos, Theor. Chim. Acta **77**, 291 (1990).

[96] P.-O. Widmark, B. J. Persson, and B. O. Roos, Theor. Chim. Acta **79**, 419 (1991).

[97] G. Karlström, R. Lindh, P.-Å. Malmqvist, B. O. Roos, U. Ryde, V. Veryazov, P.-O. Widmark, M. Cossi, B. Schimmelpfennig, P. Neogrady, et al., Comput. Mater. Sci. **28**, 222 (2003).

[98] G. Herzberg, *Molecular spectra and molecular structure: Spectra of diatomic molecules* (Van Nostrand Reinhold: New York, 1950).

[99] F. Neese, WIREs: Comput. Mol. Sci. **2**, 73 (2012).

[100] A. D. Becke, Phys. Rev. A **38**, 3098 (1988).

[101] J. P. Perdew, Phys. Rev. B **33**, 8822 (1986).

[102] M. J. Frisch, G. W. Trucks, H. B. Schlegel, G. E. Scuseria, M. A. Robb, J. R. Cheeseman, G. Scalmani, V. Barone, B. Mennucci, G. A. Petersson, et al., *Gaussian 09, Revision A.1*, Gaussian, Inc., Wallingford, CT (2009).

[103] S. Kossmann and F. Neese, J. Phys. Chem. A **114**, 11768 (2010).

[104] K. A. Peterson and T. H. Dunning Jr, J. Chem. Phys. **106**, 4119 (1997).

[105] N. Rega, M. Cossi, and V. Barone, J. Chem. Phys. **105**, 11060 (1996).

[106] M. Tanimoto, S. Saito, and E. Hirota, J. Chem. Phys. **84**, 1210 (1986).

[107] L. B. Knight Jr, W. C. Easley, and W. Weltner Jr, J. Chem. Phys. **54**, 1610 (1971).

[108] L. B. Knight Jr, M. Wise, E. Davidson, and L. McMurchie, J. Chem. Phys. **76**, 126 (1982).

[109] L. B. Knight Jr, J. O. Herlong, T. J. Kirk, and C. Arrington, J. Chem. Phys. **96**, 5604 (1992).

[110] N. D. Piltch, P. G. Szanto, T. G. Anderson, C. S. Gudeman, T. A. Dixon, and R. C. Woods, J. Chem. Phys. **76**, 3385 (1982).

[111] L. B. Knight Jr and J. Steadman, J. Chem. Phys. **77**, 1750 (1982).

[112] L. B. Knight Jr and J. Steadman, J. Am. Chem. Soc. **106**, 900 (1984).

[113] B. Fernández, P. Jørgensen, and J. Simons, J. Chem. Phys. **98**, 7012 (1993).

[114] B. Fernandez, P. Jørgensen, J. Byberg, J. Olsen, T. Helgaker, and H. J. A. Jensen, J. Chem. Phys. **97**, 3412 (1992).

[115] W. C. Easley and W. Weltner Jr, J. Chem. Phys. **52**, 197 (1970).

[116] L. Knight Jr and W. Weltner Jr, J. Chem. Phys. **55**, 5066 (1971).

[117] C. Yamada, E. A. Cohen, M. Fujitake, and E. Hirota, J. Chem. Phys. **92**, 2146 (1990).

[118] W. Kutzelnigg, U. Fleischer, and M. Schindler, *NMR basic principles and progress* (Springer-Verlag: Heidelberg, Germany, 1990).

[119] N. Ishii and T. Shimizu, Chem. Phys. Lett. **225**, 462 (1994).

[120] D. M. Chipman, *Quantum mechanical electronic structure calculations with chemical accuracy*, vol. 13 (Kluwer Academic Publisher: Dordrecht, The Netherlands, 1995).

[121] S. A. Perera, L. M. Salemi, and R. J. Bartlett, J. Chem. Phys. **106**, 4061 (1997).

[122] A. R. Al Derzi, S. Fau, and R. J. Bartlett, J. Phys. Chem. A **107**, 6656 (2003).

[123] S. Knecht, Ö. Legeza, and M. Reiher, J. Chem. Phys. **140**, 041101 (2014).

[124] T. Nakajima and K. Hirao, J. Chem. Phys. **113**, 7786 (2000).

[125] A. Wolf, M. Reiher, and B. A. Hess, J. Chem. Phys. **117**, 9215 (2002).

[126] M. Barysz and A. J. Sadlej, J. Chem. Phys. **116**, 2696 (2002).

[127] M. Reiher and A. Wolf, J. Chem. Phys. **121**, 2037 (2004).

[128] M. Reiher and A. Wolf, J. Chem. Phys. **121**, 10945 (2004).

[129] D. Peng and K. Hirao, J. Chem. Phys. **130**, 044102 (2009).

[130] R. Fukuda, M. Hada, and H. Nakatsuji, J. Chem. Phys. **118**, 1015 (2003).

[131] R. Fukuda, M. Hada, and H. Nakatsuji, J. Chem. Phys. **118**, 1027 (2003).

[132] J. Seino and M. Hada, J. Chem. Phys. **132**, 174105 (2010).

[133] J. I. Melo, M. C. R. de Azúa, J. E. Peralta, and G. E. Scuseria, J. Chem. Phys. **123**, 204112 (2005).

[134] R. Mastalerz, R. Lindh, and M. Reiher, Chem. Phys. Lett. **465**, 157 (2008).

[135] L. Bučinský, S. Biskupič, and D. Jayatilaka, J. Chem. Phys. **133**, 174125 (2010).

[136] F. Neese, A. Wolf, T. Fleig, M. Reiher, and B. A. Hess, J. Chem. Phys. **122**, 204107 (2005).

[137] R. Mastalerz, G. Barone, R. Lindh, and M. Reiher, J. Chem. Phys. **127**, 074105 (2007).

[138] T. Yoshizawa and M. Hada, Chem. Phys. Lett. **458**, 223 (2008).

[139] J. Seino, W. Uesugi, and M. Hada, J. Chem. Phys. **132**, 164108 (2010).

[140] R. Van Zee, S. Li, Y. Hamrick, and W. Weltner Jr, J. Chem. Phys. **97**, 8123 (1992).

[141] L. J. Hayton, B. Mile, and P. L. Timms, Phys. Chem. Chem. Phys **4**, 5739 (2002).

[142] A. Wolf and M. Reiher, J. Chem. Phys. **124**, 064102 (2006).

[143] J. Autschbach, ChemPhysChem **10**, 2274 (2009).

[144] L. Visscher and K. G. Dyall, At. Data and Nucl. Data Tables **67**, 207 (1997).

[145] K. Balasubramanian and D. W. Liao, J. Phys. Chem. **92**, 6259 (1988).

[146] L. B. Knight Jr, S. Cobranchi, J. Herlong, T. Kirk, K. Balasubramanian, and K. Das, J. Chem. Phys. **92**, 2721 (1990).

[147] Z. Zhang and N. Pyper, Mol. Phys. **64**, 963 (1988).

[148] R. Van Zee, S. Li, and W. Weltner Jr, J. Am. Chem. Soc. **115**, 2976 (1993).

[149] J. Autschbach and T. Ziegler, Coord. Chem. Rev. **238**, 83 (2003).

[150] Y. Yamaguchi, J. D. Goddard, Y. Osamura, and H. F. Schaefer, *A new dimension to quantum chemistry: analytic derivative methods in ab initio molecular electronic structure theory* (Oxford University Press New York, 1994).

[151] B. A. Hess, C. M. Marian, U. Wahlgren, and O. Gropen, Chem. Phys. Lett. **251**, 365 (1996).

[152] K. Balasubramanian and D. Dai, J. Chem. Phys **93**, 7243 (1990).

[153] B. O. Roos, R. Lindh, P.-Å. Malmqvist, V. Veryazov, and P.-O. Widmark, J. Phys. Chem. A **108**, 2851 (2004).

[154] B. O. Roos, R. Lindh, P.-Å. Malmqvist, V. Veryazov, and P.-O. Widmark, J. Phys. Chem. A **109**, 6575 (2005).

[155] A. Luzanov, E. Babich, and V. Ivanov, J. Mol. Struct.: THEOCHEM **311**, 211 (1994).

[156] M. Engström, B. Minaev, O. Vahtras, and H. Ågren, Chem. Phys. **237**, 149 (1998).

[157] W. Weltner, *Magnetic atoms and molecules* (Courier Dover Publications, 1989).

[158] N. Nakatani, S. Wouters, D. Van Neck, and G. K.-L. Chan, J. Chem. Phys. **140**, 024108 (2014).

[159] R. S. Mulliken, Science **157**, 13 (1967).

[160] W. Kutzelnigg, Angew. Chem. Int. Ed. **35**, 572 (1996).

[161] A. Szabo and N. S. Ostlund, *Modern quantum chemistry: introduction to advanced electronic structure theory* (Courier Dover Publications, 1989).

[162] T. Helgaker, P. Jørgensen, and J. Olsen, *Molecular electronic-structure theory* (John Wiley & Sons Inc, 2000).

[163] R. G. Parr and W. Yang, *Density-functional theory of atoms and molecules*, vol. 16 (Oxford university press, 1989).

[164] E. K. Gross and R. M. Dreizler, *Density functional theory*, vol. 337 (Plenum Publishing Corporation, 1995).

[165] P. Hohenberg and W. Kohn, Phys. Rev. **136**, B864 (1964).

[166] W. Kohn and L. Sham, Phys. Rev. **140**, A1133 (1965).

[167] A. J. Cohen, P. Mori-Snchez, and W. Yang, Chem. Rev. **112**, 289 (2012).

[168] R. C. Lochan and M. Head-Gordon, J. Chem. Phys. **126**, 164101 (2007).

[169] W. Kurlancheek and M. Head-Gordon, Mol. Phys. **107**, 1223 (2009).

[170] D. Stück, T. A. Baker, P. Zimmerman, W. Kurlancheek, and M. Head-Gordon, J. Chem. Phys. **135**, 194306 (2011).

[171] W. Kurlancheek, R. Lochan, K. Lawler, and M. Head-Gordon, J. Chem. Phys. **136**, 054113 (2012).

[172] F. Neese, T. Schwabe, S. Kossmann, B. Schirmer, and S. Grimme, J. Chem. Theory Comput. **5**, 3060 (2009).

[173] U. Bozkaya, J. M. Turney, Y. Yamaguchi, H. F. Schaefer III, and C. D. Sherrill, J. Chem. Phys. **135**, 104103 (2011).

[174] U. Bozkaya, J. Chem. Phys. **135**, 224103 (2011).

[175] E. Soydas and U. Bozkaya, J. Chem. Theory Comput. **9**, 1452 (2013).

[176] E. F. C. Byrd, C. D. Sherrill, and M. Head-Gordon, J. Phys. Chem. A **105**, 9736 (2001).

[177] L. Farnell, J. A. Pople, and L. Radom, J. Phys. Chem. **87**, 79 (1983).

[178] D. J. Tozer, N. C. Handy, R. D. Amos, J. A. Pople, R. H. Nobes, Y. Xie, and H. F. Schaefer, Mol. Phys. **79**, 777 (1993).

[179] M. W. Wong and L. Radom, J. Phys. Chem. A **102**, 2237 (1998).

[180] P. M. W. Gill, J. A. Pople, L. Radom, and R. H. Nobes, J. Chem. Phys. **89**, 7307 (1988).

[181] P. M. Gill and L. Radom, Chem. Phys. Lett. **132**, 16 (1986).

[182] W. Chen and H. B. Schlegel, J. Chem. Phys. **101**, 5957 (1994).

[183] C. Møller and M. S. Plesset, Phys. Rev. **46**, 618 (1934).

[184] K. A. Brueckner, Phys. Rev. **96**, 508 (1954).

[185] R. K. Nesbet, Phys. Rev. **109**, 1632 (1958).

[186] N. C. Handy, J. A. Pople, M. Head-Gordon, K. Raghavachari, and G. W. Trucks, Chem. Phys. Lett. **164**, 185 (1989).

[187] L. A. Barnes and R. Lindh, Chem. Phys. Lett. **223**, 207 (1994).

[188] J. F. Stanton, J. Gauss, and R. J. Bartlett, J. Chem. Phys. **97**, 5554 (1992).

[189] R. A. Chiles and C. E. Dykstra, J. Chem. Phys. **74**, 4544 (1981).

[190] C. Hampel, K. A. Peterson, and H.-J. Werner, Chem. Phys. Lett. **190**, 1 (1992).

[191] K. Raghavachari, J. A. Pople, E. S. Replogle, M. Head-Gordon, and N. C. Handy, Chem. Phys. Lett. **167**, 115 (1990).

[192] G. E. Scuseria, Chem. Phys. Lett. **226**, 251 (1994).

[193] R. Kobayashi, N. C. Handy, R. D. Amos, G. W. Trucks, M. J. Frisch, and J. A. Pople, J. Chem. Phys. **95**, 6723 (1991).

[194] R. Kobayashi, R. D. Amos, and N. C. Handy, Chem. Phys. Lett. **184**, 195 (1991).

[195] G. D. Purvis III and R. J. Bartlett, J. Chem. Phys. **76**, 1910 (1982).

[196] G. E. Scuseria and H. F. Schaefer III, Chem. Phys. Lett. **142**, 354 (1987).

[197] A. Köhn and J. Olsen, J. Chem. Phys. **122**, 084116 (2005).

[198] C. D. Sherrill, A. I. Krylov, E. F. C. Byrd, and M. Head-Gordon, J. Chem. Phys. **109**, 4171 (1998).

[199] A. I. Krylov, C. D. Sherrill, E. F. C. Byrd, and M. Head-Gordon, J. Chem. Phys. **109**, 10669 (1998).

[200] A. I. Krylov, C. D. Sherrill, and M. Head-Gordon, J. Chem. Phys. **113**, 6509 (2000).

[201] S. R. Gwaltney, C. D. Sherrill, M. Head-Gordon, and A. I. Krylov, J. Chem. Phys. **113**, 3548 (2000).

[202] T. B. Pedersen, H. Koch, and C. Hättig, J. Chem. Phys. **110**, 8318 (1999).

[203] T. B. Pedersen, B. Fernández, and H. Koch, J. Chem. Phys. **114**, 6983 (2001).

[204] U. Bozkaya and H. F. Schaefer III, J. Chem. Phys. **136**, 204114 (2012).

[205] G. D. Lindh, T. J. Mach, and T. D. Crawford, Chem. Phys. **401**, 125 (2012).

[206] A. P. L. Rendell, G. B. Bacskay, N. S. Hush, and N. C. Handy, J. Chem. Phys. **87**, 5976 (1987).

[207] J. Baker, A. Scheiner, and J. Andzelm, Chem. Phys. Lett. **216**, 380 (1993).

[208] G. J. Laming, N. C. Handy, and R. D. Amos, Mol. Phys. **80**, 1121 (1993).

[209] J. A. Pople, P. M. W. Gill, and N. C. Handy, Int. J. Quantum Chem. **56**, 303 (1995).

[210] J. W. Gauld, L. A. Eriksson, and L. Radom, J. Phys. Chem. A **101**, 1352 (1997).

[211] V. Barone, J. Chem. Phys. **101**, 6834 (1994).

[212] C. Sherrill, M. S. Lee, and M. Head-Gordon, Chem. Phys. Lett. **302**, 425 (1999).

[213] P. M. Kozlowski, G. Rauhut, and P. Pulay, J. Chem. Phys. **103**, 5650 (1995).

[214] D. P. Chong, O. V. Gritsenko, and E. J. Baerends, J. Chem. Phys. **116**, 1760 (2002).

[215] O. V. Gritsenko, B. Braïda, and E. J. Baerends, J. Chem. Phys. **119**, 1937 (2003).

[216] R. Stowasser and R. Hoffmann, J. Am. Chem. Soc. **121**, 3414 (1999).

[217] P. Politzer and F. Abu-Awwad, Theor. Chem. Acc. **99**, 83 (1998).

[218] R. W. Godby, M. Schlüter, and L. J. Sham, Phys. Rev. B **37**, 10159 (1988).

[219] J. P. Perdew and M. Levy, Phys. Rev. Lett. **51**, 1884 (1983).

[220] W. Yang, R. G. Parr, and R. Pucci, J. Chem. Phys. **81**, 2862 (1984).

[221] J. P. Perdew and M. R. Norman, Phys. Rev. B **26**, 5445 (1982).

[222] A. Savin, C. Umrigar, and X. Gonze, Chem. Phys. Lett. **288**, 391 (1998).

[223] A. J. Cohen, P. Mori-Sánchez, and W. Yang, Phys. Rev. B **77**, 115123 (2008).

[224] U. Salzner and R. Baer, J. Chem. Phys. **131**, 231101 (2009).

[225] T. Tsuneda, J.-W. Song, S. Suzuki, and K. Hirao, J. Chem. Phys. **133**, 174101 (2010).

[226] W. Kohn, A. Becke, and R. Parr, J. Phys. Chem. **100**, 12974 (1996).

[227] E. Baerends and O. Gritsenko, J. Phys. Chem. A **101**, 5383 (1997).

[228] L. Hedin, Phys. Rev. **139**, A796 (1965).

[229] M. S. Hybertsen and S. G. Louie, Phys. Rev. B **34**, 5390 (1986).

[230] J. Schirmer, L. S. Cederbaum, and O. Walter, Phys. Rev. A **28**, 1237 (1983).

[231] A. Seidl, A. Görling, P. Vogl, J. A. Majewski, and M. Levy, Phys. Rev. B **53**, 3764 (1996).

[232] F. Fuchs, J. Furthmüller, F. Bechstedt, M. Shishkin, and G. Kresse, Phys. Rev. B **76**, 115109 (2007).

[233] L. S. Cederbaum, Theor. Chim. Acta **31**, 239 (1973).

[234] L. Cederbaum and W. Domcke, Adv. Chem. Phys **36**, 205 (1977).

[235] J. Linderberg and Y. Öhrn, *Propagators in Quantum Chemistry* (Wiley-Interscience Hoboken, NJ, 2004).

[236] J. V. Ortiz, WIREs Comput Mol Sci **3**, 123 (2013).

[237] R. J. Bartlett, Chem. Phys. Lett. **484**, 1 (2009).

[238] P. Verma and R. J. Bartlett, J. Chem. Phys. **136**, 044105 (2012).

[239] P. Verma and R. J. Bartlett, J. Chem. Phys. **137**, 134102 (2012).

[240] J. D. Talman and W. F. Shadwick, Phys. Rev. A **14**, 36 (1976).

[241] J. B. Krieger, Y. Li, and G. J. Iafrate, Phys. Rev. A **45**, 101 (1992).

[242] J. B. Krieger, Y. Li, and G. J. Iafrate, Phys. Rev. A **46**, 5453 (1992).

[243] W. Yang and Q. Wu, Phys. Rev. Lett. **89**, 143002 (2002).

[244] S. Hirata, S. Ivanov, I. Grabowski, R. J. Bartlett, K. Burke, and J. D. Talman, J. Chem. Phys. **115**, 1635 (2001).

[245] F. D. Sala and A. Görling, J. Chem. Phys. **115**, 5718 (2001).

[246] A. Heßelmann, Phys. Chem. Chem. Phys. **8**, 563 (2006).

[247] I. Grabowski, S. Hirata, S. Ivanov, and R. J. Bartlett, J. Chem. Phys. **116**, 4415 (2002).

[248] R. J. Bartlett, I. Grabowski, S. Hirata, and S. Ivanov, J. Chem. Phys. **122**, 034104 (2005).

[249] I. V. Schweigert, V. F. Lotrich, and R. J. Bartlett, J. Chem. Phys. **125**, 104108 (2006).

[250] R. Shepard, Adv. Chem. Phys. **69**, 63 (1987).

[251] H.-J. Werner, Adv. Chem. Phys. **69**, 1 (1987).

[252] B. O. Roos, Adv. Chem. Phys. **69**, 399 (1987).

[253] M. W. Schmidt and M. S. Gordon, Ann. Rev. in Phys. Chem. **49**, 233 (1998).

[254] S. R. White, Phys. Rev. Lett. **69**, 2863 (1992).

[255] S. R. White, Phys. Rev. B **48**, 10345 (1993).

[256] S. R. White and R. L. Martin, J. Chem. Phys. **110**, 4127 (1999).

[257] G. K. L. Chan and M. Head-Gordon, J. Chem. Phys. **116**, 4462 (2002).

[258] D. Zgid and M. Nooijen, J. Chem. Phys. **128**, 144115 (2008).

[259] D. Zgid and M. Nooijen, J. Chem. Phys. **128**, 144116 (2008).

[260] D. Ghosh, J. Hachmann, T. Yanai, and G. K.-L. Chan, J. Chem. Phys. **128**, 144117 (2008).

[261] T. Yanai, Y. Kurashige, D. Ghosh, and G. K.-L. Chan, Int. J. Quantum Chem. **109**, 2178 (2009).

[262] Y. Jung, R. C. Lochan, A. D. Dutoi, and M. Head-Gordon, J. Chem. Phys. **121**, 9793 (2004).

[263] S. Grimme, J. Chem. Phys. **118**, 9095 (2003).

[264] T. Yanai and G. K.-L. Chan, J. Chem. Phys. **124**, 194106 (2006).

[265] T. Yanai and G. K.-L. Chan, J. Chem. Phys. **127**, 104107 (2007).

[266] E. Neuscamman, T. Yanai, and G. K.-L. Chan, J. Chem. Phys. **130**, 124102 (2009).

[267] E. Neuscamman, T. Yanai, and G. K.-L. Chan, J. Chem. Phys. **130**, 169901 (2009).

[268] E. Neuscamman, T. Yanai, and G. K.-L. Chan, J. Chem. Phys. **132**, 024106 (2010).

[269] T. Yanai, Y. Kurashige, E. Neuscamman, and G. K.-L. Chan, J. Chem. Phys. **132**, 024105 (2010).

[270] E. Neuscamman, T. Yanai, and G. K.-L. Chan, Int. Rev. Phys. Chem. **29**, 231 (2010).

[271] T. Yanai, Y. Kurashige, E. Neuscamman, and G. K.-L. Chan, Phys. Chem. Chem. Phys. **14**, 7809 (2012).

[272] W. Kutzelnigg, D. Mukherjee, and S. Koch, J. Chem. Phys. **87**, 5902 (1987).

[273] D. Mukherjee, W. Kutzelnigg, and S. Koch, J. Chem. Phys. **87**, 5911 (1987).

[274] W. Kutzelnigg and D. Mukherjee, J. Chem. Phys. **107**, 432 (1997).

[275] S. Ten-no and J. Noga, WIREs: Comput. Mol. Sci. **2**, 114 (2011).

[276] H.-J. Werner, T. B. Adler, G. Knizia, and F. R. Manby, in *Recent Progress in Coupled Cluster Methods*, edited by P. Cársky, J. Paldus, and J. Pittner (Springer, 2010).

[277] D. P. Tew, C. Hättig, R. A. Bachorz, and W. Klopper, in *Recent Progress in Coupled Cluster Methods*, edited by P. Cársky, J. Paldus, and J. Pittner (Springer, 2010).

[278] L. Kong, F. A. Bischoff, and E. F. Valeev, Chem. Rev. **112**, 75 (2011).

[279] T. Yanai and T. Shiozaki, J. Chem. Phys. **136**, 084107 (2012).

[280] D. Mukherjee, Chem. Phys Lett. **274**, 561 (1997).

[281] W. Kutzelnigg and D. Mukherjee, J. Chem. Phys. **107**, 432 (1997).

[282] A. D. Becke, J. Chem. Phys. **98**, 5648 (1993).

[283] T. H. Dunning Jr., J. Chem. Phys. **90**, 1007 (1989).

[284] D. E. Woon and T. H. Dunning Jr., J. Chem. Phys. **100**, 2975 (1994).

[285] D. E. Woon and T. H. Dunning Jr., J. Chem. Phys. **98**, 1358 (1993).

[286] N. B. Balabanov and K. A. Peterson, J. Chem. Phys. **123**, 064107 (2005).

[287] R. A. Kendall, T. H. Dunning Jr., and R. J. Harrison, J. Chem. Phys. **96**, 6796 (1992).

[288] K. Raghavachari, G. W. Trucks, J. A. Pople, and M. Head-Gordon, Chem. Phys. Lett. **157**, 479 (1989).

[289] K. E. Yousaf and K. A. Peterson, Chem. Phys. Lett. **476**, 303 (2009).

[290] E. F. Valeev, Chem. Phys. Lett. **395**, 190 (2004).

[291] T. Koopmans, Physica **1**, 104 (1934).

[292] J. P. Perdew, R. G. Parr, M. Levy, and J. L. Balduz, Phys. Rev. Lett. **49**, 1691 (1982).

[293] J. P. Perdew and M. Levy, Phys. Rev. B **56**, 16021 (1997).

[294] T. Stein, J. Autschbach, N. Govind, L. Kronik, and R. Baer, J. Phys. Chem. Lett. **3**, 3740 (2012).

[295] R. Baer, E. Livshits, and U. Salzner, Ann. Rev. Phys. Chem. **61**, 85 (2010).

[296] T. Stein, H. Eisenberg, L. Kronik, and R. Baer, Phys. Rev. Lett. **105**, 266802 (2010).

[297] C. Zhan, J. Nichols, and D. Dixon, J. Phys. Chem. A **107**, 4184 (2003).

[298] J.-Q. Sun and R. J. Bartlett, J. Chem. Phys. **107**, 5058 (1997).

[299] A. Grüneis, M. Marsman, and G. Kresse, J. Chem. Phys. **133**, 074107 (2010).

[300] V. A. Rassolov, J. A. Pople, M. A. Ratner, and T. L. Windus, J. Chem. Phys. **109**, 1223 (1998).

[301] O. A. Vydrov and G. E. Scuseria, J. Chem. Phys. **125**, 234109 (2006).

[302] O. A. Vydrov, J. Heyd, A. V. Krukau, and G. E. Scuseria, J. Chem. Phys. **125**, 074106 (2006).

[303] O. A. Vydrov, G. E. Scuseria, and J. P. Perdew, J. Chem. Phys. **126**, 154109 (2007).

[304] C. Adamo and V. Barone, J. Chem. Phys. **110**, 6158 (1999).

[305] M. Quinby and R. Feltham, Inorg. Chem. **11**, 2468 (1972).

[306] J. Enemark and R. Feltham, J. Am. Chem. Soc. **96**, 5002 (1974).

[307] M. Head-Gordon, R. J. Rico, M. Oumi, and T. J. Lee, Chem. Phys. Lett. **219**, 21 (1994).

[308] O. Christiansen, H. Koch, and P. Jorgensen, Chem. Phys. Lett. **243**, 409 (1995).

[309] S. Grimme, J. Chem. Phys. **124**, 034108 (2006).